

RESEARCH ACTIVITIES VIII

Laser Research Center for Molecular Science

VIII-A Developments and Researches of New Laser Materials

Although development of lasers is remarkable, there are no lasers which lase in ultraviolet and far infrared regions. However, it is expected that these kinds of lasers break out a great revolution in not only the molecular science but also in the industrial world.

In this project we research characters of new materials for ultraviolet and far infrared lasers, and develop new lasers by using these laser materials.

VIII-A-1 $\text{Ce}^{3+}:\text{LiCaAlF}_6$ Crystal for High-Gain or High-Peak-Power Amplification of Ultraviolet Femtosecond Pulses and New Potential Ultraviolet Gain Medium: $\text{Ce}^{3+}:\text{LiSr}_{0.8}\text{Ca}_{0.2}\text{AlF}_6$

LIU, Zhenlin¹; KOZEKI, Toshimasa; SUZUKI, Yuji; SARUKURA, Nobuhiko; SHIMAMURA, Kiyoshi²; FUKUDA, Tsuguo²; HIRANO, Masahiro¹; HOSONO, Hideo^{1,3}

(¹ERATO; ²Tohoku Univ.; ³Tokyo Inst. Tech.)

[*IEEE J. Sel. Top. Quantum Electron.* **7**, 542 (2001)]

To develop high-peak-power ultrashort pulse laser systems in the ultraviolet region, a large $\text{Ce}^{3+}:\text{LiCaAlF}_6$ (Ce:LiCAF) crystal, a tunable ultraviolet laser medium with large saturation fluence and broad gain spectrum width, was grown successfully with a diameter of more than 70 mm. To demonstrate high small signal gain, a four-pass confocal amplifier with 60 dB gain and 54 mJ output energy was constructed. Chirped pulse amplification (CPA) in the ultraviolet region was demonstrated using Ce:LiCAF for higher energy extraction. A modified bow-tie-style four-pass amplifier pumped by 100-mJ 266-nm 10-Hz pulses from a Q-switched Nd:YAG laser had 370-times gain and delivered 6-mJ 290-nm pulses. After dispersion compensation, the output pulses can be compressed down to 115 fs. This is the first ultraviolet, all-solid-state high-peak-power CPA laser system using ultraviolet gain media, and this demonstration shows further scalability of the Ce:LiCAF CPA system. Additionally, a new gain medium, $\text{Ce}^{3+}:\text{LiSr}_{0.8}\text{Ca}_{0.2}\text{AlF}_6$, with longer fluorescence lifetime and sufficient gain spectrum width over 18 nm was grown to upgrade this system as a candidate for a final power amplifier gain module.

VIII-A-2 Optical Fiber for Deep Ultraviolet Light

OTO, Masanori¹; KIKUGAWA, Shinya²; SARUKURA, Nobuhiko; HIRANO, Masahiro³; HOSONO, Hideo^{3,4}

(¹Showa Electric Wire Cable; ²Asahi Glass Co. Ltd.; ³ERATO; ⁴Tokyo Inst. Tech.)

[*IEEE Photonics Technol. Lett.* **13**, 978 (2001)]

Deep ultraviolet optical fibers are fabricated using modified SiO_2 glasses containing 2000-ppm fluorine for

the clad and 200 ppm for the core. The transmission at 193 nm is improved to more than 60%/m by optimizing the fiber drawing condition. The H-2-impregnation into the fiber suppresses the degradation of the transmission by irradiation of ArF excimer laser (50 mJ/cm²/pulse). Further improvement may be expected by reducing oxygen-deficient center (I) defect generation in the drawing process.

VIII-A-3 Crystal Growth of Fluorides for Optical Applications

SHIMAMURA, Kiyoshi¹; SATO, Hiroki¹; BENSALAH, Amina¹; SUDESH, Vikas¹; MACHIDA, Hiroshi²; SARUKURA, Nobuhiko; FUKUDA, Tsuguo¹

(¹Tohoku Univ.; ²Token Corp.)

[*Cryst. Res. Technol.* **36**, 801 (2001)]

Ce-doped and undoped LiCaAlF_6 , LiSrAlF_6 , LiYF_4 , LiLuF_4 and KMgF_3 single crystals were grown by the Czochralski technique under CF_4 atmosphere. The effective distribution coefficients of Ce^{3+} in LiCaAlF_6 , LiSrAlF_6 , LiYF_4 and LiLuF_4 were determined to be 0.031, 0.028, 0.116 and 0.054, respectively. Laser output energy of 60 mJ and 27 mJ were obtained using the grown Ce:LiCaAlF₆ and Ce:LiLuF₄ single crystals, respectively. Undoped LiCaAlF_6 and KMgF_3 single crystals showed a transmission edge at 112 nm and 115 nm, respectively.

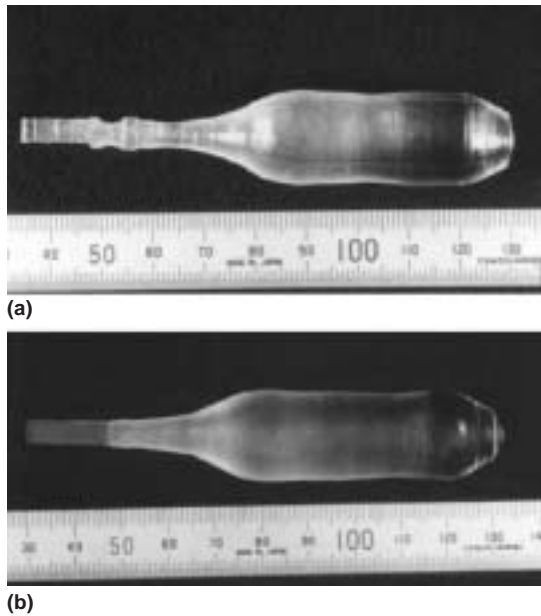


Figure 1. As-grown Ce-doped (a) LiCaAlF_6 and (b) LiSrAlF_6 single crystals 18 mm in diameter pulled along the a -axis.

VIII-A-4 Growth of Ce-Doped Colquiriite- and Scheelite-Type Single Crystals for UV Laser Applications

SHIMAMURA, Kiyoshi¹; SATO, Hiroki¹; BENSALAH, Amina¹; MACHIDA, Hiroshi²; SARUKURA, Nobuhiko; FUKUDA, Tsuguo¹ (¹Tohoku Univ.; ²Tokin Corp.)

[*Opt. Mater.* **19**, 109 (2002)]

Ce-doped Colquiriite- and Scheelite-type fluoride single crystals were grown by the Czochralski technique. The formation of inclusions and cracks accompanying the crystal growth was investigated. The effective distribution co-efficients of Ce^{3+} in LiCaAlF_6 , LiSrAlF_6 , LiYF_4 and LiLuF_4 were determined to be 0.031, 0.028, 0.116 and 0.054, respectively. Ultraviolet pulse generations with an output energy of 60 and 27 mJ were obtained from Ce: LiCaAlF_6 and Ce: LiLuF_4 lasers.

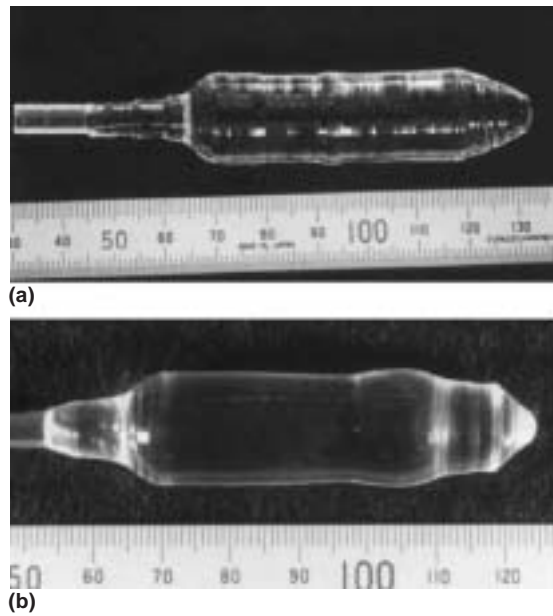


Figure 1. As-grown Ce-doped: (a) LiYF_4 and (b) LiLuF_4 single crystals of 18 mm in diameter pulled along the a -axis.

VIII-A-5 High-Energy Pulse Generation from Solid-State Ultraviolet Lasers Using Large Ce:Fluoride Crystals

LIU, Zhenlin¹; SHIMAMURA, Kiyoshi²; FUKUDA, Tsuguo²; KOZEKI, Toshimasa; SUZUKI, Yuji; SARUKURA, Nobuhiko (¹ERATO; ²Tohoku Univ.)

[*Opt. Mater.* **19**, 123 (2002)]

A large $\text{Ce}^{3+}:\text{LiCaAlF}_6$ (Ce:LiCAF) crystal with 15 mm diameter was grown successfully by the Czochralski method. Owing to its large size, 60 mJ, 289 nm pulses were generated directly from a quasi-coaxially pumped Ce:LiCAF laser. In addition, a new noncollinear Brewster-angle-pumping disk oscillator scheme was demonstrated for further output-energy scaling. An ultraviolet solid-state $\text{Ce}^{3+}:\text{LiLuF}_4$ (Ce:LLF) laser which was pumped transversely by a KrF excimer laser with the repetition rate of 1 Hz produced a 27 mJ, 309 nm pulse using a large Ce:LLF crystal which was grown by the Czochralski method, and the slope efficiency was approximately 17%.

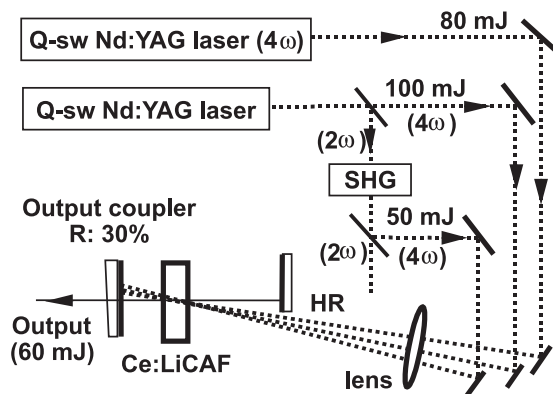


Figure 1. Experimental setup for high-power Ce:LiCAF laser pumped by the fourth harmonics of two Q-switched Nd:YAG lasers.

VIII-A-6 New Adjustment Technique for Time Coincidence of Femtosecond Laser Pulses Using Third Harmonic Generation in Air and its Application to Holograph Encoding System

KAWAMURA, Ken-ichi¹; ITO, Naoko²;
SARUKURA, Nobuhiko; HIRANO, Masahiro¹;
HOSONO, Hideo^{1,3}
(¹ERATO; ²Mater. Struct. Lab.; ³Tokyo Inst. Tech.)

[*Rev. Sci. Instrum.* **73**, 1711 (2002)]

The third harmonic generation of light (266 nm) is enhanced, sensitively depending on the time delay between a pair of pulses split from a single 800 nm femtosecond laser pulse, when they are focused and collided in air. This finding offers a convenient and widely applicable technique to detect temporal and spatial overlapping of two femtosecond pulses. This technique has several advantages over the conventional sum frequency generation method using nonlinear optical crystals, since it obviates the need for expensive crystals, free from phase matching, and elimination of temporal walk off. By applying it to "a holographic encoding system using an interference femtosecond laser pulse," a periodic fringe spacing is minimized to ~ 430 nm by extending the colliding angle between two-pulse beams up to ~ 160 °C.

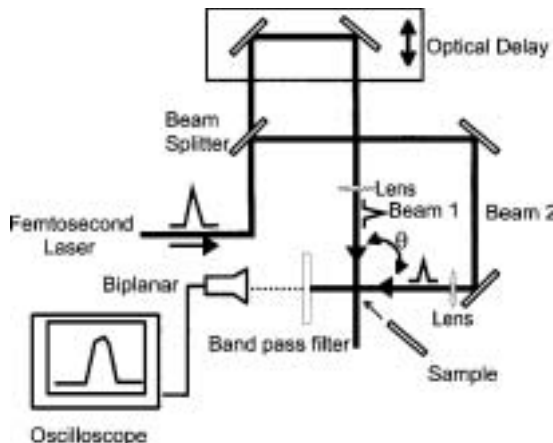


Figure 1. Experimental setup for holographic encoding system.

VIII-A-7 Hybrid Time-Resolved Spectroscopic System for Evaluating Laser Material Using a Table-Top-Sized, Low-Jitter, 3-MeV Picosecond Electron-Beam Source with a Photocathode

SUZUKI, Yuji; KOZEKI, Toshimasa; ONO, Shingo;
MURAKAMI, Hidetoshi; OHTAKE, Hideyuki;
SARUKURA, Nobuhiko; NAKAJYO, Terunobu¹;
SAKAI, Fumio¹; AOKI, Yasushi¹
(¹Sumitomo Heavy Industries, Ltd.)

[*Appl. Phys. Lett.* **80**, 3280 (2002)]

Hybrid time-resolved spectroscopy of laser media comparing electron-beam excitation and optically excited cases is performed using a newly developed, table-top-sized, low-jitter, 3-MeV picosecond electron-beam source with a photocathode. The properties of an electron-beam-pumped Ce³⁺:LiCaAlF₆ (Ce:LiCAF) ultraviolet laser medium significantly differ from those of an optically pumped medium.

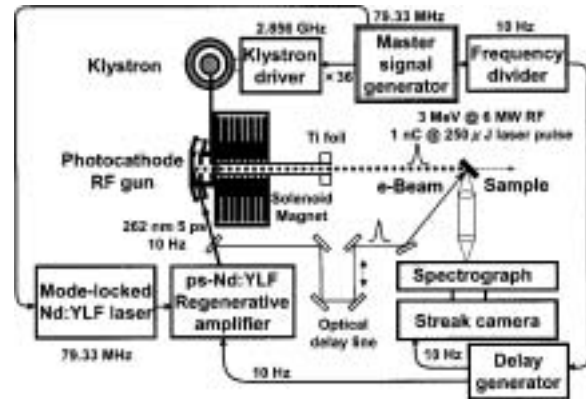


Figure 1. Experimental setup. The photocathode rf gun was irradiated with 262-nm optical pulses from a Nd:YLF regenerative system synchronously operated with a 2.856-GHz, 6-MW klystron to accelerate the extracted 1-nC photoelectron beam. The e-beam was irradiated onto the sample after being passed through titanium foil. A portion of the pumping optical pulse irradiated the same sample to compare the excitation scheme. A streak camera was equipped with a 30-cm spectrograph to measure the fluorescence spectrum and fluorescence lifetime.

VIII-A-8 Simultaneous Measurement of Thickness and Water Content of Thin Black Ink Films for the Printing Using THz Radiation

OHTAKE, Hideyuki; SUZUKI, Yuji; ONO, Shingo;
SARUKURA, Nobuhiko; HIROSUMI, Tomoya¹;
OKADA, Tomoaki²
(¹AISIN SEIKI Co., Ltd.; ²Mitsubishi Heavy Industry Co., Ltd.)

[*Jpn. J. Appl. Phys., Part 2* **41**, L475 (2002)]

Using THz radiation, a simple, noncontact, simultaneous method is applied to measure thickness and water content of black ink films independently from frequency-dependent and frequency-independent absorption characteristics of black ink films.

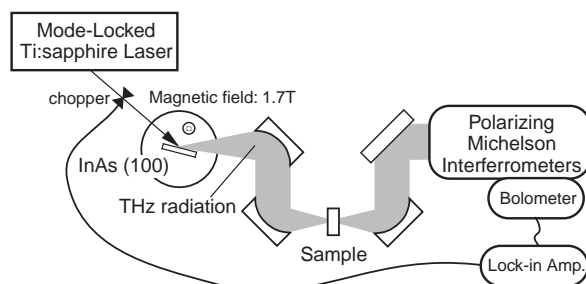


Figure 1. Experimental setup for simultaneously measuring thickness and water content of thin black ink films. The magnetic field direction is from the back to the surface.

VIII-A-9 Far-Infrared Absorption Measurements of Polypeptides and Cytochrome *c* by THz Radiation

YAMAMOTO, Kohji¹; TOMINAGA, Keisuke¹;
SASAKAWA, Hiroaki¹; TAMURA, Atsuo¹;
MURAKAMI, Hidetoshi; OHTAKE, Hideyuki;
SARUKURA, Nobuhiko
(¹Kobe Univ.)

[*Bull. Chem. Soc. Jpn.* **75**, 1083 (2002)]

Pulsed terahertz (THz) radiation and black-body radiation are applied to measure far infrared (FIR) absorption spectra of polypeptides and cytochrome *c* in the wavenumber region from 7 cm^{-1} to 160 cm^{-1} . In the region from 7 cm^{-1} to 55 cm^{-1} , FIR absorption cross sections of polyglycine and poly-*L*-alanine in powder are greater than those of glycine and *L*-alanine in powder. On the other hand, FIR absorption spectra of cytochrome *c* in lyophilized powder show little dependence on protein structures. The structures of biopolymers are investigated by mid-IR absorption (polypeptides and cytochrome *c*) and by resonance Raman scattering (cytochrome *c*). FIR spectral features of biopolymers in the THz frequency region are qualitatively discussed in terms of density of states and homogeneous/inhomogeneous broadening.

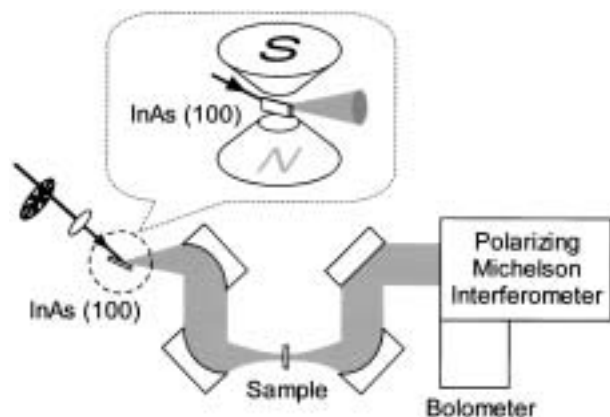


Figure 1. FIR absorption spectrometer using the THz radiation. Pulses at 800 nm with 70-fs width at 80-MHz repetition rate irradiate an InAs wafer, which is placed in a magnetic flux density of 1.7 T generated by an electromagnet. The (100)-InAs surface is parallel to a direction of the magnetic flux density. The THz radiation from the (100)-InAs is collimated by an off-axis parabolic mirror. The THz radiation is focused at a sample position and collimated again by an off-axis mirror. Intensity of the THz radiation is detected by a germanium bolometer which is cooled by helium liquid. Chopping frequency of the pump pulse is 200 Hz. A polarizing Michelson interferometer is vacuumsealed. All the FIR absorption system other than the polarizing Michelson interferometer is open to air. When using the black-body radiation for FIR absorption measurements, the generation part of the THz-radiation is replaced by a black-body.

VIII-A-10 0.43 J, 10 Hz Fourth Harmonic Generation of Nd:YAG Laser Using Large $\text{Li}_2\text{B}_4\text{O}_7$ Crystals

SUZUKI, Yuji; ONO, Shingo; MURAKAMI, Hidetoshi; KOZEKI, Toshimasa; OHTAKE, Hideyuki; SARUKURA, Nobuhiko; MASADA, Genta¹; SHIRAISHI, Hiroyuki¹; SEKINE, Ichiro¹
(¹Mitsubishi Materials Corp.)

[*Jpn. J. Appl. Phys., Part 2* **41**, L823 (2002)]

Using large-sized $\text{Li}_2\text{B}_4\text{O}_7$ crystals, 0.43 J, 266 nm pulses are obtained from a 10 Hz Nd:YAG laser with a total conversion efficiency of 30.5%. Moreover, 4 W operation for over 15 h is demonstrated.

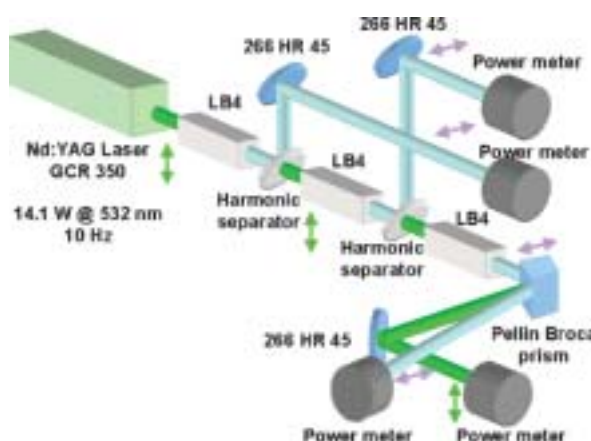


Figure 1. Experimental setup for three-cascade, fourth harmonic generation using LiB_4 crystals.

VIII-A-11 Electron-Beam Excitation of a $\text{Ce}^{3+}:\text{LiCaAlF}_6$ Crystal for Future High-Peak-Power UV Lasers

KOZEKI, Toshimasa; SUZUKI, Yuji; SAKAI, Masahiro; OHTAKE, Hideyuki; SARUKURA, Nobuhiko; SHIMAMURA, Kiyoshi¹; FUKUDA, Tsuguo¹; NAKAJYO, Terunobu²; SAKAI, Fumio²; AOKI, Yasushi²
(¹Tohoku Univ.; ²Sumitomo Heavy Industries Ltd.)

[*Appl. Phys. B* **74**, S185 (2002)]

In this experiment, we performed ultrafast spectroscopy on an electron-beam-excited $\text{Ce}^{3+}:\text{LiCaAlF}_6$ ($\text{Ce}:\text{LiCAF}$) crystal. The time-resolved fluorescence spectrum and lifetime with e-beam pumping differ significantly from those in the optically pumped case. These results suggest a new pumping scheme for an ultrashort pulse amplifier.

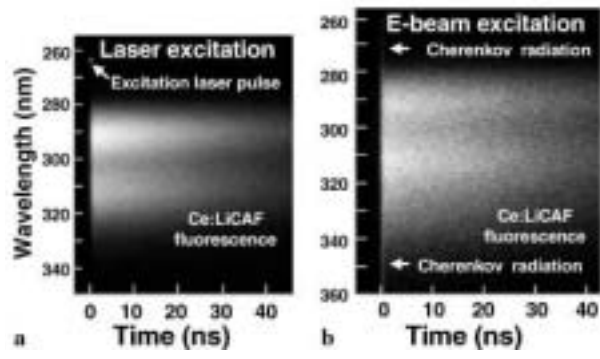


Figure 1. The streak camera images of the fluorescence from Ce:LiCAF, excited **a** by a 262-nm-pulse and **b** by an electron pulse. In the case of electron pulse excitation, a broadband, short-duration Cherenkov radiation is clearly seen.

VIII-B Development and Research of Advanced Tunable Solid State Lasers

Diode-pumped solid-state lasers can provide excellent spatial mode quality and narrow linewidths. The high spectral power brightness of these lasers has allowed high efficiency frequency extension by nonlinear frequency conversion. Moreover, the availability of new and improved nonlinear optical crystals makes these techniques more practical. Additionally, quasi phase matching (QPM) is a new technique instead of conventional birefringent phase matching for compensating phase velocity dispersion in frequency conversion. These kinds of advanced tunable solid-state light sources, so to speak "Chroma Chip Lasers," will assist the research of molecular science.

In this projects we are developing Chroma Chip Lasers based on diode-pumped-microchip-solid-state lasers and advanced nonlinear frequency conversion technique.

VIII-B-1 Thermal-Birefringence-Induced Depolarization in Nd:YAG Ceramics

SHOJI, Ichiro; SATO, Yoichi; KURIMURA, Sunao; LUPEI, Voicu¹; TAIRA, Takunori; IKESUE, Akio²; YOSHIDA, Kunio³
(¹IMS and IAP, Romania; ²JFCC; ³Osaka Inst. Tech.)

[*Opt. Lett.* **27**, 234 (2002)]

Nd:YAG ceramics are promising candidates for high-power and high-efficiency microchip laser materials because highly transparent and highly Nd³⁺-doped samples are available¹⁾ without degradation in thermomechanical properties.²⁾ We have investigated the optical properties of Nd:YAG ceramics and succeeded in microchip laser oscillation.³⁾ In this work we have investigated depolarization effect caused by thermally induced birefringence in Nd:YAG ceramics, which should be an essential issue for controlling polarization under high-power operation.

Thermal birefringence effect was measured with the pump-probe experiment. A Ti:sapphire laser oscillating at 808 nm was used as the pump source, which was focused onto the sample with the radius of 80 μm . The linearly polarized He-Ne laser beam of 1 mm radius was used as the probe. After passing through the sample, only the depolarized component of the probe beam was detected. The measured samples were 1.0, 1.3, 2.0, and 3.4 at.% Nd³⁺-doped YAG ceramics, and 1.0 and 1.3 at.% Nd:YAG single crystals. The thickness of each sample was ~ 1 mm, and (111)-cut samples were used for the single crystals.

Figure 1 shows the depolarization as a function of Nd³⁺ concentration at the absorbed pump power of 1000 mW. We found that the depolarization is nearly same between the ceramic and single-crystal YAG for the same Nd³⁺ concentrations. Because YAG ceramics consist of a lot of YAG single-crystal grains (their sizes are in several tens of microns) with various directions, which means that the birefringence effect in a ceramic sample is average of that in those grains, we suppose our results indicate that the average is close to the birefringence effect for (111)-cut Nd:YAG single crystals.

Moreover, it was also found that the depolarization became larger in samples with higher Nd³⁺ concentrations even if the same pump power was absorbed. We believe that the main reason is the difference of thermal

loading for the samples with different Nd³⁺ concentrations. For a highly Nd³⁺-doped sample, in which the interaction between Nd³⁺ ions is significant, the amount of nonradiative relaxation increases and radiative quantum efficiency gets smaller. Under the condition of no laser extraction, the smaller quantum efficiency causes larger thermal loading, that is, more heat generation in the sample even at the same absorbed power, and this induces larger thermal birefringence. The dotted line in Figure 1 shows the calculated result, in which we used the values of thermal loading obtained by Lupei *et al.*⁴⁾ The agreement between the experiment and rough estimation is satisfactory. When lasing occurs, on the other hand, thermal birefringence is expected to be greatly reduced because the thermal loading is then independent of radiative quantum efficiency. This means that *cw* or high-repetition-rate, high-average-power Q-switched operation is preferable for highly Nd³⁺-doped ceramics.

References

- 1) A. Ikesue, T. Kinoshita, K. Kamata and K. Yoshida, *J. Am. Ceram. Soc.* **78**, 1033 (1995).
- 2) T. Taira, A. Ikesue and K. Yoshida, *OSA Trends in Optics and Photonics* **19**, 430 (1998).
- 3) I. Shoji, S. Kurimura, Y. Sato, T. Taira, A. Ikesue and K. Yoshida, *Appl. Phys. Lett.* **77**, 939 (2000).
- 4) V. Lupei, A. Lupei, N. Pavel, T. Taira, I. Shoji and A. Ikesue, *Appl. Phys. Lett.* **79**, 590 (2001).

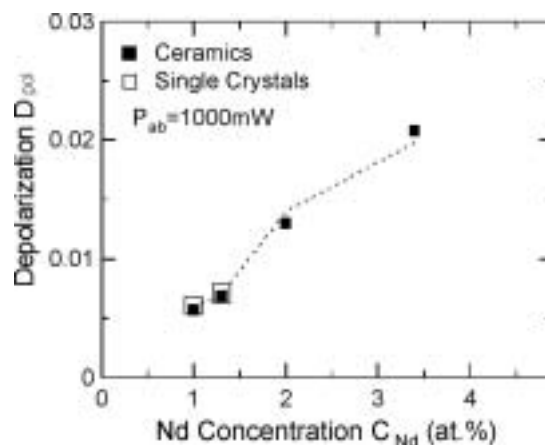


Figure 1. Depolarization as a function of Nd³⁺ concentration for the ceramic and single-crystal samples at the absorbed pump power of 1000 mW. The dotted line is the calculation taking account of increase of thermal loading.

VIII-B-2 Intrinsic Reduction of the Depolarization Loss in Solid-State Lasers by Use of a (110)-Cut $\text{Y}_3\text{Al}_5\text{O}_{12}$ Crystal

SHOJI, Ichiro; TAIRA, Takunori

[*Appl. Phys. Lett.* **80**, 3048 (2002)]

Thermally induced birefringence in solid-state laser materials is a serious problem in developing high-power and high-beam-quality lasers and amplifiers because it causes bifocusing and depolarization of a linearly polarized beam. A number of techniques which use a 90° rotator and a quarter-wave plate, *etc.*, have been suggested to compensate the depolarization. However, these compensations have been applied exclusively for (111)-cut YAG crystals, presumably because the (111) plane has simple, circularly symmetrical birefringence so that using (111)-cut rods is conventional. We report intrinsic reduction of depolarization without any compensation by use of Nd:YAG rods cut other than (111).

Koehler and Rice analyzed thermally induced birefringence in Nd:YAG rods with various directions,^{1,2)} and concluded that the amount of depolarization at the high-power limit is independent of rod directions, as shown in Figure 1. However, there were two mistakes in their theory. Figure 1 also shows the dependence of the depolarization on absorbed pump power based on our calculation when the laser beam radius r_a is equal to the rod radius r_0 . The amount of depolarization depends on the directions of planes and polarizations even at high power, and becomes smallest when the angle between the direction of polarization and the crystal axis, γ , is equal to 45° in the (100) plane, the amount for which is half that for the (111) plane at high power and 1/6 at low power.

Moreover, we have found that the depolarization can be greatly reduced by use of a (110)-cut rod under condition that r_a is smaller than r_0 . When the distance from the center of the rod, r , is as large as r_0 , the eigenvectors are directed nearly to the radial and the tangential directions at all the angles. On the other hand, when r is small, all eigenvectors are nearly aligned in one direction. Because of this nature, if the direction of the polarization is close to the crystal axis, a beam with small radius can propagate through the rod almost undepolarized. Figure 2 shows, as an example, dependence of the depolarization on the absorbed pump power when $r_a = r_0/5$ and $\gamma = 0^\circ$. The depolarization for the (110) plane reduces to about 1/50 of that for the (111) plane. This condition can be realized by use of an aperture to control the beam size in the case of the uniform pumping. A composite material in which the doped YAG is surrounded by the undoped YAG also makes the same condition and realizes better extraction efficiency. For the end pumping, on the other hand, the condition is easily satisfied because the focused pump beam itself plays a role as a gain aperture.

References

- 1) W. Koehler and D. K. Rice, *J. Quantum Electron* **QE-6**, 557 (1970).
- 2) W. Koehler and D. K. Rice, *J. Opt. Soc. Am.* **61**, 758 (1971).

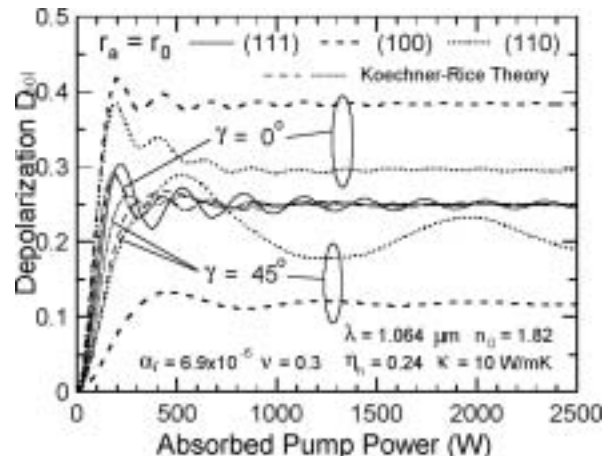


Figure 1. Dependence of the depolarization on the absorbed pump power for the (111), (100), and (110) planes based on Koehler and Rice's theory (thin curves) and our calculation (thick curves).

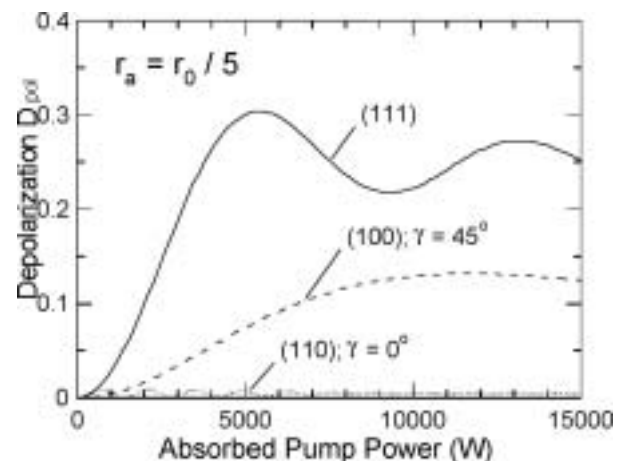


Figure 2. Dependence of the depolarization on the absorbed pump power for the (111), (100), and (110) planes when $r_a = r_0/5$.

VIII-B-3 The Effect of Nd Concentration on the Spectroscopic and Emission Decay Properties of Highly-Doped Nd:YAG Ceramics

LUPEI, Voicu¹; LUPEI, Aurelia¹; GEORGESCU, Serban¹; TAIRA, Takunori; SATO, Yoichi; IKESUE, Akio²

(¹IAP-NILPRP, Romania; ²JFCC)

[*Phys. Rev. B* **64**, 092102 (2001)]

The renewed interest in the use of highly concentrated Nd:YAG laser materials for constructing solid state lasers rises important questions concerning the effect of Nd concentration (C_{Nd}) on the spectroscopic and emission decay characteristics that determine the performances of these lasers. Highly doped Nd:YAG components can be produced by various techniques such as crystal growth by the Thermal Gradient Technique,¹⁾ flux,²⁾ epitaxial thin film deposition³⁾ or ceramic techniques.⁴⁾ Despite of the fact that some of these components have been used in laser experiments, no detailed account of the effect of C_{Nd} on their spectro-

copious and emission decay properties has been reported. This work reports the results of spectroscopic and emission decay investigations of Nd:YAG ceramics with up to 9-at.% Nd.

High optical quality transparent Nd:YAG ceramics have been produced by the technique described in Reference 4). The high-resolution transmission spectra were measured at temperatures between 10 and 300 K by using a high-resolution (better than 0.3 cm^{-1}) one-meter double monochromator. For the emission decay a photon counting technique of 20-ns resolution was used and the excitation was made non-selectively at room temperature with the 2nd harmonic of a Q-switched Nd:YAG laser (10-nsec pulse width). The intensity of excitation was kept low in order to avoid a high population of the emitting level $^4F_{3/2}$ (under $\sim 1\%$) that could favor upconversion by excited state absorption or energy transfer.

The transmission spectra of Nd:YAG ceramic samples of 1-at.% Nd are similar to those of single crystals⁵⁾ of the same C_{Nd} . No obvious line shifts or broadenings have been observed in any spectral range in agreement with previous investigations on 1-at.% Nd:YAG ceramics.⁶⁾ With increasing Nd concentration the positions of the spectral lines remain practically unchanged with very slight shifts for some of the optical transitions and with a selective broadening. The structures of the satellites in the low-temperature high-resolution spectra at 1-at.% Nd do not contain any additional satellites with respect to those reported in single crystals,⁵⁾ showing that no additional defects in the vicinity of the Nd ions occur. The only major satellites in the transmission spectra of the Nd:YAG ceramics are those connected with crystal-field perturbations inside of statistical ensembles of Nd^{3+} ions sitting on near lattice sites. At low Nd concentrations the most important of such ensembles are Nd ion pairs: the satellites corresponding to the first (*n.n.*)- and second (*n.n.n.*)- order pairs are clearly resolved in most of the optical transitions (satellites M_1 , spectral shift up to 5 to 6 cm^{-1} and M_2 , shift up to 2 to 3 cm^{-1} , respectively), as shown in Figure 1 for the transition $^4I_{9/2}(Z_1) \rightarrow ^2P_{1/2}$ at various Nd concentrations. With increasing of C_{Nd} the relative intensities of the pair lines increase, while the ones of the isolated ions decrease. Moreover, at very high concentrations, new satellites T, whose relative intensities increase with C_{Nd} faster than those of the pairs, show up. Most likely these new satellites are connected with triads of Nd^{3+} ions on near lattice sites, the larger spectral shift being consistent with the expected larger mutual crystal-field perturbation inside of these ensembles.

The weakly excited emission decay at room temperature is accelerated and shows departures from exponentials with increasing C_{Nd} (as shown in Figure 2) The decay can be divided into four successive temporal regions: (i) a very sharp drop that terminates practically within the first two microseconds of the decay and whose extent on the intensity scale increases almost proportionally to C_{Nd} ; (ii) a quasi-exponential portion that blurs at high C_{Nd} ; (iii) a non-exponential dependence; (iv) a new quasi-exponential dependence. The border between these regions is not sharp and the transition is gradual. The extent of the regions (ii) and (iii)

reduces with increasing C_{Nd} : the region (iv) is not seen in the decay of the diluted samples during 6–8 e-foldings of low noise decay at the low pump intensities used in this experiment. The emission quantum efficiency η_{qe} in the presence of energy transfer can be then determined. It decreases with increasing C_{Nd} and all the excitation lost non-radiatively by cross-relaxation is transformed into heat. This limits the possibilities of using concentrated Nd:YAG components in laser emission regimes implying the storage of excitation energy (the Q-switched regime). However, these materials show good prospect to be used in continuous-wave regimes, where the effect of the reduction of η_{qe} with increasing C_{Nd} on the threshold can be compensated by an enhanced absorption of the pump radiation.

References

- 1) Y. Zhou, *J. Crystal Growth* **78**, 31 (1986).
- 2) P. Gavrilovic, M. S. O'Neill, J. H. Zarabi, J. E. Williams, W. H. Grodkiewicz and B. Bruce, *Appl. Phys. Lett.* **65**, 1820 (1994).
- 3) D. Pelenc, B. Chambaz, I. Chartier, B. Ferrand and J. C. Vial, *J. Phys. (France) IV* **1**, 311 (1991).
- 4) A. Ikesue, T. Kinoshita, K. Kamata and K. Yoshida, *J. Am. Ceram. Soc.* **78**, 1033 (1995).
- 5) V. Lupei, A. Lupei, C. Tiseanu, S. Georgescu, C. Stoicescu and P. Nanau, *Phys. Rev. B* **51**, 8 (1995).
- 6) M. Sekita, H. Haneda, T. Yanagitani and S. Shirasaki, *J. Appl. Phys.* **67**, 453 (1990).

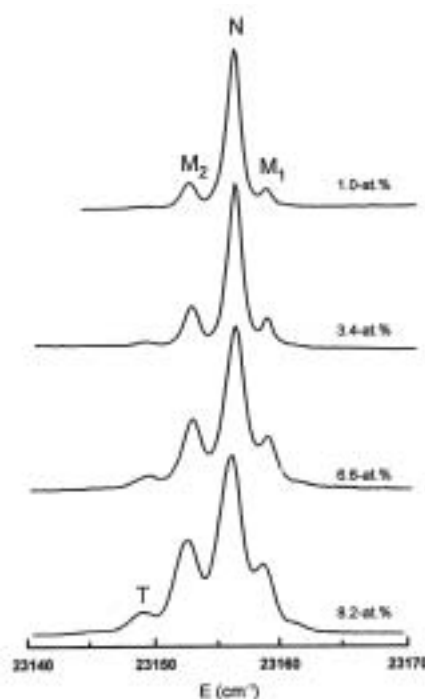


Figure 1. $^4I_{9/2} \rightarrow ^2P_{1/2}$ transmission spectra for different concentrations at low temperature.

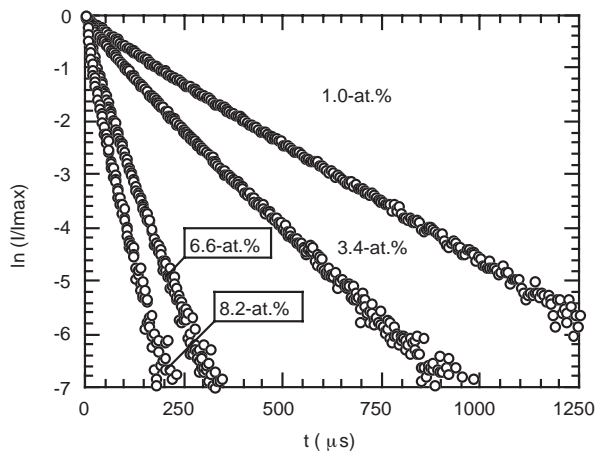


Figure 2. ${}^4F_{3/2}$ emission decays for Nd:YAG ceramics of different concentrations at room temperature.

VIII-B-4 Spectroscopy and Laser Emission under Hot Band Resonant Pumping in Highly Doped Nd:YAG Ceramics

LUPEI, Voicu¹; TAIRA, Takunori; LUPEI, Aurelia¹; PAVEL, Nicolaie; SHOJI, Ichiro; IKESUE, Akio²

(¹IAP-NILPRP, Romania; ²JFCC)

[*Opt. Commun.* **195**, 225 (2001)]

Owing to important thermo-mechanical properties, such as hardness, high thermal conductivity and high stress-fracture limit as well as to its fairly good spectroscopic properties (four-level laser scheme, high emission cross-section, fairly long lifetime), Nd:YAG remains a material of choice for the construction of solid-state lasers. However, the inability of the conventional growth techniques for bulk single-crystals (Czochralski) to incorporate Nd concentrations (C_{Nd}) above 1.2–1.4 at.% without a serious deterioration of the optical and structural properties, together with the sharp and relatively weak absorption lines at these concentrations limit the use of these crystals both in the direction of the high power lasers and of very efficient microchip lasers. This paper investigates the spectroscopic properties and the emission dynamics of Nd^{3+} ions in highly concentrated Nd:YAG ceramics. The implication of these properties on the laser emission is discussed and illustrated with the 1064-nm emission under hot band resonant pump in the emitting level.

The samples under study are Nd:YAG ceramics with Nd concentrations up to 9-at.%, produced as described in Reference 1). The main techniques of investigation are the high spectral resolution optical transmission and the high temporal resolution emission decay. The laser emission was investigated on samples of up to 3.8-at.% Nd under Ti:Sapphire laser end-pumping.

The transmission spectra at room temperature enable the selection of optical transitions suitable for diode laser pumping. A very promising such transition could be the doubly-peaked band centered around 885 nm made up by the hot bands $Z_2 \rightarrow R_1$ and $Z_3 \rightarrow R_2$ of the absorption ${}^4I_{9/2} \rightarrow {}^4F_{3/2}$. Our measurements show that the absorption coefficients of the two peaks of the 885-

nm band are approximately equal at room temperature and become appreciable at high values of C_{Nd} : they increase from $\sim 1.7 \text{ cm}^{-1}$ at 1-at.% Nd to $\sim 6.5 \text{ cm}^{-1}$ at 4-at.% and 13 to 14 cm^{-1} at 9-at.% Nd, while the FWHM increases from $\sim 2.5 \text{ nm}$ at 1-at.% Nd to $\sim 3.2 \text{ nm}$ at 9-at.% Nd, very suitable for diode laser pumping.

The room temperature global emission decay under low intensity non-selective pump of Nd:YAG ceramic samples show C_{Nd} -dependent departures from exponential.²⁾ The quantum efficiency η_{qe} , which was determined as a function of C_{Nd} by using the energy transfer parameters obtained from the emission decay, is shown in Figure 1. This dependence is different from that used traditionally $\eta_{qe} = [1 + C_{Nd}/C_0]^{-1}$, which is based on a C_{Nd}^2 -dependence of the transfer function at all Nd concentrations, but is in a very good agreement with the reported data on quantum efficiency,³⁾ fractional thermal load⁴⁾ and pump-induced birefringence.⁵⁾ These results indicate that the concentrated Nd:YAG ceramics show potential for construction of efficient CW solid state lasers.

The CW 1064-nm laser emission potential of the concentrated Nd:YAG ceramics was investigated under resonant pump in ${}^4F_{3/2}$ level at 885-nm in an end-pump laser configuration. The Nd concentration of the laser active component was 3.8-at.%; the quantum efficiency η_{qe} was ~ 0.32 , leading to a figure of merit $\eta_{qe}C_{Nd}$ of 1.21 and to a calculated product $\eta_{qe}\tau_D$ of $\sim 83 \mu\text{sec}$. The uncoated plane parallel 1.5-mm thick active component was placed in a 25-mm plane-concave resonator with a 50-mm radius output coupler. The end pumping was made with a Ti:sapphire laser focused on the sample in a 160- μm diameter spot. The emission power versus the absorbed power is represented in Figure 2. For a 5% transmission output coupler the threshold of emission in absorbed power was $\sim 65 \text{ mW}$ and the slope efficiency $\sim 40\%$, and at 500-mW absorbed power the laser emitted in excess of 167-mW in a beam with a M^2 factor equal to 1.61.6. Analysis of these data shows that for a given output coupler transmission T , the threshold and the slope efficiency can be consistently described by using the same value of the global loss parameter $(T + L)\eta_B^{-1}$, where η_B is the superposition factor of the laser mode and the pump volumes and L represents all the other losses, including the residual Fresnell loss at the wavelength of emission. This global loss parameter amounts to 0.10.005 for $T = 0.05$ and 0.045 ± 0.002 for $T = 0.01$; these two values are consistent with a superposition factor of ~ 0.73 , in agreement with the measured ratio of the laser emission and the pump beam diameters, and with a loss parameter $L = 0.023$.

In conclusion the laser emission of a 3.8-at.% Nd ceramic laser component under hot band resonant pump at 885-nm with a Ti:sapphire laser is demonstrated. The laser active component used in this experiment is the most concentrated Nd:YAG active component reported to lase at 1064 nm. The performances of this laser could be improved by using coated active components of higher optical quality.

References

- 1) A. Ikesue, T. Kinoshita, K. Kamata and K. Yoshida, *J. Am. Ceram. Soc.* **78**, 1033 (1995).
- 2) V. Lupei, A. Lupei, S. Georgescu, T. Taira, Y. Sato and A.

- Ikesue, *Phys. Rev. B* **64**, 092102 (2001).
 3) K. K. Deb, R. G. Buser and J. Paul, *Appl. Opt.* **20**, 1203 (1981).
 4) T. Y. Fan, *IEEE J. Quantum Electron.* **29**, 1457 (1993).
 5) I. Shoji, Y. Sato, S. Kurimura, T. Taira, A. Ikesue and K. Yoshida, *Advanced Solid State Lasers Conference*, Seattle-USA, Jan. 2001, paper ME14.

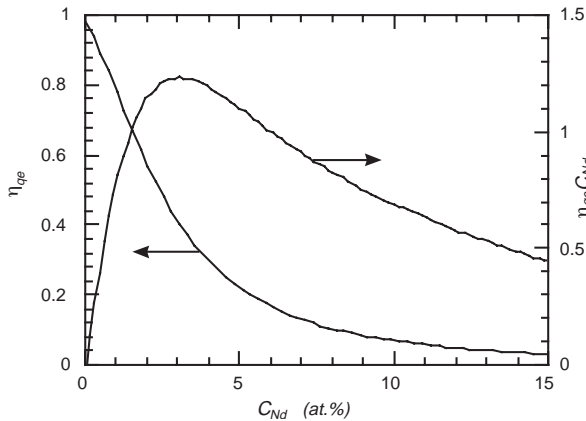


Figure 1. Calculated concentration dependence of emission quantum efficiency η_{qe} and of $\eta_{qe}C_{Nd}$ parameter.

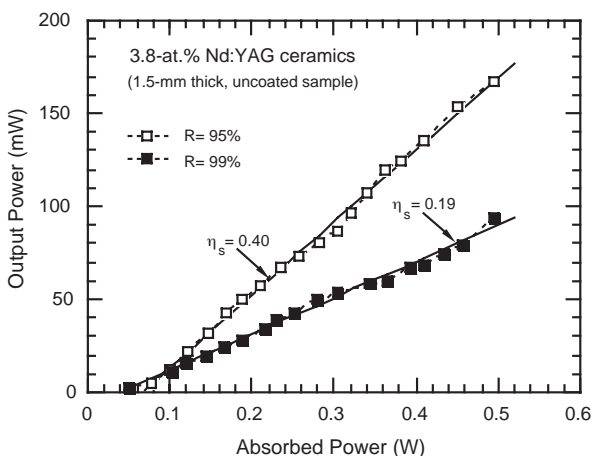


Figure 2. Output power function of absorbed power for an uncoated 3.8-at.% Nd:YAG ceramics sample under 885-nm end pumping by Ti:sapphire laser.

VIII-B-5 Efficient Laser Emission in Concentrated Nd Laser Materials under Pumping into the Emitting Level

LUPEI, Voicu¹; PAVEL, Nicolaie²; TAIRA, Takunori
 (¹IAP-NILPRP, Romania; ²IMS and IAP-NILPRP, Romania)

[*IEEE J. Quantum Electron.* **38**, 240 (2002)]

The enhancement of overall efficiency, low transverse-mode laser emission in miniature lasers, and scaling to high powers are among the most important directions in the development of solid-state lasers. The first of these implies an increase of slope efficiency and a reduction of emission threshold; the second relies on increased absorption of the pump while the third imposes the reduction on heat generation. A suitable

choice of the laser material, with optimised spectroscopic and thermo-mechanical properties, of the optical pumping scheme or of the laser design is then crucial. There is no laser material to fulfill optimally all these requirements and thus the choice is limited within well-defined segments of performance.

The present paper shows that a means to overcome weak pump absorption on transitions directly to the $^4F_{3/2}$ level in the diluted (~ 1 -at.%) Nd laser-materials is to increase the Nd concentration (C_{Nd}). The use of concentrated Nd laser materials requires the examination of several important basic aspects such as the state of Nd ions in YAG samples produced by various techniques, and the effect of C_{Nd} on the spectroscopic and population dynamics properties, in order to select new transitions suitable for pumping and to determine the range of C_{Nd} adequate for laser emission. The Nd:YAG ceramic samples used in this investigation have up to 9-at.% Nd and were supplied by the Japan Fine Ceramics Center, Nagoya, Japan, while the Nd:YAG crystals (2.4 and 3.5-at.%) and Nd:YVO₄ crystals (1, 2, and 3-at.%) were purchased.

The pumping at 885 nm in Nd:YAG reduces the quantum defect with respect to the 808-nm pumping into $^4F_{5/2}$ by about 30% in the case of 1064-nm emission and by $\sim 58\%$ for 940-nm emission, thus contributing to a considerable reduction in the fractional thermal load. Thus, the near degeneracy of the $Z_2 \rightarrow R_1$ and $Z_3 \rightarrow R_2$ absorption lines could be useful for the occurrence of absorption bands suitable for direct diode laser pumping into the $^4F_{3/2}$ state. This near degeneracy takes place in many Nd laser materials and it could help to get more efficient or more powerful emission even from laser active components with good spectroscopic characteristics but poorer thermo-mechanical properties. In the case of Nd:YVO₄, no accidental degeneracy of the thermally-activated transitions occurs. However, for this material the absorption line $Z_1 \rightarrow R_1$ at 879.8 nm has a FWHM similar to the traditional pump transition $Z_1 \rightarrow ^4F_{5/2}(1)$ at 808.6 nm, while the peak absorption coefficient is only 40–50% smaller. This reduction can be easily compensated by an increase in C_{Nd} . Thus in the case of Nd:YVO₄, the transition $Z_1 \rightarrow R_1$ of the $^4I_{9/2} \rightarrow ^4F_{3/2}$ absorption can be used for direct pumping into the emitting level, leading to a reduction of the quantum defect with respect to 808.6-nm pump by 27.4% in the case of 1064-nm $^4F_{3/2} \rightarrow ^4I_{11/2}$ emission and by 65.6% for 915-nm $^4F_{3/2} \rightarrow ^4I_{9/2}$ emission.

For Nd:YVO₄ the effects of the energy transfer on the emission decay are very poorly characterized and an analysis similar to YAG^{1,2)} is not possible at the present time. However, the investigation of emission decay in Nd:GdVO₄ (a crystal similar with YVO₄) gives energy transfer parameters about two times larger than in Nd:YAG.³⁾ Moreover, the investigation of the pump intensity effect on laser emission in Nd:YVO₄ concludes that the up-conversion processes by energy transfer in this crystal are much stronger than in Nd:YAG.⁴⁾ Thus, a stronger decrease of emission quantum efficiency with increased C_{Nd} in Nd:YVO₄ could be expected, although figures of merit $\eta_{qe}C_{Nd}$ larger than for 1-at.% Nd doping could be still obtained for a certain range of higher C_{Nd} .

The 1064-nm laser emission in concentrated

Nd:YAG ceramics and single crystals and in Nd:YVO₄ crystals is investigated using oscillators end pumped by Ti:sapphire laser. Figure 1a shows the laser output power function of the absorbed power for the Nd:YAG ceramic laser components. The most concentrated component to lase under 885-nm pumping was a 0.4-mm thick sample of 6.8-at.% Nd: for the 95% output mirror the slope efficiency (versus the absorbed power) was 20% with the emission threshold of 144 mW. For a 1.5-mm thick 3.8-at.% Nd sample and a 95% output coupler reflectivity the slope efficiency was 42%, the threshold of emission was 58 mW and the output power reaches in excess of 132 mW for 350 mW absorbed pump with a laser beam M² factor of 1.6 × 1.6. The highest slope of 51% was obtained for the output mirror of 90% reflectivity, but with an increased threshold pump power of 115 mW. The laser output power versus the absorbed power for uncoated 2.4-at.% (3.0-mm thick) and 3.5-at.% (1.0-mm thick) Nd:YAG crystals under 885-nm pumping is shown in Figure 1b, in comparison with those of a standard 1-at.% (3.0-mm thick) Nd component. For the 1-at.% Nd:YAG sample the slope efficiency was 0.54 and the threshold absorbed power was 31 mW. A deterioration of these parameters with increasing C_{Nd} was observed: while for the 2.4-at.% Nd:YAG crystal the slope efficiency was 0.50 and the absorbed power at threshold was 45 mW, for the 3.5-at.% Nd:YAG sample the slope efficiency decreased to 0.46 with a threshold absorbed power of 65 mW. Figure 2 presents the laser performances for 0.9-mm thick Nd:YVO₄ components in the configuration E//c-crystal axis and with the 95% reflectivity output coupler. In spite of using uncoated active elements the laser parameters obtained with the 1-at.% Nd sample are substantially improved (slope efficiency of 70% and absorbed pump power at threshold of 21 mW) with respect to those reported in Reference 5) for a thicker sample. For the 2-at.% Nd component the threshold of emission in absorbed power was 44 mW, the slope efficiency reached 67% and for 420-mW absorbed power the laser emitted 265 mW at 1064 nm. A slope efficiency of 58% and a threshold of 58 mW absorbed power were determined for the 3-at.% Nd:YVO₄ sample. The residual losses L were determined as ~0.005, 0.01 and ~0.016 for the 1, 2, and 3-at.% Nd:YVO₄ crystals, respectively.

In conclusions, the investigation of the effect of Nd concentration on emission decay of Nd:YAG indicates that up to quite high concentrations the reduction of the emission quantum efficiency by self-quenching can be compensated by the increase of pump absorption. Efficient CW laser emission is demonstrated under direct pumping into the ⁴F_{3/2} emitting level of Nd:YAG crystals with up to 3.5-at.% Nd, Nd:YAG ceramics with up to 6.8-at.% Nd, and Nd:YVO₄ crystals with up to 3-at.% Nd. Superior performance as compared to traditional pumping into the ⁴F_{5/2} state were obtained. It is inferred that direct pumping into the emitting level of concentrated Nd materials can improve the efficiency of solid-state lasers in the free-generation or low-storage regimes and opens the possibility of scaling these lasers to high powers.

References

- 1) V. Lupei, A. Lupei, S. Georgescu, T. Taira, Y. Sato and A. Ikesue, *Phys. Rev. B* **64**, 092102 (2001).
- 2) V. Lupei, A. Lupei, N. Pavel, T. Taira, I. Shoji and A. Ikesue, *Appl. Phys. Lett.* **79**, 590 (2001).
- 3) V. Ostroumov, T. Jensen, J. P. Meyn, G. Huber and M.A. Noginov, *J. Opt. Soc. Am. B* **15**, 1052 (1998).
- 4) Y.F. Chen, C.C. Liao, Y.P. Lan and S.C. Wang, *Appl. Phys. B* **70**, 487 (2000).
- 5) R. Lavi, S. Jackel, Y. Tzuk, M. Winik, E. Lebiush, M. Katz and I. Paiss, *Appl. Opt.* **38**, 7382 (1999).

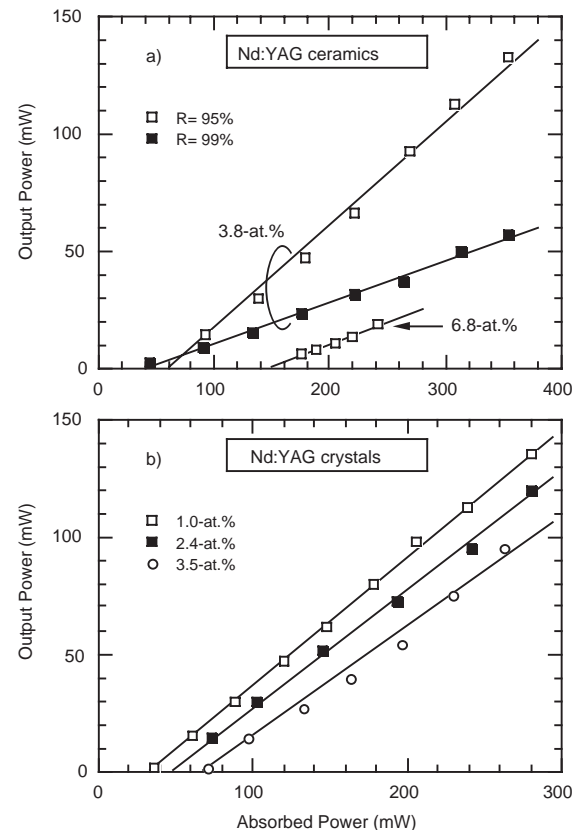


Figure 1. 1064-nm laser emission characteristics for (a) uncoated 3.8 and 6.8-at.% Nd:YAG ceramics and for (b) uncoated Nd:YAG crystals under 885-nm pumping.

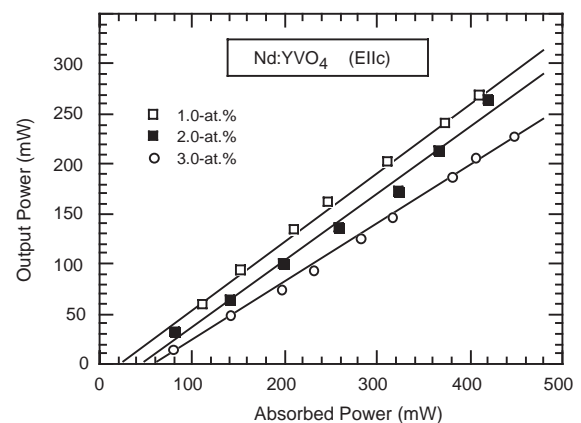


Figure 2. Comparative 1064-nm laser performances for Nd:YVO₄ components under 880-nm pumping (E//c-crystal axis) with a 95% reflectivity output coupler.

VIII-B-6 1064-nm Laser Emission of Highly Doped Nd:Yttrium Aluminium Garnet under 885-nm Diode Laser Pumping

LUPEI, Voicu¹; PAVEL, Nicolaie²; TAIRA, Takunori

(¹IAP-NILPRP, Romania; ²IMS and IAP-NILPRP, Romania)

[*Appl. Phys. Lett.* **80**, 4309 (2002)]

Owing to the high optical-to-electrical efficiency and to the ability to excite resonantly the energy levels of the laser active ions, the diode laser pumping has a major role in increasing the efficiency of the solid-state lasers. The resonant excitation of Nd³⁺ emission was demonstrated at early stages of laser development by exciting Nd:CaWO₄ directly into the emitting level on the transition $^4I_{9/2} (Z_2) \rightarrow ^4F_{3/2} (R_2)$ by the 880-nm recombination radiation of GaAs diodes.¹⁾ The first diode laser pumped Nd:YAG lasers in transverse²⁾ or longitudinal³⁾ pumping configurations used the direct excitation of the emitting level on the 869-nm transition $^4I_{9/2} (Z_1) \rightarrow ^4F_{3/2} (R_2)$. Due to the weak absorption on this transition and to the lack of suitable pump diodes, the 869-nm pumping was soon replaced by the 808-nm pumping into the stronger absorption $^4I_{9/2} (Z_1) \rightarrow ^4F_{5/2} (S_1)$. Unfortunately, this introduces a parasitic upper quantum defect between the pump- and the emitting laser levels that contributes to the reduction of the laser emission parameters and to the generation of heat by non-radiative processes in the pumped laser material.

The pumping into the emitting level of Nd-doped materials has received a renewed attention in the last few years: in case of Nd:YAG successful attempts have been made with diluted (~1-at.% Nd) single crystals under Ti:sapphire or diode laser pumping^{4),5)} and with highly-doped ceramics or single crystals^{6),7)} under Ti:sapphire pump. This paper demonstrates CW laser emission of highly doped Nd:YAG ceramics (up to 3.5-at.% Nd) and single crystals (up to 3.8-at.% Nd) under 885-nm diode laser pumping. The laser emission of a 2.4-at.% Nd:YAG single crystal passively Q-switched with a Cr⁴⁺:YAG saturable absorber under CW diode laser pumping at 885 nm is also reported.

A fiber array packed diode bars FAP-81-16C-800B laser (Coherent Co.) whose output is delivered in a 19-fiber bundle confined within an 800- μ m diameter aperture with NA = 0.15 was used as pumping source. With a collimating achromatic lens of 60-mm focal length and a focusing achromatic lens of 50-mm focal length the end face of the fiber bundle was imaged into the laser active components in a 780- μ m diameter spot. The laser active components were Nd:YAG single crystals of 1-at.% (3-mm thick), 2.4-at.% (3-mm thick) and 3.5-at.% Nd (1.0-mm thick) and Nd:YAG ceramics of 3.8-at.% Nd (1.5 and 2.5-mm thick), AR coated on both sides for 885 and 1064 nm. A plane-concave resonator of 50 mm length with an output mirror of 0.25-m radius of curvature was used. The active component was placed close to the rear mirror, which was coated HR for 1064 nm and HT for the pumping wavelength.

Figure 1a shows the laser performances for the 2.4-at.% Nd:YAG crystal. The maximum slope efficiency of

0.64 was obtained for a 90% reflectivity output mirror, with a corresponding emission threshold 1.51 W. The slope efficiency and the threshold become 0.62 and 0.87 W for 95% reflectivity and 0.26 and 0.25 mW for 99% reflectivity. The output power obtained with 95% reflectivity output mirror for the laser materials used in this experiment is presented in Figure 1b: the best results, i.e. a slope efficiency of 0.67 and 0.71 W absorbed power at threshold, were obtained with the 1.0-at.% Nd:YAG crystal of 3.0-mm thickness. The laser parameters vs. incident power reveal the practical advantages of the concentrated materials: for the region close to the maximum operating point, where the diode wavelength is ~ 885 nm, the measured slope efficiency in input power for the 3-mm thick crystals is 0.26 for 1-at.% Nd and 0.43, i.e. by 65% larger, for 2.4-at.% Nd. At the same time the emission threshold is by ~ 40 % lower for the second crystal and the absorption efficiency is larger by ~ 75%.

The passive Q-switching regime was investigated with Cr⁴⁺:YAG saturable absorber (SA) crystals. A plane-plane resonator with the active medium positioned near the rear mirror and the SA crystal placed closed of the output mirror was investigated. Figure 2 shows the average power vs. the absorbed power for a 70-mm length resonator. With a Cr:YAG SA of 90% initial transmission (T_0) and an output mirror of 95% reflectivity an average output power of 0.95 W resulted for 5.2-W absorbed power. The maximum repetition rate was 7.1 kHz with the pulse width 37.5 ns over the entire range of absorbed power: this corresponds to a maximum pulse energy of 134 μ J and ~ 3.6 kW peak power. With a 90% reflectivity output mirror the average power decreases to 0.84 W; the pulse width reduces to 26.5 ns, corresponding to ~ 161- μ J pulse energy and ~6 kW peak power. With a Cr:YAG SA of $T_0 = 85%$ and a 95% reflectivity output mirror the laser emitted max. 0.56-W average power at 3.2-kHz repetition rate: the pulse had 175 μ J energy and 5.6-kW peak power. In spite of using a non-optimised scheme, improved laser characteristics (lower threshold, higher average power and pulse energy) resulted compared with a 1.1-at.% composite Nd:YAG laser passively Q-switched by Cr:YAG under 808-nm diode pumping.⁸⁾

In conclusion, highly efficient 1064-nm CW laser emission under 885-nm diode pumping in concentrated Nd:YAG crystals (up to 3.5-at.% Nd) and ceramics (up to 3.8-at.% Nd) is reported. First highly doped (2.4-at.%) Nd:YAG laser passively Q-switched by a Cr⁴⁺:YAG saturable absorber is demonstrated.

References

- 1) R. Newman, *J. Appl. Phys.* **34**, 437 (1963).
- 2) M. Ross, *Proc. IEEE* **56**, 196 (1968).
- 3) L. J. Rosenkrantz, *J. Appl. Phys.* **34**, 4603 (1972).
- 4) R. Lavi and S. Jackel, *Appl. Opt.* **39**, 3093 (2000).
- 5) R. Lavi, S. Jackel, A. Tal, E. Lebiush, Y. Tzuk and S. Goldring, *Opt. Commun.* **195**, 427 (2001).
- 6) V. Lupei, A. Lupei, N. Pavel, T. Taira, I. Shoji and A. Ikesue, *Appl. Phys. Lett.* **79**, 590 (2001).
- 7) V. Lupei, N. Pavel and T. Taira, *Opt. Lett.* **26**, 1678 (2001).
- 8) N. Pavel, J. Saikawa, S. Kurimura and T. Taira, *Jpn. J. Appl. Phys.* **40**, 1253 (2001).

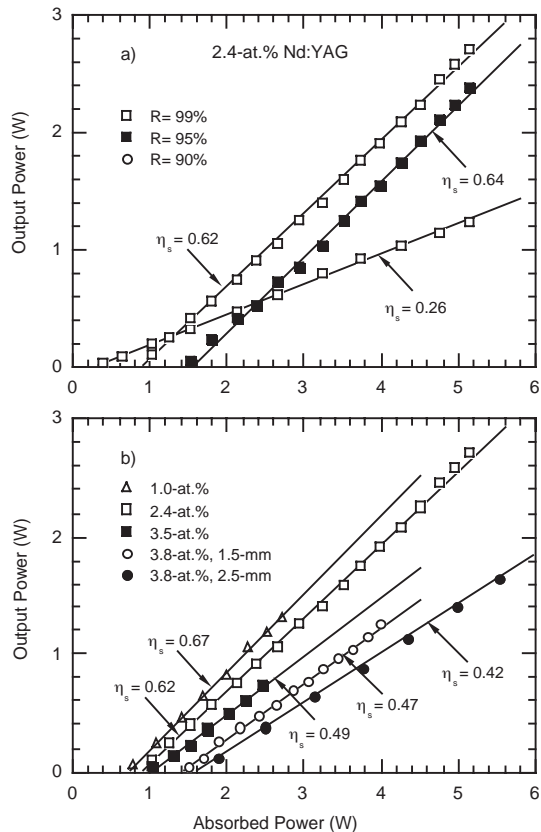


Figure 1. 1064-nm laser emission characteristics for (a) a 2.4-at.% Nd:YAG crystal and for (b) the Nd:YAG laser active components used in experiments and a 95% reflectivity output mirror under 885-nm diode laser pumping.

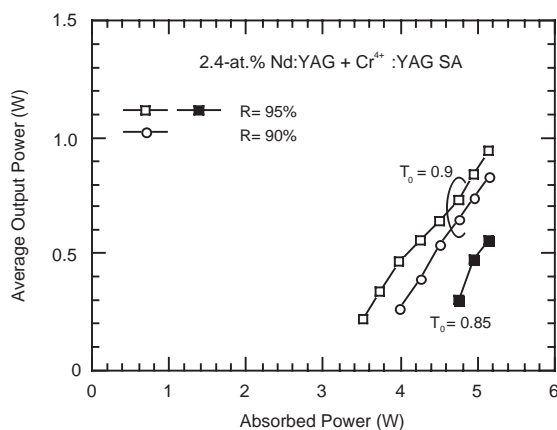


Figure 2. Average output power of a CW diode pumped at 885 nm highly-doped (2.4-at.% Nd:YAG laser passively Q-switched by Cr⁴⁺:YAG saturable absorber.

VIII-B-7 Diode Edge-Pumped Microchip Composite Yb:YAG Laser

DASCALU, Traian; TAIRA, Takunori; PAVEL, Nicolaie

[*Jpn. J. Appl. Phys.* **41**, 606 (2002)]

High power microchip laser based on Yb³⁺ doped materials has been recognized as very useful in the ultrafast-laser field.^{1,2)} Thermal effects in the laser gain

medium generally limit power scaling of diode-pumped solid-state microchip lasers. Yb:YAG is a gain medium that has improved properties relative to Nd³⁺-doped gain media³⁾ for addressing this issue and efficient room-temperature laser operation (slope efficiency of 65%) has been demonstrated in this material despite the fact that it is a quasi-four-level laser.⁴⁾ Besides of choice of gain medium the configuration that is chosen for pumping, cooling, and extraction plays a critical role in power scaling of microchip laser. Despite of the Yb:YAG low quantum defect, large thermal effects occur at high pumping power. One solution to diminish the thermal lens is to orient the heat flux collinearly with the direction of laser propagation. We propose an edge pumped Yb:YAG microchip scheme. This scheme can be used efficiently only if the pumping power is concentrated into a small region of the microchip consequently a composite material was designed.

The composite material consists in an Yb:YAG core of hexagonal or square shape surrounded by circular shaped undoped YAG. The composite crystal consists of an Yb:YAG doped core surrounded by an undoped YAG region, the core and the undoped crystal being diffusion bonded. The crystal has one side high reflectivity (HR) coated at the laser wavelength and the opposite side anti reflection (AR) coated and it is mounted with its HR coated side on a highly effective micro channel cooling system, Figure 1. Two fiber-coupled diode lasers delivering more than of 100 W at 940 nm are used for pumping. Inside of the microchip the pumping beam propagates by total internal reflection and intersects the Yb:YAG core where it is partially absorbed.

Continuous laser operation was obtained from the 2 at% Yb doped crystal by using an optical resonator of 50-mm length with output coupler of 100-mm radius of curvature and 97% reflectivity output mirror. The slope efficiency for laser operation at more than three times above the threshold is 50% and the laser delivers maximum 1.8 W output power for 5.1 W absorbed power.

In order to evaluate the laser performances under low thermal effects the microchip was operated in quasi-CW mode with a duty factor of 2.5% and 2.4 Hz repetition rate. Figure 2 presents the output vs. input power for the 10-at. % doped sample with 97% reflectivity output mirror. Laser emission with 42% slope efficiency and 41-W output peak power at 220-W input power was demonstrated. The experiments show the potential of the microchip laser to be scaled in the range of tens of watts output power.

References

- 1) C. Honninger, R. Paschotta, M. Graf, F. Morier-Genoud, G. Zhang, M. Moser, S. Biswal, J. Nees, A. Braun, G.A. Mourou, A. Giesen, W. Seeber and U. Keller, *Appl Phys. B* **69**, 3 (1999).
- 2) C. Honninger, I. Johannsen, M. Moser, G. Zhang, A. Giesen and U. Keller, *Appl. Phys. B* **65**, 423 (1997).
- 3) L.D. DeLoach, S.A. Payne, L.L. Chase, L.K. Smith, W.L. Kway and W.F. Krupke, *IEEE J. Quantum Electron.* **29**, 1179 (1993).
- 4) K. Contag, M. Karzewski, C. Stewen, A. Giesen and H. Hugel, *Quantum Electronics* **29**, 697 (1999).

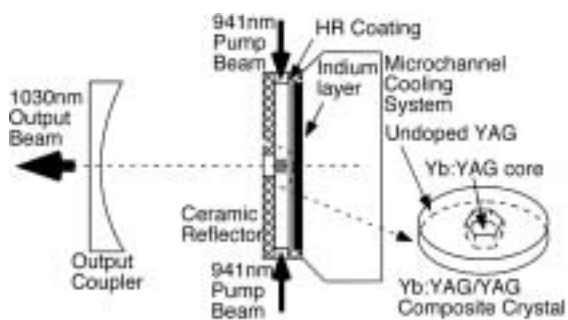


Figure 1. The diode radial-pumped composite Yb:YAG microchip laser.

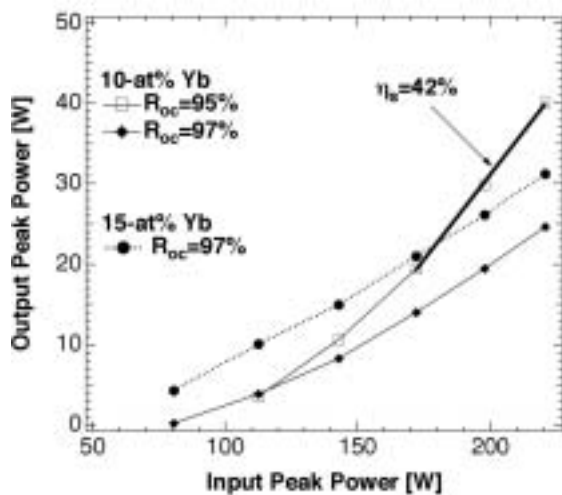


Figure 2. Output power vs. input power for quasi CW laser operation for 10-at. % Yb-doping crystal, $2 \times 2 \text{ mm}^2$ square core dimensions and 15-at. % Yb-doping crystal, $1.2 \times 1.2 \text{ mm}^2$ square core dimensions. Here R represents the output mirror reflectivity.

Research Center for Molecular-Scale Nanoscience

VIII-C Development of Organic Semiconductors for Molecular Thin-Film Devices

Organic light-emitting diodes (OLEDs) and organic field-effect transistors (OFETs) based on π -conjugated oligomers have been extensively studied as molecular thin-film devices. Organic semiconductors with low injection barriers and high mobilities are required for highly efficient OLEDs and OFETs. Radical cations or anions of an organic semiconductor have to be generated easily at the interface with an electrode (or a dielectric), and holes or electrons must move fast in the semiconducting layer. Compared with organic *p*-type semiconductors, organic *n*-type semiconductors for practical use are few and rather difficult to develop. Recently, we found that perfluorinated oligomers are efficient electron-transport materials for OLEDs.

VIII-C-1 Perfluoro-1,3,5-tris(*p*-Oligophenyl)benzenes: Amorphous Electron-Transport Materials with High Glass-Transition Temperature and High Electron Mobility

KOMATSU, Shingo; SAKAMOTO, Youichi;
SUZUKI, Toshiyasu; TOKITO, Shizuo¹
(¹NHK Sci. Tech. Res. Labs.)

[*J. Solid State Chem.* in press]

Perfluoro-1,3,5-tris(*p*-quaterphenyl)benzene (**PF-13Y**) and perfluoro-1,3,5-tris(*p*-quinquephenyl)benzene (**PF-16Y**) have been synthesized and characterized. They showed higher glass transition temperatures compared with perfluoro-1,3,5-tris(*p*-terphenyl)benzene (**PF-10Y**). Organic light-emitting diodes (OLEDs) were fabricated using these materials as the electron-transport layers. **PF-13Y** and **PF-16Y** are better electron-transporters than **PF-10Y**. The electron mobilities of **PF-10Y** and Alq₃ were measured by the time-of-flight technique. **PF-10Y** showed higher electron mobilities (10^{-4} cm²/Vs) and weaker electric field dependence compared with Alq₃.

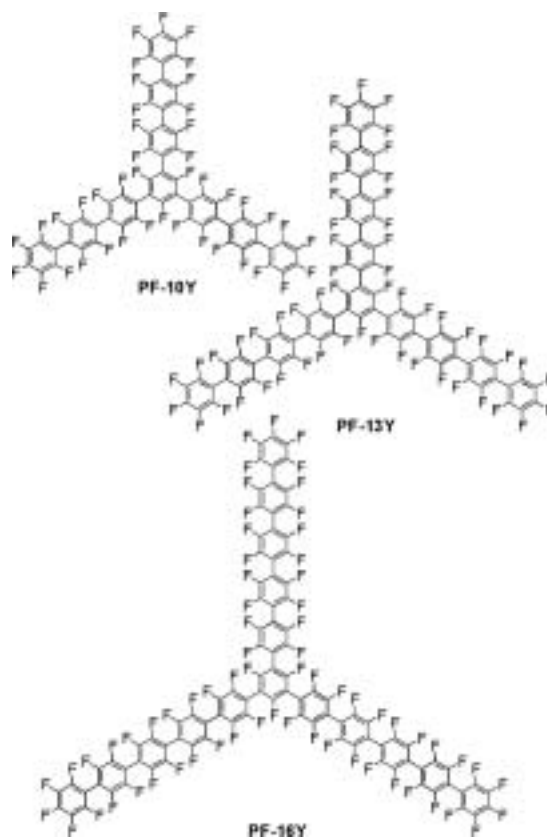


Figure 1. Perfluoro-1,3,5-tris(*p*-oligophenyl)benzenes.

VIII-C-2 Synthesis and Properties of Iridium Complexes Bearing Perfluoroaryl-Substituted 2-Phenylpyridine

SHIRASAWA, Nobuhiko; SAKAMOTO, Youichi;
SUZUKI, Toshiyasu; TSUZUKI, Toshimitsu¹;
TOKITO, Shizuo¹
(¹NHK Sci. Tech. Res. Labs.)

Perfluorophenyl derivatives of 2-phenylpyridine, 2-(*p*-C₆F₅-phenyl)pyridine (**1a**), 5-C₆F₅-2-phenylpyridine (**1b**), and 5-C₆F₅-2-(*p*-C₆F₅-phenyl)pyridine (**1c**), have been prepared. Their iridium(III) acetylacetonato complexes (**2a-c**) were satisfactorily synthesized in a one-pot reaction of a free ligand and an iridium salt in 2-ethoxyethanol at 105 °C, and the subsequent reaction

with acetylacetonate in the presence of a base at 50 °C for 4 h. When the reaction was carried out at 140 °C, the substitution reaction of fluoride with 2-ethoxyethoxide at para position took place. When applied to OLED devices, compounds **2a-c** showed emissions from greenish yellow to yellow at room temperature with the external quantum efficiency up to 14.7%.

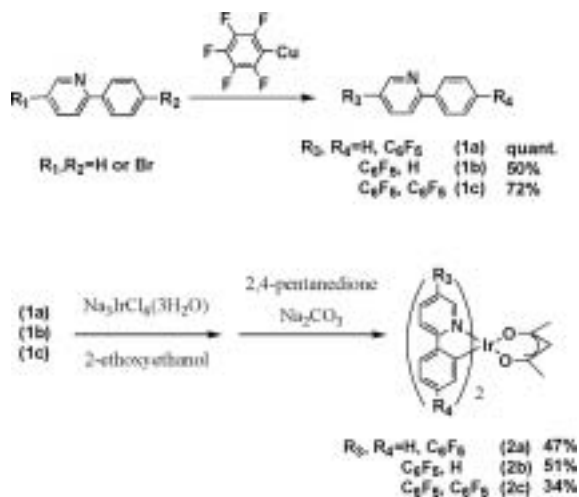


Figure 1. Synthesis of C_6F_5 -substituted ppy and their iridium acac derivatives.

VIII-D Field Effect Transistors with Organic Semiconductors

The mechanism of carrier transport in organic semiconductors and carrier injection from metal electrodes becomes the most important subject to be elucidated for the construction of high performance organic thin film devices. We have studied electrical properties of organic films using field effect transistors.

VIII-D-1 Electrical Characteristics of Phthalocyanine Films Prepared by Electrophoretic Deposition

TAKADA, Masaki¹; YOSHIOKA, Hirokazu²;
TADA, Hirokazu; MATSUSHIGE, Kazumi²
(¹GUAS; ²Kyoto Univ.)

[*Jpn. J. Appl. Phys.* **41**, L73 (2002)]

Electrical properties of phthalocyanine (Pc) films prepared by an electrochemical process were investigated using field effect transistors (FETs). Copper-Pc (CuPc) films were deposited electrophoretically on voltage-applied cathodic electrodes from trifluoroacetic acid/dichloromethane mixed solution containing protonated monomeric CuPc molecules. Optical absorption spectra showed that the CuPc films had α -type polymorphs. The grains grew with reaction time to close a gap between the FET electrodes. FET studies showed that CuPc films after annealing exhibited a *p*-type semiconducting behavior. Carrier mobility, conductivity and carrier density of the films were $1.4 \times 10^{-5} \text{ cm}^2/\text{Vs}$, $7.7 \times 10^{-7} \text{ S/cm}$ and $6.6 \times 10^{16} \text{ cm}^{-3}$, respectively. It is revealed that electrophoretic deposition is applicable for the preparation of active layers in organic electronic devices.

VIII-D-2 BTQBT (bis-(1,2,5-thiadiazolo)-*p*-Quinobis(1,3-dithiole)) Thin Films; A Promising Candidate for High Mobility Organic Transistors

TAKADA, Masaki¹; GRAAF, Harald;
YAMASHITA, Yoshiro²; TADA, Hirokazu
(¹GUAS, ²Tokyo Inst. Tech.)

[*Jpn. J. Appl. Phys.* **41**, L4 (2002)]

BTQBT (bis-(1,2,5-thiadiazolo)-*p*-quinobis(1,3-dithiole)) films have been prepared as active semiconducting layers of organic field effect transistors (FETs). BTQBT films showed a *p*-type semiconducting behavior. The hole mobility and on/off ratio of BTQBT films under ultrahigh vacuum conditions reached to $0.2 \text{ cm}^2/\text{Vs}$ and 10^8 , respectively, by optimization of the growth conditions. These values are in the same order as those of pentacene thin films, which indicates that BTQBT molecules have a great potential for active layers of organic electronic devices.

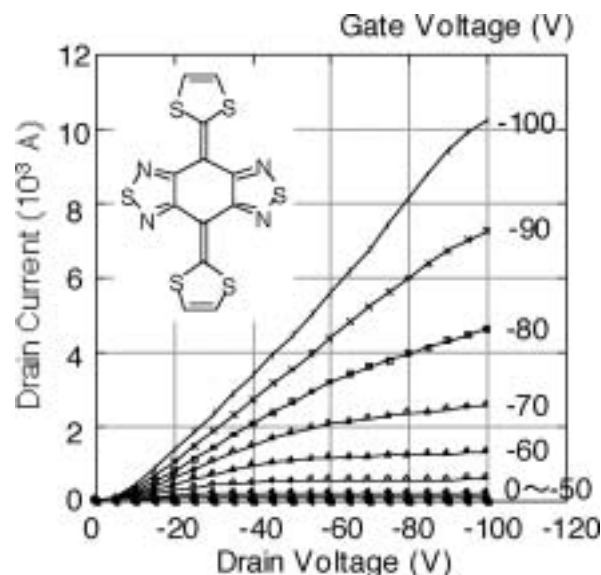


Figure 1. FET characteristics of BTQBT films measured in UHV.

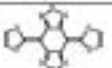
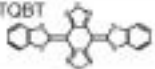
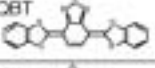
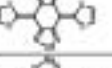
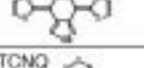
VIII-D-3 Field Effect Transistors of BTQBT and Its Derivatives

TAKADA, Masaki¹; YAMASHITA, Yoshiro²;
TADA, Hirokazu
(¹GUAS; ²Tokyo Inst. Tech.)

[*Proc. MRS 725*, P10.3 (2002)]

We have prepared and characterized thin film field effect transistors (FETs) of bis-(1, 2, 5- thiadiazolo)-*p*-quinobis(1, 3-dithiole) (BTQBT) and its derivatives. Preparation and characterization of the films were carried out under ultrahigh vacuum condition. Most materials examined showed *p*-type semiconducting behaviors. Among *p*-type molecules, BTQBT films deposited at room temperature showed *p*-type semiconducting behaviors with mobility of $0.1 \text{ cm}^2/\text{Vs}$. The on/off drain current ratio was 10^7 . The mobility and on/off ratio reached to $0.2 \text{ cm}^2/\text{Vs}$ and 10^8 , respectively, by optimizing the film growth conditions. These performances are almost comparable to those of pentacene and polythiophene thin films, indicated that BTQBT molecule is a prominent semiconducting material as a high mobility thin film. It was also found that tetracyanoquinodimethane (TCNQ) derivative showed an *n*-type semiconducting behavior with an electron mobility of $8.9 \times 10^{-4} \text{ cm}^2/\text{Vs}$.

Table 1. Field Effect Mobilities of BTQBT and Its Derivatives.

	type	Mobility(cm ² /Vs)	On/off ratio
BTQBT 	p	1.0×10^{-1} (0.2 at 50°C)	10^7
DB-BTQBT 	p	4.6×10^{-4}	10^4
DB-TQBT 	p	1.6×10^{-5}	50
TQBT 	p	1.2×10^{-5}	3
BSQBT 	p	1.3×10^{-6}	10
BTDA-TCNQ 	n	8.9×10^{-4} Al electrodes	10^2

VIII-D-4 Preparation of Nanometer-Gap Electrodes for Field Effect Transistors by Electroplating

YAMADA, Ryo; TAKADA, Masaki¹; OISHI, Osamu; TADA, Hirokazu
(¹GUAS)

A pair of electrodes with a nanometer-scale spacing

was fabricated by electroplating of gold onto micrometer gap electrodes prepared through conventional photolithography. The electrodes were prepared on SiO₂ formed on a heavily doped Si substrate which serves as a gate electrode. Figure 1 shows a SEM micrograph of the electrode fabricated by this method. It was shown that the drain current changed as a function of a gate voltage when Ti-phthalocyanine thin film was deposited onto this electrode. Thus, the electrode made by this method can be used for the study of organic thin film field effect transistors.

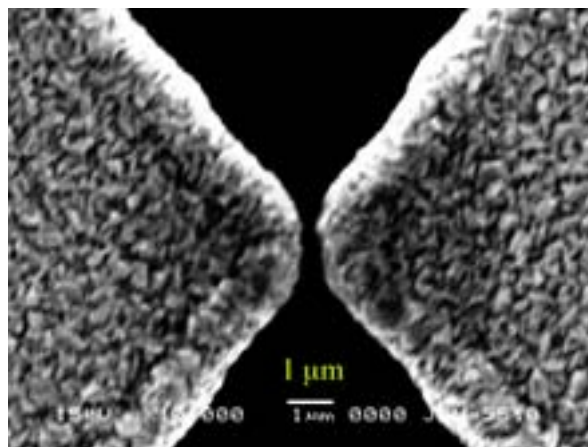


Figure 1. SEM Photograph of Nanometer Gap Electrodes.

VIII-E Preparation and Characterization of Highly Ordered Molecular Films on Silicon Bound with Si–C Covalent Bond

Self-assembled monolayers (SAMs) have received considerable attention because of their potential applications to molecular scale electronic devices. Covalently bond alkane SAMs formed by reaction between alkene and hydrogen terminated silicon are of increasing interest as nano-interface for molecular electronics devices fabricated on silicon microstructures. We have studied the growth manner and electronic structure of Si–C junction using scanning probe microscope such as STM (scanning tunneling microscope), AFM (atomic force microscope) and KFM (Kelvin force microscope).

VIII-E-1 Force Curve Measurement of Self-Assembled Organic Monolayers Bound Covalently on Silicon(111)

GRAAF, Harald; ARA, Masato¹; TADA, Hirokazu
(¹GUAS)

[*Mol. Cryst. Liq. Cryst.* **377**, 33 (2002)]

Self-assembled monolayers of alkyl chains were prepared on silicon(111) surfaces. The surface was characterized by atomic force microscopy (AFM). Atomically flat terraces were observed in topographic images of the films with contact mode AFM, indicating the formation of highly ordered monolayers. Force curve measurements showed that the adhesion force between organic films and gold cantilever was much stronger comparing to the force on hydrogen terminated

surfaces.

VIII-E-2 Atomic Force Microscope Anodization of Si(111) Covered with Alkyl Monolayers

ARA, Masato¹; GRAAF, Harald; TADA, Hirokazu
(¹GUAS)

[*Jpn. J. Appl. Phys.* **41**, 4894 (2002)]

Alkyl monolayers on Si were prepared through the reaction between 1-alkenes and hydrogen-terminated Si by heat treatment. The monolayers were characterized by atomic force microscopy (AFM), force curve and water contact angle measurements. It was found that surface properties were modified by the formation of highly ordered closely packed monolayers. The monolayers were anodized with a contact-mode AFM

by applying voltage between the conductive cantilever and surface under ambient conditions, which resulted in nanometer-scale oxidation of surfaces. After anodization, patterned areas were modified by removing the silicon oxide and terminating the surface of the grooves with hydrogen atoms by NH_4F etching, and by covering the etched surface with 1-octadecene molecules. The monolayers themselves showed high resistance to NH_4F etching and air oxidation.

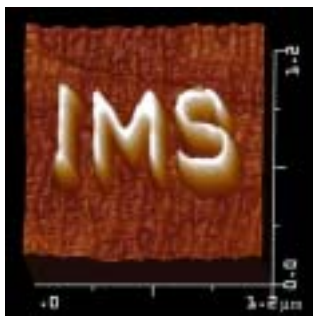


Figure 1. AFM anodization of Silicon Surfaces with AFM.

VIII-E-3 Nanopatterning of Alkyl Monolayers Covalently Bound to Si(111) with an Atomic Force Microscope

ARA, Masato¹; GRAAF, Harald; TADA, Hirokazu
(¹GUAS)

[*Appl. Phys. Lett.* **80**, 2565 (2002)]

Alkyl monolayers covalently bound to silicon were prepared through the reaction between 1-alkene molecules and hydrogen-terminated Si. The surfaces were anodized in nanometer scale with a contact-mode atomic force microscope (AFM) by applying positive bias voltage to the surface with respect to a conducting cantilever under ambient conditions. Following the anodization, patterned areas were selectively modified by chemical etching and coating with different molecules. The alkyl monolayers showed high resistance against chemical etching and protected Si surfaces from oxidation. AFM lithography of monolayers on Si was found to be useful for nanofabrication of organic/-inorganic interfaces based on the Si–C covalent bond.

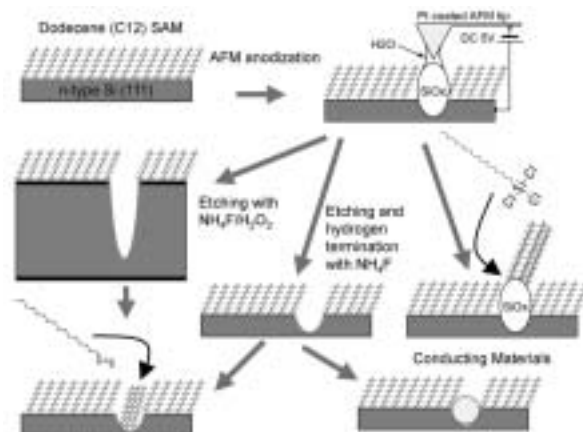


Figure 1. Nanopatterning of Silicon Surfaces with AFM.

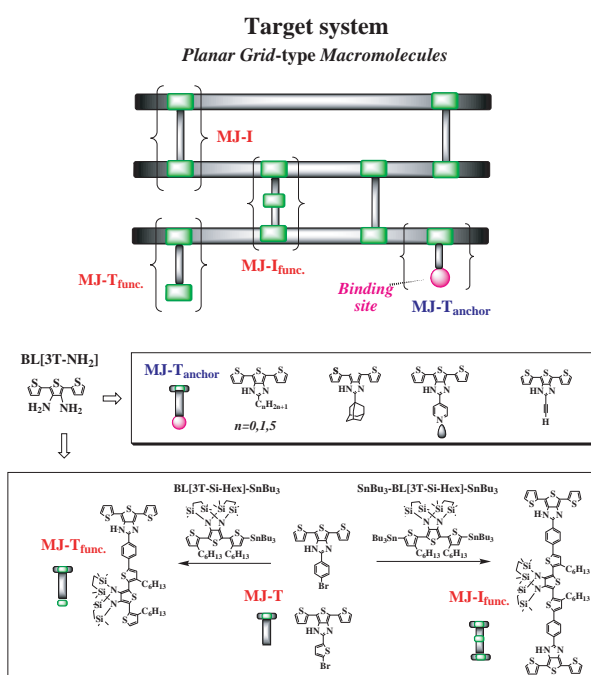
VIII-F Development of Precisely-Defined Macromolecules and their Organization on Substrate Surfaces for Molecular-Scale Electronics Circuits

The concept of molecular-scale electronics is now realized for individual components such as wire, diode, switch, and memory cell, but the fabrication of complete molecular-scale circuits remains challenging because of the difficulty of connecting molecular modules to one another. Molecular monolithic technology, which integrates the wiring, transistors and the required passive elements on a single macromolecule, has been proposed as a promising solution to this problem. In this project we have been trying to establish both the architecture of this novel class of macromolecules and the protocols for their purposive organization on metal/semiconductor substrate surfaces.

VIII-F-1 Design and Synthesis of Molecular Junction and Anchor Modules for Multi-Function Integrated Macromolecules

TANAKA, Shoji; YOKOYAMA, Takashi¹
(¹NIMS)

The design of “planar and multi-function integrated” π -conjugated macromolecules has been a subject of intensive research in the field of molecular electronics, because of their potential applications as basic components for future IT hardware such as ultra-dense molecular-scale quantum computers. In order to establish the architecture for this class of tailor-made macromolecules, we have developed various types of molecular building blocks and characterized them on substrate surfaces based on the high-resolution STM experiments combined with their bulk-level properties. Here we describe the synthesis of i) “molecule-anchor modules” for setting the molecular systems on metal/semiconductor substrate, and ii) “molecule-junction modules” for constructing planar grid-type molecular frameworks. Scheme 1 shows the synthetic pathways to these modules. Purification of these molecules was achieved by gel permeation chromatography. The purity of the obtained compounds was clearly revealed by MALDI-TOF mass spectroscopy using dithranol as matrix.



Scheme 1.

VIII-G Development of Novel Heterocyclic Compounds and their Molecular Assemblies for Advanced Materials

Heterocycles containing sulfur and/or nitrogen atoms are useful as components of functional materials since heteroatoms in their rings are helpful to stabilize ions or ion-radical species, and extended π -conjugation decreases Coulombic repulsion. In addition intermolecular interactions caused by heteroatom contacts can be expected to form novel molecular assemblies. In this project new electron acceptors, donors, and donor-acceptor compounds based on heterocycles such as 1,2,5-thiadiazole and 1,3-dithiole were synthesized and their properties including those of the charge-transfer complexes or ion-radical salts were investigated. Unique crystal structures were constructed by using weak intermolecular interactions such as hydrogen bonding or heteroatom contacts.

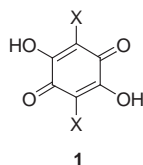
VIII-G-1 Crystal Engineering Using Anilic Acids and Dipyridyl Compounds through a New Supramolecular Synthron

ZAMAN, Md. Badruz¹; TOMURA, Masaaki; YAMASHITA, Yoshiro²
(¹IMS and Steacie Inst. Mol. Sci.; ²IMS and Tokyo Inst.

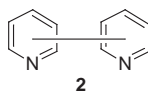
Tech.)

[*J. Org. Chem.* **66**, 5987 (2001)]

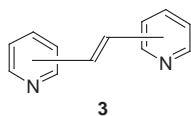
The anilic acids, 2,5-dihydroxy-1,4-benzoquinone **1a**, 2,5-dibromo-3,6-dihydroxy-1,4-benzoquinone (bromanilic acid; **1b**), 2,5-dichloro-3,6-dihydroxy-1,4-benzoquinone (chloranilic acid; **1c**), and 2,5-dicyano-3,6-dihydroxy-1,4-benzoquinone (cyananilic acid; **1d**), were cocrystallized with rigid organic ligands containing two pyridine rings, 2,4-bipyridine **2a**, 4,4'-bipyridine **2b**, 1,2-bis(2-pyridyl)ethylene **3a**, 1,2-bis(4-pyridyl)ethylene **3b**, 2,2'-dipyridylacetylene **4a**, 3,3'-dipyridylacetylene **4b**, and 4,4'-dipyridylacetylene **4c**. Fourteen complexes **5–18** were obtained as single crystals, and their crystal structures were successfully determined by X-ray analysis. All complexes except those with **2a** are 1 : 1 and are composed of an infinite linear or zigzag tape structure, the formation of which is ascribed to intermolecular O–H...N, N⁺–H...O, or N⁺–H...O[–] hydrogen bonds or a combination of these between the anilic acids and the dipyrindyl compounds. In the complexes **5** and **6**, no infinite tape structure is observed although the molecular units connected by a similar hydrogen-bonding pattern are formed. For the 1 : 1 complexes, we have found two types of stacking arrangements, segregated stacks (**7**, **9**, **12–15**, **18**) and alternated ones (**8**, **10**, **11**, **16**, **17**). In the complexes of **1c** with the series of dipyrindylacetylenes **4** (**14**, **15**, **17**), the neutral, dication, and monocation states are formed depending on the nitrogen positions, which can be attributed to the different basicity of the pyridyl groups.



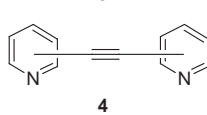
- 1a**: X = H
1b: X = Br
1c: X = Cl
1d: X = CN



- 2a**: 2,4-bipyridine
2b: 4,4'-bipyridine



- 3a**: 1,2-bis(2-pyridyl)ethylene
3b: 1,2-bis(4-pyridyl)ethylene



- 4a**: 2,2'-dipyridylacetylene
4b: 3,3'-dipyridylacetylene
4c: 4,4'-dipyridylacetylene

- 5**: complex between **1b** and **2a** **12**: complex between **1a** and **4c**
6: complex between **1c** and **2a** **13**: complex between **1b** and **4a**
7: complex between **1a** and **2b** **14**: complex between **1c** and **4a**
8: complex between **1c** and **2b** **15**: complex between **1c** and **4b**
9: complex between **1c** and **3a** **16**: complex between **1b** and **4c**
10: complex between **1b** and **3b** **17**: complex between **1c** and **4c**
11: complex between **1c** and **3b** **18**: complex between **1d** and **4c**

VIII-G-2 Bis(tetra-*n*-butylammonium) Bis(2-dicyanomethylene-4,5-dimercapto-1,3-dithiole)nickel(II)

TOMURA, Masaaki; YAMASHITA, Yoshiro¹(¹IMS and Tokyo Inst. Tech.)[*Acta Crystallogr., Sect. E* **58**, m133 (2002)]

We have carried out the X-ray crystallographic analysis of the title dithiolato-nickel complex derived from 2-dicyanomethylene-4,5-dimercapto-1,3-dithiole (dcndmdt) ligand.¹ This ligand in the nickel complex has peripheral heteroatoms and extended π -conjugated systems. In the nickel complex, [Ni(dcndmdt)₂](*n*-Bu₄N)₂, the centrosymmetric dianion is flat. The nickel atom has square-planar coordination, with Ni–S bond lengths of 2.1836(16) and 2.1940(18) Å.

Reference

- 1) M. Tomura and Y. Yamashita, *J. Mater. Chem.* **5**, 1753 (1995).

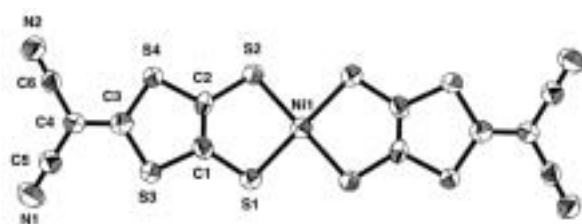


Figure 1. Molecular structure of the dianion in [Ni(dcndmdt)₂](*n*-Bu₄N)₂.

VIII-G-3 ¹H NMR Analysis and Crystal Structures of 1,1',3,3'-Tetramethyl-2,2'-bi-1*H*-Imidazolium Bis(tetraphenylborate): Ion-Associative Interactions Containing Ketone, Aldehyde, and Nitrile

ONO, Katsuhiko¹; SAITO, Katsuhiko¹; UCHIUMI, Hideki¹; TOMURA, Masaaki
 (¹Nagoya Inst. Tech.)

[*Chem. Lett.* 622 (2002)]

According to ¹H NMR analysis of 1,1',3,3'-tetramethyl-2,2'-bi-1*H*-imidazolium bis(tetraphenylborate) **1** in acetone and acetonitrile, high magnetic field shifts of the chemical shifts were observed. The facts are ascribable to ion association between the biimidazolium dication and BPh₄ anions. The crystals of **1** included some kinds of ketone, aldehyde, and nitrile as guest molecules to afford unique molecular aggregations. The biimidazolium dication is surrounded by four BPh₄ anions and is in a specific cyclic environment arising from eight phenyl groups, as shown in Figure 1. The molecular arrangements of the biimidazolium dication in the crystals can be controlled by the guest molecules.

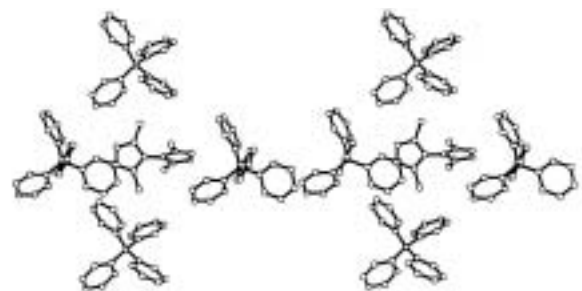


Figure 1. Stereo view of the packing mode of **1**-cyclohexanone.

VIII-G-4 4,7-Diiodo-2,1,3-Benzothiadiazole and 7,7'-Diiodo-4,4'-bis(2,1,3-benzothiadiazole)

TOMURA, Masaaki; AKHTARUZZAMAN, Md.¹; SUZUKI, Kazuharu²; YAMASHITA, Yoshiro³
(¹GUAS; ²IMS and Inst. Res. Innov.; ³IMS and Tokyo Inst. Tech.)

[*Acta Crystallogr., Sect. C: Cryst. Struct. Commun.* **58**, o373 (2002)]

The title compounds, 4,7-diiodo-2,1,3-benzothiadiazole **1** and 7,7'-diiodo-4,4'-bis(2,1,3-benzothiadiazole) **2** crystallize in the $P2_1/a$ and the noncentrosymmetric $Fdd2$ space group, respectively. In the crystal structures of **1**, a large number of short S...N and I...I contacts, and a planar I_4 square cluster are observed, as shown in Figure 1. The angle between the planes for the two 2,1,3-benzothiadiazole rings of **2** is $48.4(1)^\circ$, and short and linear N...I contacts [$3.333(8)$ Å] exist in the crystal of **2**.

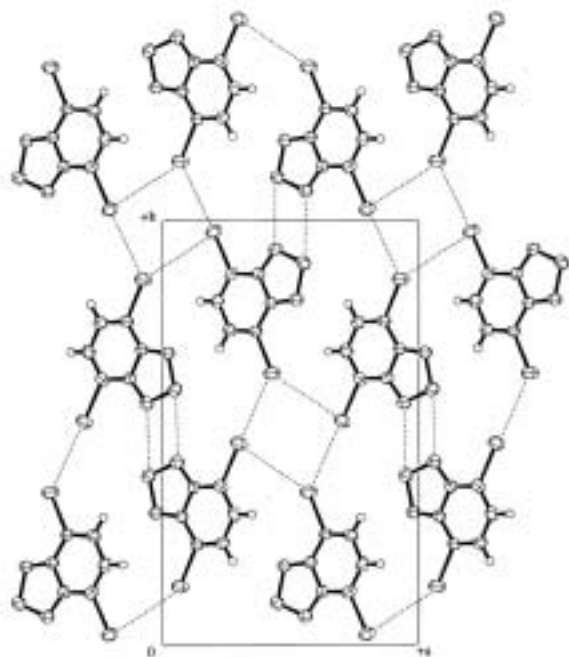


Figure 1. Packing diagram of **1** viewed along the c axis. Dotted lines show the short S...N and I...I contacts.

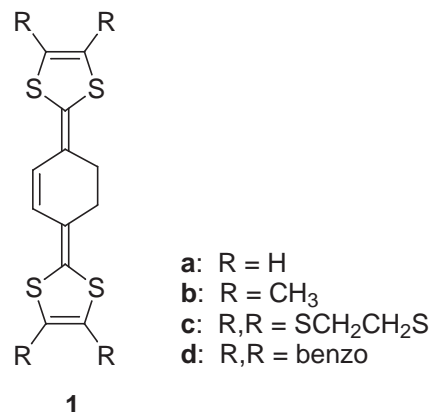
VIII-G-5 Synthesis and Properties of π -Extended TTF Analogues and Their Cation Radical and Dication Salts

YAMASHITA, Yoshiro¹; TOMURA, Masaaki; URUICHI, Mikio; YAKUSHI, Kyuya
(¹IMS and Tokyo Inst. Tech.)

[*Mol. Cryst. Liq. Cryst.* **376**, 19 (2002)]

New bis(1,3-dithole) electron donor **1** containing a cyclohexene unit were prepared using a Wittig-Honer reaction and a cycloreversion reaction. The tetramethyl

derivative afforded the highly conductive cation radical salts as single crystal whose unusual crystal structures were revealed by X-ray crystallographic analysis.



VIII-G-6 Synthesis and Structure of Bi- and Terthiophene Derivatives Having 4-Pyridylethynyl Substituents

TOMURA, Masaaki; YAMASHITA, Yoshiro¹
(¹IMS and Tokyo Inst. Tech.)

Conjugated organic oligomers are gaining increasing attention as new and promising materials in the field of molecular electronics. We have synthesized the title compounds, which are able to coordinate with metals and perform intermolecular interaction *via* hydrogen bonding, using the Sonogashira reaction. The X-ray crystallographic analyses of them revealed that the centrosymmetric bithiophene derivative has the *anti* conformation, whereas the crystallographically independent terthiophene derivative has *anti-cis* conformation. All thiophene and pyridine rings in the two derivatives are almost coplanar.

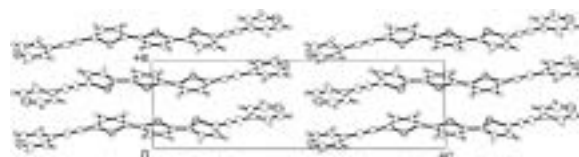


Figure 1. Molecular packing of 5,5''-bis[(4-pyridyl)ethynyl]-2,2':5',2''-terthiophene viewed along the b axis.

VIII-H Designing Artificial Photosynthesis at Molecular Dimensions

Photosynthesis is one of the finest piece of molecular machinery that Nature has ever created. Its ultrafast electron transfer and following well-organized sequence of chemical transformation have been, and will continue to be, challenging goals for molecular scientists. We are trying to mimic the function of photosynthesis by assembling molecular units that perform individual physical/chemical action. The molecular units include porphyrins, redox active organic molecules, and transition metal complexes. Our ultimate goal is to design artificial molecular systems that effect multiple chemical reactions triggered by light on the basis of molecular rationale.

VIII-H-1 Photoinduced Oxidation of Alcohols Catalyzed by Porphyrins and TEMPO

ITO, Hajime; NAGATA, Toshi

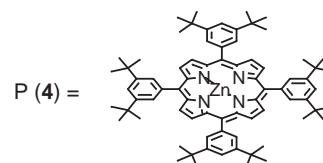
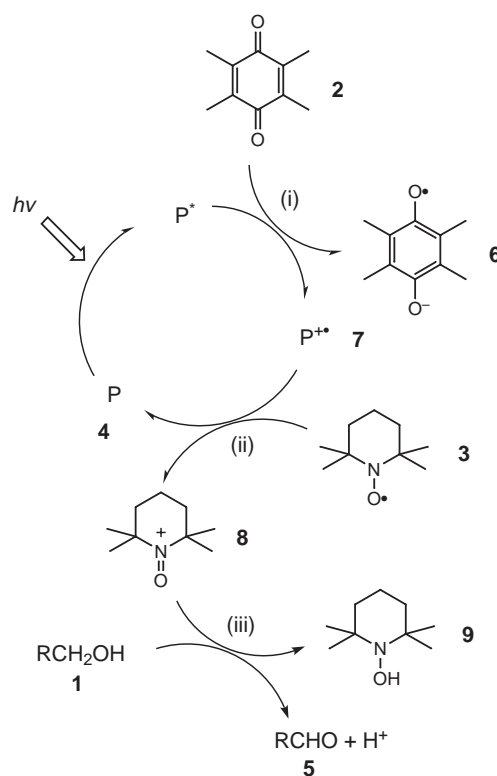
Photoinduced electron transfers involving porphyrins are widely studied, but utilizing the high-energy radical ion pairs for driving chemical reactions remains to be a great challenge. Herein we report the TEMPO-mediated oxidation of alcohols catalyzed by porphyrins under irradiation with visible light. Although there have been many reports on TEMPO-mediated oxidation of alcohols, our system is the first to utilize photoinduced electron transfer including porphyrins.

When a solution of benzyl alcohol (**1**, 0.1 mmol), duroquinone (**2**, 0.1 mmol), TEMPO (**3**, 2,2,6,6-tetramethylpiperidine N-oxide, 0.1 mmol), diisopropylethylamine (0.2 mmol) and 5,10,15,20-tetrakis(3,5-*di-t*-butylphenyl)porphinatozinc(II) (**4**, 0.001 mmol) in THF/DMF (1/1, 0.5 ml) was irradiated with visible light ($\lambda > 500$ nm, halogen lamp with a Toshiba Y-52 filter) for 10 hours, benzaldehyde (**5**) was formed in 23% yield. On addition of tetrabutylammonium perchlorate (0.1 mmol), the yield was improved to 42%. When either TEMPO, duroquinone, diisopropylethylamine or porphyrin was omitted, or in the absence of light, no benzaldehyde was detected.

As the reaction proceeded, 2,2,6,6-tetramethyl-N-hydroxypiperidine (TEMPO-H, **9**) was detected together with benzaldehyde, indicating that the oxidant was TEMPO rather than duroquinone. It is noteworthy, however, that in the absence of duroquinone the reaction did not proceed. The role of duroquinone is rationally understood by assuming photoinduced electron transfer from the porphyrin to the quinone. The tentative reaction mechanism is shown in Scheme 1; (i) the photoexcited porphyrin transfers an electron to the quinone, (ii) the cation radical of the porphyrin (**7**) oxidizes TEMPO to give the oxoammonium intermediate (**8**), (iii) the oxoammonium cation oxidizes the alcohol (**1**) with the aid of the base. The quinone anion radical (**6**) should be oxidized to regenerate the quinone either (iv) by the porphyrin cation radical, (v) by the oxoammonium cation, or (vi) by TEMPO. As the paths (iv) and (v) are non-productive, they result in the lower efficiency. Indeed, the reaction was too slow to be synthetically useful, so that we looked into the way to improve the reaction efficiency.

A moderate success was achieved by changing the electron acceptor. When 2,6-*di-t*-butyl-1,4-benzoquinone was used in place of duroquinone, benzalde-

hyde was obtained in 86% yield by use of 0.2 equivalents of TEMPO instead of the stoichiometric amount (solvent = base = pyridine, 27 hours irradiation). In this system, 2,5-*di-t*-butyl-1,4-hydroquinone accumulated instead of TEMPO-H. We assume that direct oxidation of the quinone anion radical was suppressed by the introduction of the bulky *t*-butyl groups.



Scheme 1.

VIII-I Development of New Metal Complexes as Redox Catalysts

Redox catalysis is an important field of chemistry which translates a flow of electron into chemical transformation. It is also one of the requisites for artificial photosynthesis. This project of ours aims at developing new metal complexes that perform redox catalysis at low overpotential. We have been focusing our attention to developing terdentate ligands with strong donor character, and have found that introducing a pyrrole ligand in place of pyridine leads to useful ligands.

VIII-I-1 Syntheses of a 6-(2-Pyrrolyl)-2,2'-Bipyridine Derivative and Its Ruthenium Complex

NAGATA, Toshi; TANAKA, Koji

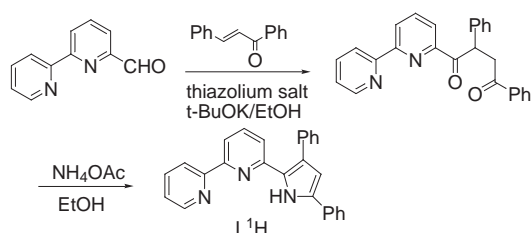
[*Bull. Chem. Soc. Jpn.* in press.]

Metal complexes of pyrroles are gathering interest as an activator of the pyrrole ring, an intermediate for synthesizing pyrrole derivatives, and as a component of conducting polymers. Herein we report the syntheses of 6-(3,5-diphenyl-2-pyrrolyl)-2,2'-bipyridine (L^1H) and its ruthenium complex $[Ru(L^1)_2]$. The compound L^1H is the first example of the "ter-aryl" ligand that has one pyrrole and two pyridine rings in this order, and it will be a useful substitute for 2,2':6',2''-terpyridine (terpy) when more electron-donating character is desirable.

The synthesis of L^1H is shown in Scheme 1. The Stetter condensation of 2,2'-bipyridine-6-carbaldehyde with chalcone was utilized, followed by ring closure of the 1,4-diketone with an ammonium salt (67% yield). By use of pyridine-2,6-dicarbaldehyde as a starting material, the compound L^2H_2 , 2,6-bis(3,5-diphenyl-2-pyrrolyl)pyridine, was also obtained (69% yield).

The ORTEP drawing of the complex $[Ru(L^1)_2]$ is shown in Figure 1. The coordination geometry around the Ru(II) center is similar to that of $[Ru(terpy)_2]X_2$, however the six pyridine/pyrrole rings are not exactly coplanar.

The cyclic voltammograms of $[Ru(L^1)_2]$ and $[Ru(terpy)_2](ClO_4)_2$ are shown in Figure 2. The Ru(III)/Ru(II) couple appeared at -0.29 V (*versus* ferrocene/ferrocenium couple) in $[Ru(L^1)_2]$, which was 1.10 V more negative than in $[Ru(terpy)_2](ClO_4)_2$, consistent with the strong donor character of the L^1 ligand. The first reduction wave (reduction of the ligand) was also negatively shifted by 0.51 V. At higher potential range ($+0.5$ – 0.7 V), $[Ru(L^1)_2]$ showed irreversible waves suggesting the oxidative degradation of the complex. Apparently the oxidation of the pyrrole rings led to the degradation of the ligand and/or the decomplexation of the metal ion.



Scheme 1. Synthesis of the ligand L^1H .

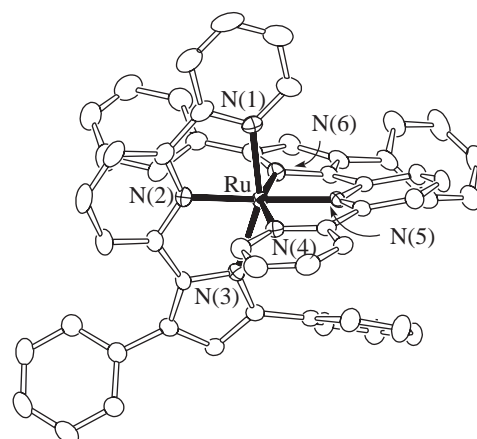


Figure 1. ORTEP view (50% probability ellipsoids) of the complex $[Ru(L^1)_2]$.

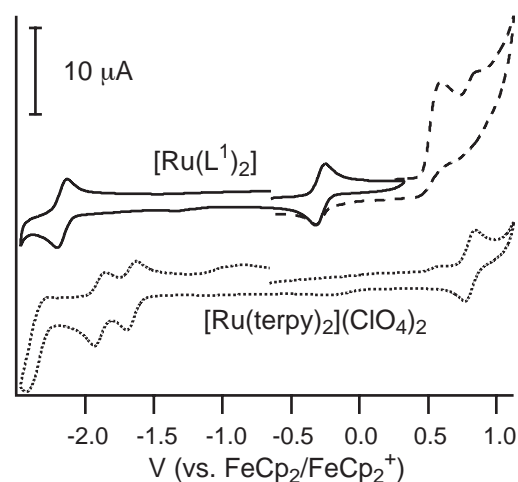


Figure 2. The cyclic voltammograms of $[Ru(L^1)_2]$ and $[Ru(terpy)_2](ClO_4)_2$.

VIII-J Electronic Properties of Monolayer-Protected Metal Clusters

Monolayer-protected metal clusters or nanoparticles have received much attention recently because their electronic and optical properties can be tuned by their sizes and shapes. The novel electronic properties of the clusters as well as their tunability are important from the viewpoint of future application as optoelectronic nanodevices. Our interests are focused on the following topics on the thiol-derivatized metal clusters and nanoparticles: (1) preparation and characterization of small clusters with core diameters of ~ 1 nm range (~ 40 atoms/cluster) which may exhibit molecular-like electronic and charging properties, (2) determination of structural dimensions (core diameters and monolayer thickness) of metal nanoparticles, and (3) development of size-selection method for the clusters and nanoparticles. Our goal is to reveal the evolution of electronic structures of the metal clusters as a function of the cluster size.

VIII-J-1 Development of Mass Spectrometer for Clusters

NEGISHI, Yuichi; TSUKUDA, Tatsuya

Mass spectrometry provides detailed informations on the chemical compositions of the metal clusters. We have constructed a time-of-flight (TOF) mass spectrometer which accommodates three types of ion sources: (1) a matrix-associated laser desorption ionization (MALDI) source for clusters obtained as solid, (2) an electrospray ionization source for clusters dispersed in aqueous phase, and (3) an electron-impact ionization source for molecular clusters. Only a brief description on the MALDI/TOF apparatus, which has been developed recently, is presented here. The specimens for mass analysis are prepared by depositing an aliquot (~ 1–5 μL) of the mix solutions of cluster samples and matrix onto a surface of a target made of stainless steel. After the solvent is evaporated at ambient atmosphere, the target is fed into the mass spectrometer through a load-lock chamber and attached to one of acceleration grids. The sample is irradiated with the third harmonic (355 nm) of a Nd:YAG laser operated at 10 Hz. The laser fluence is adjusted typically in the range of 10–40 $\mu\text{J}/\text{mm}^2/\text{pulse}$. The cluster ions thus formed are accelerated by applying a pulsed high voltage (15–20 kV) to the electrode plates. The ion beams are focused and stirred by ion optics and then detected by a MCP detector located at the end of the flight path of 1.17 m. Mass spectra of the ions of either polarity can be recorded by simply changing the polarities of the power supplies.

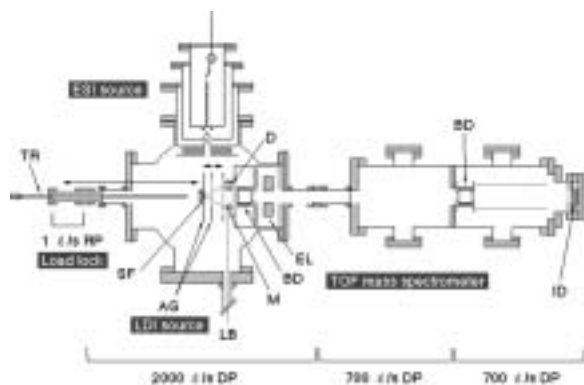


Figure 1. Schematic diagram of the apparatus: TR: transfer rod, SF: sample folder, AG: acceleration grid, LB: laser beam, M: mirror, D: damper, BD, beam defectors, EL: einzel lens, ID: ion detector. Details of the ESI source are not described here. The EI source installed perpendicularly to the diagram is not shown.

VIII-J-2 Formation of $\text{Pd}_n(\text{SR})_m$ Clusters ($n < 60$) in the Reactions of PdCl_2 and RSH ($\text{R} = n\text{-C}_{18}\text{H}_{37}$, $n\text{-C}_{12}\text{H}_{25}$)

NEGISHI, Yuichi; MURAYAMA, Haruno; TSUKUDA, Tatsuya

[*Chem. Phys. Lett.* **366**, 561 (2002)]

Mass spectroscopic analysis revealed that Pd clusters passivated by thiolates as well as the stoichiometric thiolate complexes $\text{Pd}_n(\text{SR})_{2n}$ ($n = 5, 6$) are formed in the reactions between palladium chloride and n -alkane-thiols (RSH: $\text{R} = n\text{-C}_{18}\text{H}_{37}$, $n\text{-C}_{12}\text{H}_{25}$) in toluene. The Pd clusters thus formed are formulated as $\text{Pd}_n(\text{SR})_m$ with $m \sim 0.6n$ and the cluster size are distributed in the range of $5 \leq n \leq 60$, being consistent with core diameters of ~ 1 nm determined by TEM observations. A gap of ~ 2 eV was observed in the optical transition of the $\text{Pd}_n(\text{SR})_m$ clusters showing the emergence of non-metallic properties as a result of the size reduction.

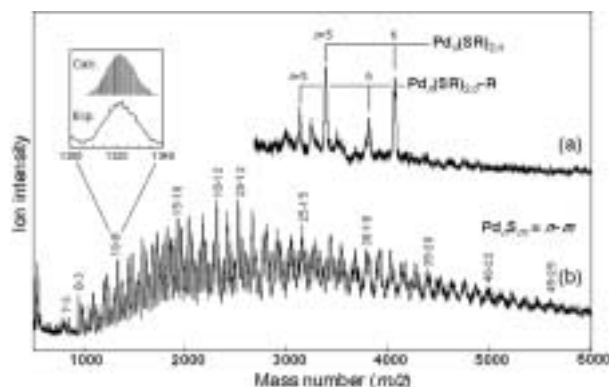


Figure 1. Typical representations of MALDI mass spectra of the mixtures of $\text{PdCl}_2/n\text{-C}_{18}\text{H}_{37}\text{SH}$ which are diluted with anthracene to (a) ~ 1 and (b) ~ 20 mol%.

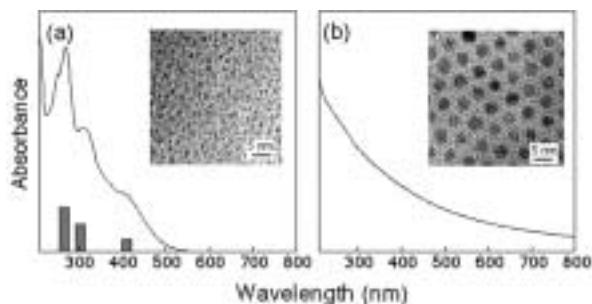


Figure 2. Optical spectra of hexane solutions of (a) PdCl₂/*n*-C₁₈H₃₇SH mixture and (b) Pd:SC₁₈H₃₇ nanoparticles. The solid bars in panel (a) represent the absorbance of the Pd_{*n*}(SC₁₈H₃₇)_{2*n*} complexes (*n* = 5 and 6).

VIII-J-3 Size-Selective Preparation of Water-Soluble Gold Clusters

NEGISHI, Yuichi; TSUKUDA, Tatsuya

Colloidal solution of gold clusters was formed upon mixing AuCl or AuCl₄⁻ and *meso*-dimercaptosuccinic acid (DMSA: HO₂CCH(SH)CH(SH)CO₂H) in water. The size distributions of the gold clusters can be controlled by simply changing the mixing ratios of the gold salts and DMSA as revealed by optical spectroscopy and TEM observations. Figure 1 shows the uv-vis spectra of the colloidal solutions prepared with different mixing ratios between AuCl and DMSA. With increase in the ratios of DMSA, the surface plasmon band at ~530 nm disappears and the onset of the optical transition shifts toward shorter wavelength, implying the reduction of the cluster sizes. The TEM measurements confirm this trend: the average sizes of the Au cores are 3.1 ± 0.7 and 1.8 ± 0.6 for the mixing ratios [DMSA]/[AuCl] of 1 and 2, respectively (Figure 2). These findings indicate the DMSA molecules act both as reducing agents against the Au(I) or Au(III) ions and stabilizing ligands for the resulting Au(0) clusters. Optimization of preparation conditions as well as purification of the clusters by polyacrylamide gel electrophoresis (PAGE) and gel permeation chromatography (GPC) is now under way in our laboratory.

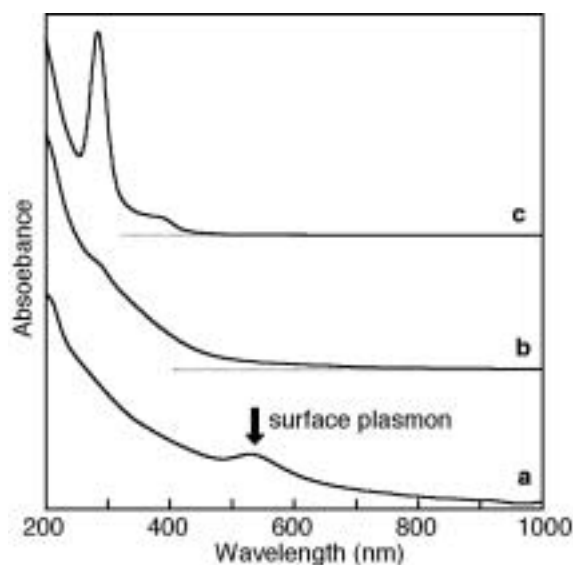


Figure 1. Optical spectra of colloidal solutions of gold clusters prepared with the mixing ratios [DMSA]/[AuCl] of (a) 0.1, (b) 0.2, and (c) 0.4.

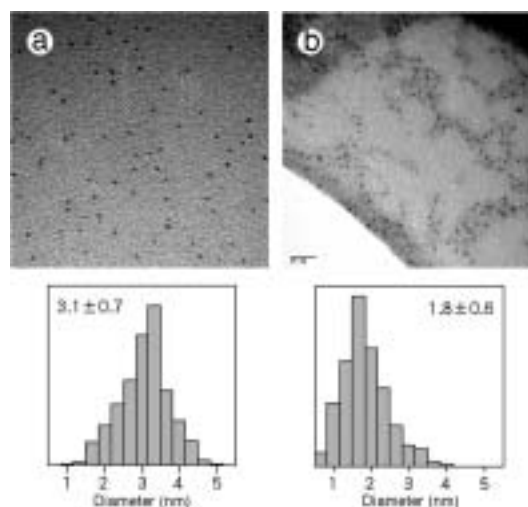


Figure 2. TEM images and size distributions of gold clusters obtained with the mixing ratios [DMSA]/[AuCl] of (a) 1 and (b) 2.

VIII-J-4 Characterization and Purification of Pd:SR Nanoparticles by Gel Permeation Chromatography

MURAYAMA, Haruno; TSUKUDA, Tatsuya

Gel permeation chromatography (GPC) and transmission electron microscopy (TEM) have been used to characterize the structures of Pd:SR (R = *n*-C₁₈H₃₇, C₁₆H₃₃, C₁₄H₂₉, C₁₂H₂₅, C₁₀H₂₁, C₆H₁₃) nanoparticles. The Pd:SR nanoparticles are prepared by ligand exchange of PVP-protected Pd nanoparticles.¹⁾ The difference between the average diameter (*D_c*) measured by TEM and hydrodynamic diameter (*D_h*) determined by GPC allows us to determine the thickness (*T*) of the monolayer of alkanethiolates. On the basis of these results together with the length of free alkanethiols, a structural model of the monolayers on the Pd clusters has been proposed. It is also demonstrated that the Pd:SR clusters which are size selected by GPC show pronounced tendency to self-assemble into two-dimensional superlattices (Figure 1). Further purification of the clusters by the GPC in a recycled mode is now in progress in our group.

Reference

- 1) T. Tsukuda, N. Kimura, T. Sasaki and T. Nagata, *Trans. Matr. Res. Soc. Jpn.* **25**, 929 (2000).

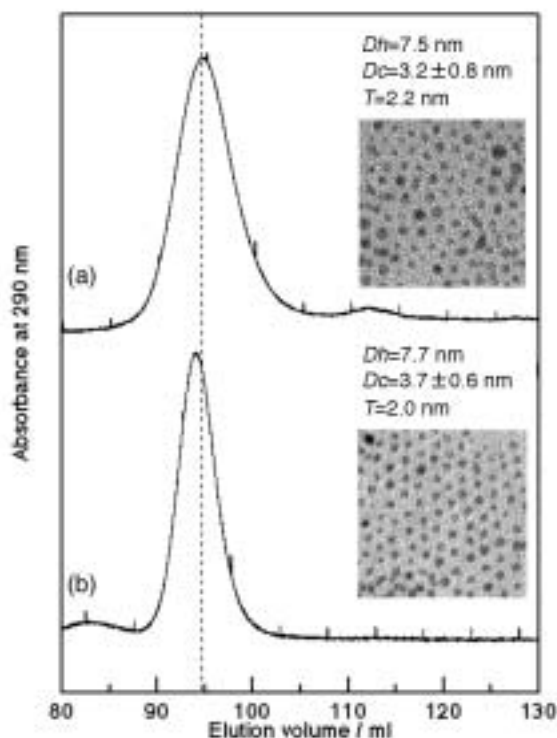


Figure 1. Chromatograms and TEM images for (a) as-prepared and (b) purified Pd:SR nanoparticles.

VIII-K Structures and Dynamics of Molecular Cluster Ions

Molecular clusters, intermediate states of matter between bulk and a molecule, provide us unique opportunities to study how the chemical and physical properties evolve with a degree of aggregation. We studied photo-induced reactions within size-selected cluster anions and evolutions of crystal structures of clusters.

VIII-K-1 Structural Evolution of Large $(\text{CO}_2)_n^-$ Clusters as Studied by Mass Spectrometry

NEGISHI, Yuichi; NAGATA, Takashi¹; TSUKUDA, Tatsuya
(¹Univ. Tokyo)

[*Chem. Phys. Lett.* **364**, 127 (2002)]

The mass distributions of $(\text{CO}_2)_n^-$ produced by electron-impact ionization of a free jet have been measured up to $n \sim 10^3$. Several intensity anomalies observed in a small size range are ascribed to the stabilities of the negative ions. In contrast, a series of humps are clearly discernible in the range of $n \geq 100$, which reflects the abundance of neutral $(\text{CO}_2)_n$. The intensity oscillations are analyzed in the context of “geometrical shell closings.” The analysis reveals that the $(\text{CO}_2)_n$ clusters with $n > \sim 80$ have truncated forms of an *fcc* crystal, most likely a cuboctahedral motif (Figure 1).

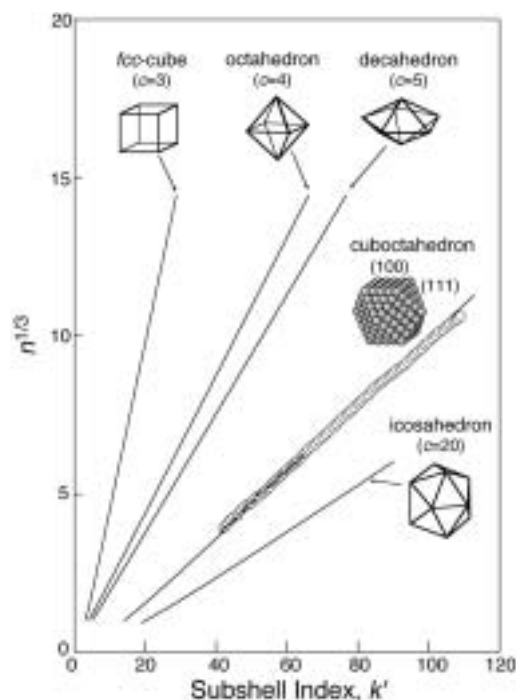


Figure 1. Plots of $n^{1/3}$ against the subshell index k' for various polyhedra. Symbols \circ and \bullet represent the experimental data for $(\text{CO}_2)_n^-$ and $(\text{CO}_2)_n^+$, respectively. Both plots are explicable in terms of cuboctahedra (CO). The spheres in the CO motif represent the CO_2 constituent molecules.

VIII-K-2 Photochemistry of $(\text{NO})_n^-$ as Studied by Photofragment Mass Spectrometry

TSUKUDA, Tatsuya; ZHU, Lei¹; SAEKI, Morihisa; NAGATA, Takashi²

(¹Data Storage Inst.; ²Univ. Tokyo)

[*Int. J. Mass Specrom.* **220**, 137 (2002)]

Photofragmentation of $(\text{NO})_n^-$ ($3 \leq n \leq 21$) in the energy range 2.7–3.6 eV (350–460 nm) results in the production of $(\text{NO})_m^-$ with $m \geq 2$ and $\text{NO}_2^-(\text{NO})_m$ with $0 \leq m \leq 2$. The photofragment yield spectra obtained for $n = 3$ –7 display a broad and structureless band profile with successive blue-shift with increase in the cluster size, indicating that N_3O_3^- (reference 1) behaves as a chromophoric core in the larger $(\text{NO})_n^-$. The observed fragmentation patterns suggest that photoexcitation of the N_3O_3^- chromophore is followed by direct dissociation into $(\text{NO})_2^-$, solvent evaporation to form $(\text{NO})_m^-$, and/or intracluster reactions to produce NO_2^- .

Reference

- 1) T. Tsukuda, M. Saeki, L. Zhu and T. Nagata, *Chem. Phys. Lett.* **295**, 416 (1998).

VIII-L Rotational Echo Double Resonance (REDOR) Experiments with Overtone Adiabatic Inversion Pulses

The effect of an overtone adiabatic inversion pulse on solid-state ^{14}N spins was investigated.

VIII-L-1 The Observation of REDOR Phenomena for Solid-State ^{13}C - ^{14}N Spin Systems with the Help of Overtone Adiabatic Inversion Pulses

KUWAHARA, Daisuke

We applied overtone adiabatic inversion pulses to ^{13}C - ^{14}N spin systems in powdered *L*-alanine undergoing MAS in order to observe REDOR phenomena. The damping of ^{13}C resonance line intensities was compared with that corresponding to the REDOR experiments with normal RF pulses having a constant frequency. We tried to establish the theoretical treatment for the REDOR experiments with adiabatic inversion pulses. The computer simulations for the REDOR experiments revealed that overtone adiabatic pulses had little dependence on the offsets of rf carrier frequencies.

VIII-M Nanoscale Characterization of Heterogeneous Catalyst Surfaces

Heterogeneous catalysis occurs on a surface of a solid catalyst. Active centers for heterogeneous catalysis commonly consist of clusters of several surface atoms, and thus a long-range order of surface atoms is not normally required. Therefore, when using precious metals as catalysts, nanometer-scale superfine particles are commonly employed in order to increase its surface area and to decrease the amount of catalysts. This introduces difficulties in characterizing the catalyst surfaces and their active centers, because characterization techniques of solid surfaces at nanometer-scale are not well established. Here we mainly used scanning probe microscopes, in conjunction with other surface characterization techniques, to characterize catalytically active centers as well as the nature of catalyst-support interactions.

VIII-M-1 Determination of Extra-Framework Cation Positions and Their Occupancies on Heulandite(010) by Atomic Force Microscopy

KOMIYAMA, Masaharu; GU, Minming¹; WU, Hai-Ming²
(¹McGill Univ.; ²Res. Inst. Innovative Tech. Earth)

[*J. Phys. Chem. B* **105**, 4680 (2001)]

Atomic images of a cleaved heulandite(010) surface were obtained under an aqueous condition by atomic force microscopy (AFM). In addition to the framework oxygen atoms on the (010) plane, extra-framework cations on the surface were also imaged. An AFM imaging simulation was performed using published X-ray diffraction data to assist the assignment of the AFM-observed framework and extra-framework atoms. By comparing it with the observed AFM images, local variations of position and occupancy of individual cations were determined.

VIII-M-2 Molecular Orbital Interpretation of Thymine/Graphite NC-AFM Images

KOMIYAMA, Masaharu; UCHIHASHI, Takayuki¹; SUGAWARA, Yasuhiro^{1,2}; MORITA, Seizo²
(¹Joint Res. Center Atom Tech.; ²Osaka Univ.)

[*Surf. Interface Anal.* **29**, 53 (2001)]

Recent non-contact atomic force microscopy (nc-AFM) images of a deoxyribonucleic acid (DNA) base thymine (2,4-dioxy-5-methylpyrimidine), vacuum-deposited on a highly-oriented pyrolytic graphite (HOPG) surface, are interpreted by means of theoretical adsorption simulations, and the molecular geometry and the energetics of the adsorption system are estimated. The lowest-energy dimer configuration was found to be the one in which the respective hydrogen on number 1 nitrogen and oxygen on number 6 carbon of two thymine molecules make a hydrogen bond to each other. A surface unit cell structure was reproduced. Adsorption energy for the thymine pair on HOPG is rather small, amounting to only *ca.* 1 kcal/mol, with small variations depending on the molecular orientation with respect to the substrate surface. A possibility of having a mirrored adsorption configuration in adjacent domains is also suggested.

VIII-M-3 Partial Reduction of Si(IV) in SiO₂ Thin Film by Deposited Metal Particles—An XPS Study

KOMIYAMA, Masaharu; SHIMAGUCHI, Takemi¹
(¹Yamanashi Univ.)

[*Surf. Interface Anal.* **29**, 189 (2001)]

Metal-support interactions in the systems of dispersed metals supported on thin film silica surfaces were examined by X-ray photoelectron spectroscopy. Four metal-silica systems, Pt-, Pd-, Ag- and Au-SiO₂, all indicated the formation of partially reduced Si(IV) species by the metal deposition. The extent of the reduction varied little with the kind and the amount of deposited metal species. On the other hand, the amount of this newly formed Si(IV- δ) indicated a strong metal species dependence.

VIII-M-4 Apparent Local Structural Change Caused by Ultraviolet Light on a TiO₂ Surface Observed by Scanning Tunneling Microscopy

KOMIYAMA, Masaharu; YIN, Donghong¹
(¹Hunan Normal Univ.)

[*Jpn. J. Appl. Phys.* **40**, 4281 (2001)]

An apparent local surface structural change at nanoscale was observed by scanning tunneling microscopy on a TiO₂ surface upon irradiation with ultraviolet (UV) light. This phenomenon was reversible with UV light irradiation, and was interpreted to be due to the local accumulation of photoexcited states. This is the first real-space observation of inhomogeneous local charge distribution under UV light irradiation at nanoscale on a semiconductive photocatalyst surface, which may help identify the photocatalytic active sites and elucidate their reaction mechanisms.

VIII-M-5 Various Phases on Natural Stilbite (010) Surface Observed by Atomic Force Microscopy under Aqueous Conditions

GU, Ning¹; KOMIYAMA, Masaharu
(¹Southeast Univ.)

[*Jpn. J. Appl. Phys.* **40**, 4285 (2001)]

Various phases on a natural stilbite (010) surface were observed by atomic force microscopy (AFM) under aqueous conditions. In a wide-area observation, oriented protrusions observed on the surface differed from the “sheaflike” structure which has been found in stilbite in an aqueous NaOH solution. Narrow-area observations showed surfaces consisting of an island structure, or a structure of alternating ridges and trenches. The latter is similar to the one reported previously under ambient conditions. The atomically resolved AFM image of the stilbite confirms that its surface is in good agreement with the known crystallographic parameters of the bulk-terminated (010) surface. Defects such as dislocations and grain boundaries at the atomic level were also observed.

VIII-N Studies of Electronic Structure of Organic Thin Films and Organic/Inorganic Interfaces by Electron Spectroscopies

Electronic structures of organic film surface and organic/inorganic interface are expected to play an important role in organic-device properties. We investigated surface structures and energy alignments to clarify their electronic structures using surface sensitive spectroscopy such as photoelectron spectroscopy combined with synchrotron radiation and metastable atom electron spectroscopy.

VIII-N-1 Low Energy Electron Diffraction of the System In-[perylene-3,4,9,10-tetracarboxylic Dianhydride] on MoS₂

AZUMA, Yasushi¹; IWASAKI, Kazuaki²;
KURIHARA, Tsutomu²; OKUDAIRA K., Koji;
HARADA, Yoshiya³; UENO, Nobuo¹
(¹IMS and Chiba Univ.; ²Chiba Univ.; ³Seitoku Univ.)

[*J. Appl. Phys.* **91**, 5024 (2002)]

The system In-perylene-3,4,9,10-tetracarboxylic dianhydride ~PTCDA on MoS₂, prepared by the sequential evaporation of PTCDA and In on a cleaved MoS₂ surface, was studied by low energy electron diffraction. The result indicates that reaction products form an ordered structure on the MoS₂ surface. From the analysis of the diffraction pattern, the presence of six symmetry-equivalent domains of an oblique unit cell of In-PTCDA species results with the dimensions of 9.5 Å, 16.3 Å, and an enclosed angle of 80.2°. In addition, splitting in two domains by a mirror plane exists with the rotation angle $R5610.8^\circ$ with respect to each of the three equivalent surface crystal axes of the MoS₂ substrate. The new structure is explained by assuming that four In atoms are chemically bonded to the four carbonyl groups of the PTCDA molecules. Furthermore, it is concluded that the In₄PTCDA species become tilted after a chemical reaction between the PTCDA molecules and the In atoms, which is in agreement with results previously obtained by angle-resolved ultraviolet photoemission experiments.

VIII-N-2 Electronic Structure and Molecular Orientation at Thin Film Surfaces of Pendant-Group Polymers Studied by Outermost Surface Spectroscopy Using Metastable Atoms

OKUDAIRA K., Koji; KERA, Satoshi²;
SETOYAMA, Hiroyuki²; MORIKAWA, Eiji³;
UENO, Nobuo¹
(¹IMS and Chiba Univ.; ²Chiba Univ.; ³Louisiana State Univ.)

[*J. Electron Spectrosc. Relat. Phenom.* **121**, 225(2001)]

Metastable-atom electron spectroscopy (MAES) and ultraviolet photoelectron spectroscopy (UPS) were used to study the outermost surface of thin films of pendant group polymers: polystyrene (PSt), poly(2-vinylnaphthalene), and poly(9-vinylcarbazole). MAES is selectively sensitive to the outermost surface, and indicated that the surfaces of the polymer films were very clean,

even though they were prepared by spin-casting in a room atmosphere. In Figure 1 observed MAES and UPS of PSt are shown. By comparison with gas-phase spectra and molecular orbital calculations of model molecules with pendant groups, it was confirmed that the principal constituent at the outermost surface of these polymer films is the pendant groups. Furthermore, it was observed that the intensity for σ (C–H) states of the pendant group is stronger in MAES spectra than in UPS spectra, indicating many pendant groups are inclined at large tilt angles.

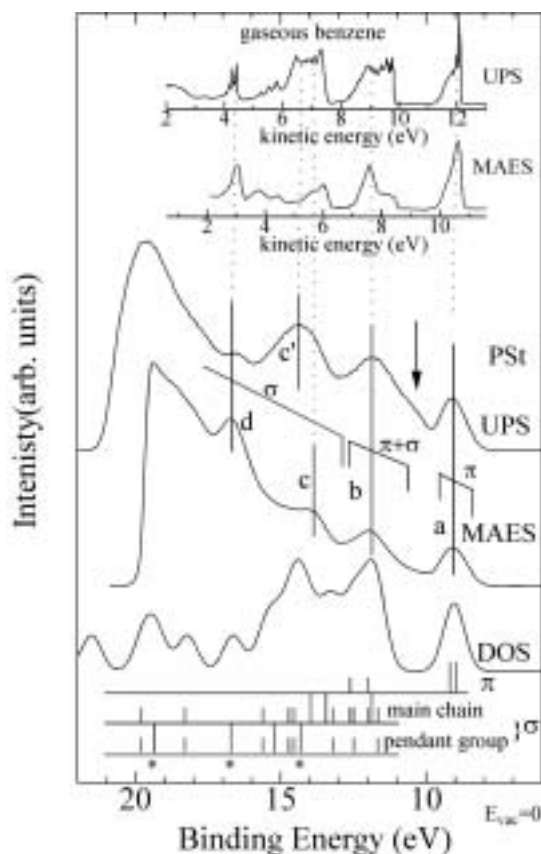


Figure 1. MAES and UPS of polystyrene (PSt) thin film. The vertical bars show the molecular orbital energies calculated by *ab initio* MO calculation (6-31G with diffuse function) for the model compound of PSt. The energy levels for the molecular orbital consisted of π orbital at pendant group and σ orbital at polymer chain are represented by the vertical bars marked by asterisk(*). The density of states (DOS) was obtained by broadening with gaussian function (width = 0.8 eV). The calculated binding energy scale was contracted by 1.35 and shifted to fit with the experimental results. The inset shows the MAES and UPS of gaseous benzene.

VIII-N-3 Photodegradation of Poly(tetrafluoroethylene) and Poly(vinylidene fluoride) Thin Films by Inner Shell Excitation

OKUDAIRA K., Koji; YAMANE, Hiroyuki²; ITO, Kazuhiko²; IMAMURA, Motoyasu³; HASEGAWA, Shinji; UENO, Nobuo¹
(¹IMS and Chiba Univ.; ²Chiba Univ.; ³AIST)

[*Surf. Rev. Lett.* **9**, 335 (2002)]

Ion time-of-flight (TOF) mass spectra of poly(tetrafluoroethylene) (PTFE) and poly(vinylidene fluoride) (PVDF) thin films near fluorine and carbon *K*-edges were observed. For PTFE thin films peaks corresponding to F^+ , CF^+ , and CF_3^+ appeared, while for PVDF F^+ and H^+ were mainly observed. They indicate that for PTFE the polymer chain (C–C bonds) as well as C–F bonds are broken by irradiation of photons near fluorine and carbon *K*-edges, while for PVDF the bond scission occurs mainly at the C–F and C–H bond. Partial ion yields (PIY) of these ions for PTFE and PVDF thin films show strong photon energy dependencies near fluorine (Figure 1) and carbon *K*-edges. The excitation from fluorine $1s$ to $\sigma(C-F)^*$ is specially efficient for F^+ ion production for both PTFE and PVDF.

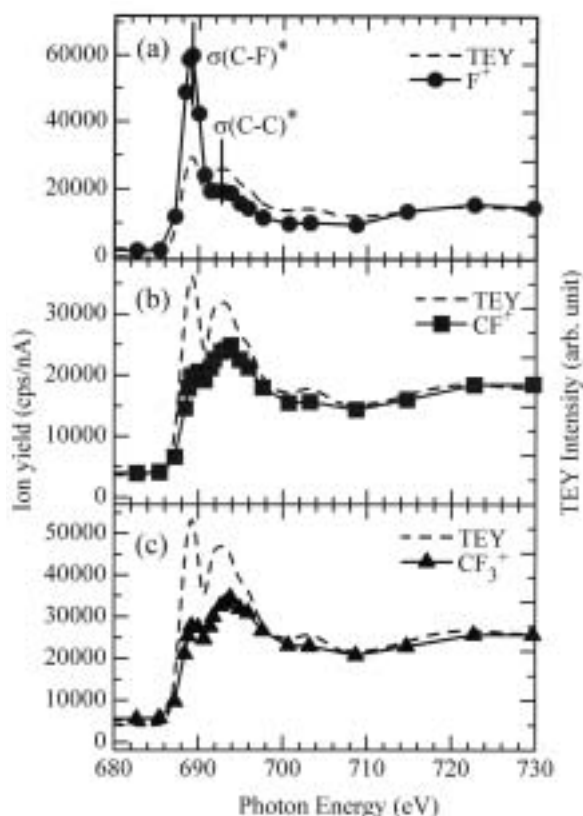


Figure 1. PIY spectra of (a) F^+ , (b) CF^+ and (c) CF_3^+ for PTFE thin film near the fluorine *K* absorption edge. TEY spectra (broken curve) are also shown for comparison. TEY spectra are renormalized at $h\nu = 682.5$ eV and at $h\nu = 730$ eV to fit PIY intensities.

VIII-N-4 Intramolecular Energy-Band Dispersion in Oriented Thin Film of n - $CF_3(CF_2)_{22}CF_3$ Observed by Angle-Resolved UV Photoemission and its Theoretical Simulation

YOSHIMURA, Daisuke¹; ISHII, Hisao²; MIYAMAE, Takayuki³; HASEGAWA, Shinji⁴; OKUDAIRA K., Koji⁵; UENO, Nobuo; SEKI, Kazuhiko¹
(¹Nagoya Univ.; ²Tohoku Univ.; ³AIST; ⁴Fuji Xerox; ⁵Chiba Univ.)

[*Surf. Rev. Lett.* **9**, 407 (2002)]

Poly(tetrafluoroethylene) (PTFE) $(CF_2)_n$ is one of the most fundamental polymers, which is the perfluorinated analogue of polyethylene $(CH_2)_n$ with a simple repeating CF_2 unit. For such a one-dimensional polymer, we can expect the formation of one-dimensional intramolecular energy-band relation along the chain direction, and the energy-band structures of PTFE have been studied theoretically. Unfortunately, however, there was no experimental result to be compared with such calculated energy-band structure. In this work, we performed angle-resolved UV photoemission spectroscopy (ARUPS) with synchrotron radiation for the oriented thin films of perfluorotetracosane (n - $CF_3(CF_2)_{22}CF_3$; PFT), which is one of the oligomer of PTFE. The sample of PFT with their long chain axis being perpendicular to the surface was prepared by in-situ vacuum evaporation. The normal-emission spectra of the PFT film show incident photon energy dependence due to the intramolecular energy-band dispersion. We also performed the theoretical simulation of the spectra by using independent-atomic-center (IAC) approximation combined with *ab initio* MO calculations. The simulations successfully reproduced the $h\nu$ -dependence of the observed ARUPS spectra. From the observed and simulated spectra, we deduced the value of inner potential V_0 , which is the parameter defining the energy origin of the free-electron-like final state, and derived reliable energy-band dispersion relation.

VIII-O Study on Compact X-Ray Sources

Electron storage rings are useful and practical devices as x-ray sources. However, these synchrotron radiation facilities which can provide intense x-rays usually occupy large area and we need many costs in order to construct and maintain the facilities. So that there have been many works to investigate compact x-ray sources. Laser undulator radiation and backward Compton scattering which are generated by interaction of electron beams from small accelerators with intense laser photons are candidates to produce hard x-rays.

X-ray sources must be shielded for radiation safety. For constructing effective shields, we need to know how many radiations are yielded from our x-ray sources. We will use high energy electrons to produce x-rays. These electrons cause radiations when they interact with beam ducts or beam dumps, so that it is useful to study radiations generated in synchrotron radiation facilities in order to estimate the yields of radiations from our x-ray sources.

VIII-O-1 Study on Radiation Shielding for Small Synchrotron Radiation Facilities

TAKASHIMA, Yoshifumi; KUWAYAMA, Shunsuke¹; KOBAYAKAWA, Hisashi¹
(¹Nagoya Univ.)

X-ray sources using high energy electrons usually generate radiations which should be shielded. In order to design effective shields, we need to estimate how many radiations are generated from a storage ring and penetrate radiation shields. Circulating electrons in a storage ring go out of their stable orbit when their energy exceeds the critical energy. These electrons are incident on the beam duct and generate electromagnetic showers around the beam duct.

We measured angular distribution of radiations around a beam duct of the storage ring of UVSOR. Figure 1 shows experimental set up. Two Photodiodes were set in tandem in a copper case and coincident signal from these two photodiodes were counted, so that we detected only charged particles. The area of the photodiodes were $7 \times 7 \text{ mm}^2$. We used 12 pairs of photodiodes installed at about 2 m upstream from the inflector. Figure 2 shows an angular distribution of the number of signal from the detectors. We notice that the stray radiations of charged particles counted at inside of the ring are more than that counted at outside, because most electrons which exceed their energy over the bucket height hit on the inside wall of the beam duct.

In order to estimate the amount of the stray radiations around compact x-ray sources, we should investigate the spatial distribution of stray radiations by comparing experimental results and theoretical calculations. We will propose a simple formula to calculate radiation dose around a small accelerator. In order to check the accuracy of the formula, we should measure the radiations at many points around UVSOR storage ring and compare the experimental results with our calculations.

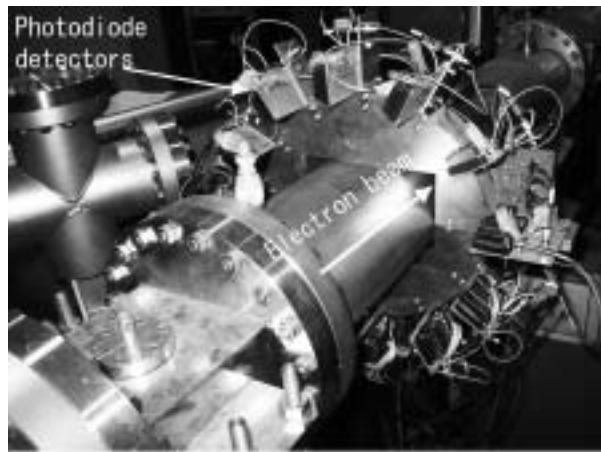


Figure 1. Experimental setup.

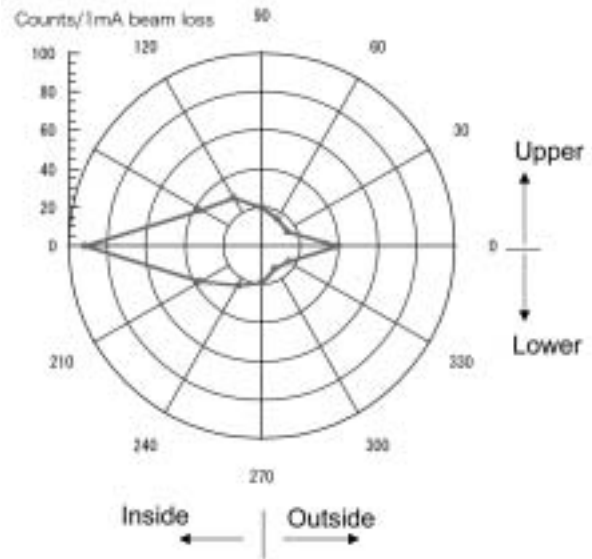


Figure 2. Angular distribution of charged particles around the beam duct of the storage ring of UVSOR.

VIII-P Syntheses of Fullerene-Based New Materials with Novel Physical Properties

Fullerene-based new materials are synthesized, and the structures and physical properties are studied in wide temperature and pressure regions. The structures and transport properties of pressure-induced superconducting fulleride, Cs_3C_{60} , are studied by X-ray powder diffraction, ESR, Raman, AC susceptibility and resistivity measurements, in order to clarify the mechanism of pressure-induced superconductivity. The structures and transport properties of metallofullerenes are also studied by X-ray diffraction and resistivity. The field-effect transistors (FET's) with thin-films of fullerenes are fabricated and their transport properties are studied in wide temperature region. STM studies on metallofullerenes adsorbed on Si(111)-(7×7) surface are performed under high vacuum condition.

VIII-P-1 Pressure and Temperature Dependences of the Structural Properties of Dy@C₈₂ Isomer I

TAKABAYASHI, Yasuhiro¹; KUBOZONO, Yoshihiro; KANBARA, Takayoshi¹; FUJIKI, Satoshi; SHIBATA, Kana²; HARUYAMA, Yusuke²; HOSOKAWA, Tomoko²; RIKIISHI, Yoshie²; KASHINO, Setuo²
(¹IMS and Okayama Univ.; ²Okayama Univ.)

[*Phys. Rev. B* **65**, 73405 (2002)]

Crystals of Dy@C₈₂ isomer I are studied by x-ray powder diffraction with synchrotron radiation in wide temperature and pressure regions. The isomer I of Dy@C₈₂ shows a simple cubic structure with lattice constant, a , of 15.85(3) Å at 298 K, while the isomer II shows a face-centered cubic structure with a of 15.75(4) Å. The structural phase transition of the second-order is indicated for the isomer I at 300–310 K by the temperature dependence of x-ray diffraction and differential scanning calorimetry. Further, the pressure dependence of the lattice constant is studied for the isomer I up to 60 kbar, which can be fitted by a Murnaghan equation of state.

VIII-P-2 Ferromagnetism and Giant Magnetoresistance in the Rare-Earth Fullerides Eu_{6-x}Sr_xC₆₀

ISHII, Kenji^{1,2}; FUJIWARA, Akihiko¹; SUEMATSU, Hiroyoshi¹; KUBOZONO, Yoshihiro
(¹Univ. Tokyo; ²JAERI)

[*Phys. Rev. B* **65**, 134431 (2002)]

We have studied crystal structure, magnetism, and electric transport properties of a europium fulleride Eu₆C₆₀ and its Sr-substituted compounds, Eu_{6-x}Sr_xC₆₀. They have a *bcc* structure, which is an isostructure of other $M_6\text{C}_{60}$ (M represents an alkali atom or an alkaline-earth atom). Magnetic measurements revealed that magnetic moment is ascribed to the divalent europium atom with $S = 7/2$ spin, and a ferromagnetic transition was observed at $T_c = 10$ –14 K. In Eu₆C₆₀, we also confirm the ferromagnetic transition by heat-capacity measurement. The striking feature in Eu_{6-x}Sr_xC₆₀ is very large negative magnetoresistance at low tempera-

ture; the resistivity ratio $\rho(H = 9 \text{ T})/\rho(H = 0 \text{ T})$ reaches almost 10^{-3} at 1 K in Eu₆C₆₀. Such large magnetoresistance is the manifestation of a strong π - f interaction between conduction carriers on C₆₀ and $4f$ electrons of Eu.

VIII-P-3 Bridging Fullerenes with Metals

CHI, Dam Hieu¹; IWASA, Yoshihiro^{1,2,3}; CHEN, X. H.⁴; TAKENOBU, Taishi²; ITO, Takayoshi¹; MITANI, Tadaoki¹; NISHIBORI, Eiji⁵; TAKATA, Masaki⁵; SAKATA, Makoto⁵; KUBOZONO, Yoshihiro
(¹JAIST; ²Tohoku Univ.; ³CREST; ⁴Univ. Sci. Tech. China; ⁵Nagoya Univ.)

[*Chem. Phys. Lett.* **359**, 177 (2002)]

The bonding nature between rare earth metals and fullerene molecules has been investigated. The electron density distribution for nominal Sm₃C₇₀, calculated by a maximum entropy method (MEM) based on the Rietveld analysis of synchrotron X-ray diffraction pattern, unambiguously demonstrated a covalent Sm...C bond, which is almost as strong as the interatomic bonding of crystal Si. Furthermore, the Sm bridges two C₇₀ molecules, producing a C₇₀...Sm...C₇₀ dimer structure.

VIII-P-4 Structure and Physical Properties of Cs_{3+α}C₆₀ (α = 0.0–1.0) under Ambient and High Pressures

FUJIKI, Satoshi; KUBOZONO, Yoshihiro; KOBAYASHI, Mototada²; KAMBE, Takashi¹; RIKIISHI, Yoshie¹; KASHINO, Setuo¹; ISHII, Kenji³; SUEMATSU, Hiroyoshi³; FUJIWARA, Akihiko⁴
(¹Okayama Univ.; ²Himeji Inst. Tech.; ³Univ. Tokyo; ⁴JAIST)

[*Phys. Rev. B* **65**, 235425 (2002)]

The intermediate phases, Cs_{3+α}C₆₀ (α = 0.0–1.0), have been prepared, and their structure and physical properties are studied by x-ray powder diffraction, Raman, ESR, electric conductivity and ac susceptibility measurements under ambient and high pressures. The x-ray powder diffraction pattern of Cs_{3+α}C₆₀ (α = 0.0–

1.0) can be indexed as a mixture of the body-centered-orthorhombic (*bco*) and cubic (A15) phases. The A15 phase diminishes above 30 kbar. The broad ESR peak due to conduction electron (*c*-ESR) is observed only for the phases around $\alpha = 0.0$ in $C_{S_{3+\alpha}}C_{60}$. The resistivity of the $C_{S_{3+\alpha}}C_{60}$ ($\alpha \neq 0$) sample follows the granular metal theory and/or Sheng model even in the sample exhibiting a broad ESR peak. No superconducting transition is observed up to 10.6 kbar in $C_{S_{3+\alpha}}C_{60}$ ($\alpha \neq 0$). These results present that *bco* phase of $C_{S_{3+\alpha}}C_{60}$ ($\alpha = 0$) is a final candidate for a pressure-induced superconductor.

VIII-P-5 Complex-Plane Impedance Study on a Hydrogen-Doped Copper Coordination Polymer: *N,N'*-bis-(2-hydroxy-ethyl)-Dithiooxamidato-Copper(II)

NAGAO, Yuki¹; IKEDA, Ryuichi¹; KANDA, Seiichi²; KUBOZONO, Yoshihiro; KITAGAWA, Hiroshi^{1,3,4}

(¹Univ. Tsukuba; ²Univ. Tokushima; ³JAIST; ⁴JST)

[*Mol. Cryst. Liq. Cryst.* **379**, 89 (2002)]

AC conductivity measurements with an impedance analyzer were carried out for a hydrogen-doped coordination polymer, *N,N'*-bis-(2-hydroxy-ethyl)-dithiooxamidato-copper(II), in order to estimate the protonic conductivity (σ_p). The $\log \sigma_p$ was linearly increased from 2.6×10^{-9} to 2.2×10^{-6} Scm^{-1} with relative humidity (RH) from 45 to 100% at 300 K. A slight hysteresis of protonic conductivity was observed upon increasing and decreasing RH, which implies that H_3O^+ is generated by a reaction between water molecule and acid-base polymer near $\text{RH} \sim 100\%$.

VIII-P-6 Crystal Structure and Electronic Transport of Dy@C₈₂

KUBOZONO, Yoshihiro; TAKABAYASHI, Yasuhiro¹; SHIBATA, Kana²; KANBARA, Takayoshi¹; FUJIKI, Satoshi; KASHINO, Setuo²; FUJIWARA, Akihiko³; EMURA, Shuichi⁴

(¹IMS and Okayama Univ.; ²Okayama Univ.; ³JAIST; ⁴Osaka Univ.)

[*Phys. Rev. B* submitted]

Crystal structure of Dy@C₈₂ isomer I at 298 K has been determined by Rietveld refinement for X-ray powder diffraction with synchrotron radiation. The isomer I shows a simple cubic structure (sc: $Pa\bar{3}$) with a lattice constant, a , of 15.78(1) Å. The C₂ axis of a C_{2v}-C₈₂ cage aligns along a [111] direction of this crystal lattice. The C₈₂ cage is orientationally disordered to satisfy a $\bar{3}$ symmetry along [111] which is requested in this space group. The large thermal parameter for the Dy atom estimated from the X-ray diffraction probably reflects a large disorder caused by a floating motion of the Dy atom inside the C₈₂ cage as well as a ratchet-type motion of the Dy@C₈₂ molecule. The electronic transport of thin film of Dy@C₈₂ shows a semi-conducting behavior. The energy gap, E_g , is estimated to

be 0.2 eV. Further, the variation of valence from Dy³⁺ to Dy²⁺ is found by metal-doping into the Dy@C₈₂ crystals.

VIII-P-7 N-Channel Field-Transistors with Thin Films of Fullerenes

KANBARA, Takayoshi²; FUJIKI, Satoshi²; SHIBATA, Kana¹; KUBOZONO, Yoshihiro¹; URISU, Tsuneo; SAKAI, Masahiro; FUJIWARA, Akihiko³

(¹Okayama Univ.; ²IMS and Okayama Univ.; ³JAIST)

[*Phys. Rev. B* submitted]

N-channel field effect transistors (FETs) are fabricated with thin films of C₆₀, C₇₀ and Dy@C₈₂, and an SiO₂ insulating layer. The transport properties of the C₆₀ and C₇₀ FET's are studied in a temperature region from 200 to 330 K. The typical FET properties are observed in C₆₀ and C₇₀ above 220 K. The hopping transport with activation energy of 0.3 eV is observed for the C₆₀ and C₇₀ FET's in this temperature region. Further, the condition of fabrication is studied in order to improve the FET property. The Dy@C₈₂ FET is first fabricated and its property is studied at 295 K.

VIII-P-8 STM Study of Dy@C₈₂ on Si(111)-(7×7) Surface

FUJIKI, Satoshi; KUBOZONO, Yoshihiro; KANBARA, Takayoshi¹; FUJIWARA, Akihiko²; HOSOKAWA, Tomoko¹; URISU, Tsuneo

(¹Okayama Univ.; ²JAIST)

[to be submitted]

Single-molecule image of Dy@C₈₂ on Si(111)-(7×7) surface is observed by STM. The Dy@C₈₂ molecules were deposited on the Si(111)-(7×7) surface under UHV chamber. The first layer of Dy@C₈₂ is disordered, and no second layer islands are found before the complete formation of the first layer of Dy@C₈₂. A single-molecule image of Dy@C₈₂ was clearly observed on the first layer. This image shows that the maximum height of the molecule is ~ 11.3 Å which corresponds to those of two long axes of Dy@C₈₂ inclusive of van der Waals radius of C atom. The STS of the multilayer of Dy@C₈₂ suggests a energy gap of 0.1 eV at 295 K, in consistent with that, 0.2 eV, determined by resistivity measurement for the Dy@C₈₂ thin film. This shows that the Dy@C₈₂ molecule is a small-gap semiconductor.

VIII-Q Effects of High Magnetic Field on Chemical Process

It is interesting to control chemical and physical process with the aid of magnetism which is one of the key properties of matter. This research group is studying the mechanisms of the interaction of matter and magnetic field in order to develop a new technique to control chemical and physical process by magnetic field. In the anodic oxidation reaction of potassium iodide, significant magnetic field effects (≤ 0.6 T) on the product yields are interpreted in terms of the Lorentz force on iodide ions. In the liquid/solid redox reaction of silver ion and copper metal, anomalous magnetic field effects (≤ 15 T) are chiefly explained by the magnetic force on generated copper ions. It is clarified that mass transportation in solution is remarkably affected by the magnetic field.

VIII-Q-1 Magnetic Field Effects on Anodic Oxidation of Potassium Iodide

UECHI, Ichiro¹; FUJIWARA, Masao¹; FUJIWARA, Yoshihisa²; YAMAMOTO, Yohsuke²; TANIMOTO, Yoshifumi¹

(¹IMS and Hiroshima Univ.; ²Hiroshima Univ.)

[*Bull. Chem. Soc. Jpn.* in press]

External magnetic fields (≤ 6 kG) significantly increase yields of I_3^- and H_2 as well as anodic currents in anodic oxidation of potassium iodide. At 0.7 V, the ratio of the current at 6 kG and at 0 kG is about 1.7, whereas that of I_3^- yield is 1.2. The ratio of the H_2 yield is 1.4 at 2 kG. The Lorentz force on ions in the solution induces convection of solution (MHD flow), resulting in acceleration of the entire reaction rate. The MHD flow of the solution is confirmed from the visual observation that reddish-brown streams of I_3^- in the solution, moving downward at zero field, undergo turbulent motion in magnetic fields. Small magnetic field effect on the I_3^- yield, compared to that on the anodic current, is attributable to the fact that the reaction of I_3^- and OH^- , generated at the cathode, is also enhanced by the MHD flow.

VIII-Q-2 High Magnetic Field Effect on the Growth of 3-Dimensional Silver Dendrites

KATSUKI, Akio¹; UECHI, Ichiro; FUJIWARA, Masao; TANIMOTO, Yoshifumi

(¹Shinshu Univ.)

[*Chem. Lett.* submitted]

A liquid/solid redox reaction between silver ion and copper metal is investigated under high vertical magnetic field (maximum field strength: 15 T). The magnetic field causes drastic changes in the color and shape of silver dendrites. At zero field, branches of metallic silver grow on the gray and cylindrical dendrites. In the presence of magnetic field, the dendrites are black in color and almost spherical in shape. The dendrites in magnetic field are denser than those at zero field. In the presence of the magnetic field, yields of silver dendrite and copper ion increase by 1.3–2. These effects are chiefly interpreted in terms of the magnetic force in copper ion in solution. As the reaction progresses, paramagnetic copper ions are generated. These ions are attracted by the magnetic force, leading to the convection of the solution.

VIII-R Theoretical and Computational Study on Gas Phase Reactions and Chromic Molecules

Quantum chemical calculations are used to produce potential energy surface (PES) to do reaction dynamics simulations. We develop the methodology to generate PES efficiently and/or automatically using quantum chemical calculation results. Another interest of our group is theoretical explanation and prediction of structural and spectral changes of photochromic and electrochromic substances.

VIII-R-1 Polycyano–Polycadmte Host Clathrates Including a Methylviologen Dication. Syntheses, Crystal Structures and Photo-Induced Reduction of Methylviologen Dication

YOSHIKAWA, Hirofumi¹; NISHIKIORI, Shin-ichi¹; WATANABE, Tokuko²; ISHIDA, Toshimasa³; WATANABE, Go³; MURAKAMI, Makoto³; SUWINSKA, Kinga⁴; LUBORADZKI, Roman⁴; LIPKOWSKI, Janusz⁴

(¹Univ. Tokyo; ²Tokyo Univ. Fisheries; ³Shizuoka Univ.; ⁴Polish Acad. Sci.)

[*J. Chem. Soc., Dalton Trans.* 1907 (2002)]

A series of polycyano-polycadmte host clathrates including a methylviologen dication (MV²⁺), which is a photo-hemically active electron acceptor, and an organic molecule, such as alcohols, haloalkanes, ethers and small aromatics, and two complexes built of a polycyano-polycadmte and MV²⁺ were synthesized. The single crystal X-ray diffraction experiments on ten clathrates and the two complexes revealed their 3-D network polycyano-polycadmte structures built of Cd²⁺ ions and CN. bridges. The network structures are classified into five structure types. Type I, II and III were found in the clathrates, and Type IV and V were turned up in the two complexes. Type I and II have cage-like cavities and each of the cavities includes one guest, MV²⁺ or an organic molecule. Type III has a channel-like cavity where MV²⁺ ions and organic molecules are included. Type IV and V have 3-D space, which is neither a cage-like cavity nor a channel-like cavity, for embracing MV²⁺. Although all compounds were colorless and the formation of a charge transfer complex between MV²⁺ and a neutral guest in the clathrates was not confirmed from the structural data and diffuse reflectance spectra, some of them showed a color change from colorless to blue on UV irradiation, and which arose from the reduction of MV²⁺ to a methylviologen radical MV^{•+}.

VIII-R-2 IR Absorption Spectra of Electrochromic WO₃ Films

KONOSHIMA, Koji¹; GOTO, Takeshi; ISHIDA, Toshimasa¹; URABE, Kazuo¹; KITAO, Michihiko¹
(¹Shizuoka Univ.)

[*Trans. Mater. Res. Soc. Jpn.* 27, 349 (2002)]

WO₃ films were prepared by thermal evaporation. IR absorption spectra of the films were measured for

various amount of injected protons. Three peaks of $\nu(\text{W-OH})$, $\nu(\text{W=O})$ and $\nu(\text{O-W-O})$ vibrations were observed. With increasing of injected protons, the intensity of peak of $\nu(\text{W-OH})$ increased and its position shifted hugely from 3200 to 2400 cm⁻¹. We calculated various bond-patterns of OH vibrations. Then OH vibrations accompanied with hydrogen bonds are plausible for observed OH peaks. On the other hand, with increasing of injected protons the intensity of peak of $\nu(\text{W=O})$ bond also increased, but its position shifted a little. It is considered that parts of W-O-W-O-W bonds were broken by injected protons and then W=O bonds were brought about.

VIII-R-3 A Local Interpolation Scheme Using No Derivatives in Potential Sampling: Application to O(¹D) + H₂ System

ISHIDA, Toshimasa; SCHATZ, George C.¹
(¹Northwestern Univ.)

[*J. Comput. Chem.* submitted]

We recently proposed a local interpolation scheme, in which interpolant moving least squares (IMLS) and Shepard interpolation are employed to describe potential energy surfaces. This IMLS/Shepard scheme is applicable to do potential interpolation with quantum chemical results for which analytical derivatives are not available. In this study, we apply the scheme to the highly exothermic O(¹D) + H₂ → H + OH reaction and compare it with results based on Shepard interpolation using second order Taylor expansions. An analytical surface is used to define the potential function so that errors in the interpolation function may accurately be determined. We found that the present scheme reproduces the correct reactive cross sections more accurately than the Shepard scheme, and with rms errors for energy and gradients that are significantly smaller than those from Shepard interpolation. This occurs even though the present scheme does not utilize derivative and hessian information whereas the Shepard interpolation does. The Bayesian approach proposed by Bettens and Collins does not improve the IMLS/Shepard results significantly although it does the Shepard-only approach. The accuracy in the IMLS/Shepard scheme is surprising, but can be explained by the more global nature of the interpolation.

VIII-R-4 Theoretical Study on Photoinduced Color Change and Charge Transfer of Methylviologen

ISHIDA, Toshimasa; MURAKAMI, Makoto¹;

WATANABE, Go¹; YOSHIKAWA, Hirofumi²;
NISHIKIORI, Shin-ichi²
(¹Shizuoka Univ.; ²Univ. Tokyo)

[*Internet Electron. J. Mol. Des.* submitted]

Motivation. Methylviologen dication is easily reduced to be a monocation radical, and turned to be blue, and forms a charge-transfer complex with a donor molecule. Yoshikawa *et al.* recently reported photo-induced reduction and charge transfer complexes in polycyanopolycadmate host clathrates. We study the reduction using quantum chemical calculations. The energy changes with the torsion angle of the two cations and the spectral change, solvent effect and the charge transfer between the dication and other guest molecules in the clathrates are investigated.

Method. The Hartree-Fock and CI singles, time dependent DFT calculations are carried out for the ground state and excited states of the two cations. Solvation effect is treated with the polarizable continuum model, and the charge transfer in the clathrates is modeled based on crystal structures determined experimentally.

Results. The optimized geometry of the monocation radical was found to be planar while that of the dication is twisted. These results are consistent with recent calculations for related compounds. The color change upon the photoreduction was reproduced by the calculation. The solvent effect of acetonitrile was found to be small. Charge transfer absorption was reproduced for the mesitylene-methylviologen dication complex in the clathrate host using a small model.

Conclusions. The geometrical and the color change was reproduced satisfactorily. The TDDFT scheme reproduces the observed spectra better than the CIS scheme, but the latter scheme is still valuable to evaluate qualitative feature of spectra.

VIII-R-5 Potential Energy Surface Generation Using Ab Initio Calculations and IMLS/Shepard Interpolation for the $\text{LiH} + \text{H} \rightleftharpoons \text{Li} + \text{H}_2$ Reactions

KIM, Kyoung Hoon¹; LEE, Yoon Sup¹; JEUNG, Gwang-Hi²; ISHIDA, Toshimasa³
(¹Korea Adv. Inst. Sci. Tech.; ²Univ. Paris-Sud;
³Shizuoka Univ.)

[*J. Chem. Phys.* submitted]

CASSCF following MRCI calculations are employed to generate potential energy surfaces for the reaction of $\text{LiH} + \text{H} \rightleftharpoons \text{Li} + \text{H}_2$ and analyze the reactive region for the reaction. Spectroscopic data for LiH and H_2 obtained by our scheme are in good agreement with experiment results. IMLS combined with Shepard interpolation method is used to interpolate the Potential energy surfaces. Trajectory calculations for $\text{LiH} + \text{H} \rightarrow \text{Li} + \text{H}_2$ on the interpolated potential energy surface illustrate that the initial vibrational content of LiH plays a rather minor role which is explained by the fact there is no energy barrier for the reaction $\text{LiH} + \text{H} \rightarrow \text{Li} + \text{H}_2$, and the reactive cross section has maximum value, when the initial collision energy is about 0.1 eV. Trajec-

tory calculations for $\text{Li} + \text{H}_2 \rightarrow \text{LiH} + \text{H}$ show that the reaction requires highly excited $\text{H}_2(v \geq 4)$ molecules for it to occur at low collision energy and it is more efficient to put the same amount energy into the H_2 vibration energy rather than translational energy.

VIII-S Macromolecular Self-Assembly Opens a Way to the Development of Novel Materials that Have Characteristics of Cellular Systems

In cellular systems, assembly of devices (*e.g.* enzymes) into complexes is a principle to construct supramolecular apparatuses and ensure the specificity, fidelity, and efficiency of intracellular events. Exchangeability of the components of the complex is also advantageous for adaptation to the environment and metabolism of the apparatus. For global, sustainable development, in our opinion, readiness for the adaptation and decomposition is required for any future materials and systems such as highly integrated device arrays. Utilizing elaborate macromolecular self-assemblies, we thus aimed at development of artificial systems endowed with energy- and entropy-saving properties: the system can be formed and function on demand, and are readily reusable, repairable, and bio-degradable. We attempt to fabricate the nano-systems for energy conversion and computing; for their basis, we also study on molecular mechanisms of photosynthesis and signal transduction. Our study should serve a new design concept for nano- and molecular-scale intelligent materials (see also Special Research Project (c)).

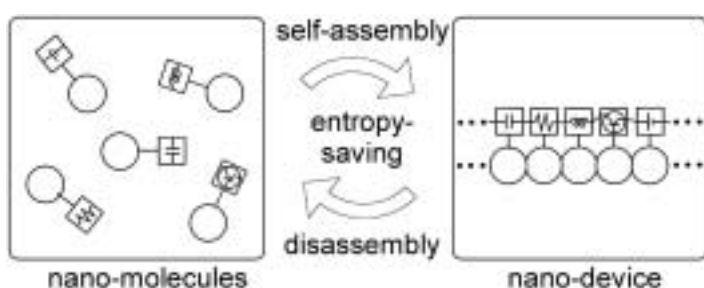


Figure 1. A concept of the “entropy-saving” nano-materials.

VIII-S-1 Fabrication of “Entropy-Saving” Nano-Solar-Cells

OBA, Toru; HANASAKI, Mitsuru¹; MINABE, Masahiro¹
(¹Utsunomiya Univ.)

Photosynthetic apparatuses in living organisms are, in common, assemblies of light-harvesting antenna parts and reaction centers (RCs) where energy conversion occur. Nano-scale order in the assembled supramolecular structure contributes efficient function. The assembly is advantageous to light adaptation and metabolism. These facts suggest that elaborate self-assembly of macromolecular components can provide solar-cells that can be formed and function on demand. We developed such device utilizing cytoskeletal nano-tubes, “microtubules” (MTs). The component protein “tubulin” (Tub) molecules assemble to form MTs at 37 °C in the presence of nucleotide, and MTs disassemble to Tubs at 0 °C. We prepared Tubs conjugated with a fluorophore for the antenna part and a photosensitizer-labeled hemoprotein for the RC, respectively. The modified Tubs were mixed and the temperature of the solution was switched simply. Only in the Tub-assembled state (MTs), solar energy absorbed by the antenna parts migrated to the sensitizer, leading to charge separation in the RC, as occurs in photosynthesis. The device reversibly functioned at each Tub-assembled state in the course of the Tub-assembly / MT-disassembly cycles.

VIII-S-2 Model Study on Signaling Behaviors of Scaffold Proteins—Toward its Application to Novel Computing Devices—

OBA, Toru; FUJIWARA, Umihito¹; MINABE, Masahiro¹
(¹Utsunomiya Univ.)

Scaffold proteins, found in postsynaptic termini, can bind several members of a signaling cascade to form a supramolecular complex, which may contribute to rapidity, fidelity, and selectivity of signal transduction.¹⁾ Such a mechanism can correlate to learning and memory formation. Due to the limitation of the experiments, however, no detailed model of scaffold action has been reported except for numerical simulations. We utilized a eukaryotic cytoskeleton ‘microtubule’ (MT) for fabrication of a model of the signaling complexes. We conjugated both glucose oxidase (GOx) and horseradish peroxidase (HRP) on the surface of an MT by use of the avidin-biotin interaction. The upstream effector (GOx) converted an input signal (*D*-glucose) into a second messenger (H₂O₂) that was diffusely supplied to the downstream effector (HRP) and converted into an output signal (Dye). It was found that sensitivity of the system to the stimulus increased with increasing density of the effectors on a MT. Further examinations of this model system may contribute to development of novel computing devices.

Reference

- 1) U. Thomas, “Modulation of synaptic signalling complexes by Homer proteins,” *J. Neurochem.* **81**, 407 (2002).

VIII-S-3 Physicochemical Studies on the Molecular Mechanism of Photosynthesis

OBA, Toru; TAMIYAKI, Hitoshi¹

(¹Ritsumeikan Univ.)

[*Photosynth. Res.* in press]

Since chlorophyll *a* and bacteriochlorophyll *a* are asymmetric molecules (Figure 1), an external ligand can coordinate to the central Mg atom either from the chlorin macrocycle side where the C13²-methoxycarbonyl moiety protrudes (denoting as the 'back' side) or from the other side (the 'face' side). We investigated which side of the macrocycle is favored for the ligand coordination, by survey of the highly resolved crystal structures of various photosynthetic proteins and theoretical model calculations. It is found that chlorophyll *a* as well as bacteriochlorophylls *a* and *b* in the photosynthetic proteins mostly bind their ligands on the 'back' sides. This finding was confirmed by the theoretical calculations for methyl chlorophyllide *a* and methyl bacteriochlorophyllide *a* as models: the 'back' type ligand-(bacterio)chlorophyll complex was more stable than the 'face' type one. The calculations predicted influence of the C13²-stereochemistry on the choice of the side of the ligand coordination, which may be correlated to the presence of the C13²-epimer of chlorophyll *a* in photosystem I reaction center.¹⁾

Reference

- 1) P. Jordan, P. Fromme, H. T. Witt, O. Klukas, W. Saenger and N. Krauß, "Three-dimensional structure of cyanobacterial photosystem I at 2.5 Å resolution," *Nature* **411**, 909 (2001).

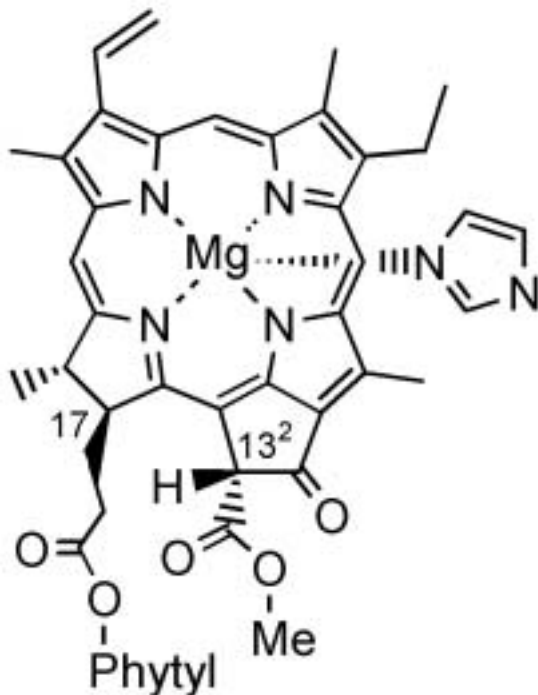


Figure 1. Molecular structure of the 'back' type chlorophyll *a*-imidazole complex.

Equipment Development Center

VIII-T Development of “Special Machine”

The technical staff of the Equipment Development Center is partly engaged in planning, researching, designing and constructing “Special machine.” This machine, is a high-tech experimental instrument, with emphasis on new technical idea and co-operative work with members inside and outside the Institute including those in industries. We collect suggestions of new instruments once every year from Professors and Associate Professors of IMS.

In this fiscal year, 2001, one project theme was adopted as Special machine.

VIII-T-1 Development of Twin-Probe Scanning Tunneling Microscope

YAMADA, Ryo; TADA, Hirokazu; YOSHIDA, Hisashi; MATSUSHITA, Kouji; SUZUI, Mitsukazu; KONDO, Takuhiko

It is important to study electrical properties of materials in nm scale for the construction of electronic devices in the same scale. Scanning probe microscopy (SPM) is one of the most powerful methods to measure local properties of solid surfaces in nm ~ atomic scales. Most of the SPM uses a single probe and, therefore, it is difficult to measure the transport properties of nanoscale structures.

We constructed a twin probe scanning tunneling microscope which has two independently driven probes. By using this instrument, it is expected to be possible to measure electrical transport properties such as resistance as a function of a distance between two probes in nano-scale.

The whole instruments were placed on a spring damper to be isolated from the mechanical vibrations. Two tube piezos which were used for the fine adjustment of the tip positions were fixed beneath steel beams. The beams were placed on commercially available microstage (Melles Griot) used for coarse adjustment of the tip positions. A current-to-voltage converter with a sensitivity of 1 nA/V was fabricated. It is used to measure a current flowing between the probe and the sample and that flowing between the each probe when the bias voltage is applied to the sample and one of the probes, respectively. The measured current was fed into the commercially available SPM controller (JEOL) and surface morphology was obtained by scanning the probe in x - y plane by the tube piezos keeping the current constant by controlling the z position of the probe.

Figure 1 shows an image of HOPG surface obtained by the instrument. Atomically flat terraces and mono-atomic steps were imaged independently by two probes at the same time. We are now optimizing the resolution and fabricating a sharper tip to get two probes closer each other.

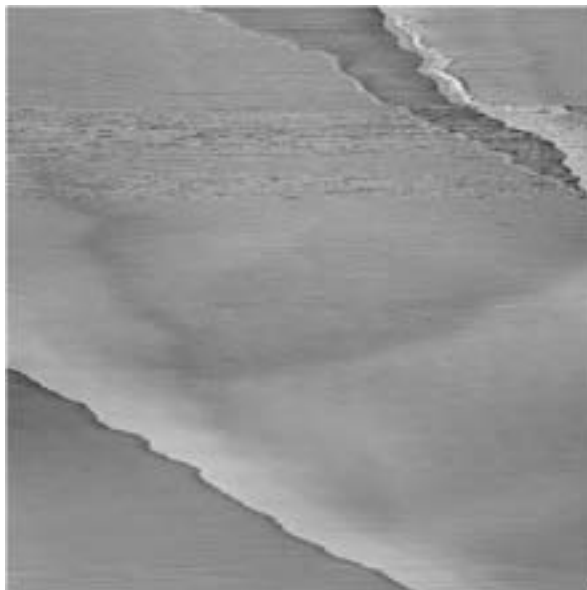


Figure 1. An STM image of HOPG surface.

Ultraviolet Synchrotron Orbital Radiation Facility

VIII-U Development of the UVSOR Light Source

VIII-U-1 Development of Lattice Components for UVSOR Upgrade Project

KATOH, Masahiro; HAYASHI, Kenji; HONDA, Toru¹; HORI, Yoichiro²; HOSAKA, Masahito; KINOSHITA, Toshio; KODA, Shigeru³; TAKASHIMA, Yoshifumi; YAMAZAKI, Jun-ichiro; KITAMURA, Hideo⁴; HARA, Toru⁴; TANAKA, Takashi⁴

(¹KEK-PF; ²IMS and KEK-PF; ³Saga Univ.; ⁴RIKEN)

We have been developing the lattice components for the UVSOR upgrade project. In this project, the original DBA lattice of the storage ring will be modified to have lower emittance and more straight sections available for insertion devices. The reconstruction will be started in March 2003 and be completed until the end of May. All the quadrupole and sextupole magnets will be replaced with combined function multi-pole magnets, which is capable of producing both quadrupole field and sextupole field. We constructed a prototype and measured the magnetic field. The results have shown that the required field strength and field quality was well realized. We have completed the design of the vacuum system. Their fabrication will be started in September 2002 and be completed until the end of February.

VIII-U-2 Storage Ring Free Electron Laser

HOSAKA, Masahito; KATOH, Masahiro; HAYASHI, Kenji; KINOSHITA, Toshio; KODA, Shigeru¹; TAKASHIMA, Yoshifumi; YAMAZAKI, Jun-ichiro

(¹Saga Univ.)

At the UVSOR, performance of the free electron lasers has been improved aiming users applications. The average output power has reached 1W level, which is the world highest record as a storage ring free electron laser (SRFEL). SRFEL have a potentiality for scientific applications as a unique light source because of variable wavelength, good coherence, temporal structure, and perfect synchronization with synchrotron radiation (SR). We started an experiment using SRFEL combined with SR. We have succeeded to observe the double-resonant excitation of Xe by using SR and SRFEL as pump and probe lights, respectively.

VIII-U-3 Ion Trapping at UVSOR

MOCHIIHASHI, Akira; KATOH, Masahiro; HAYASHI, Kenji; KINOSHITA, Toshio; HOSAKA, Masahito; TAKASHIMA, Yoshifumi; YAMAZAKI, Jun-ichiro

An ion-related vertical instability of the UVSOR electron storage ring was observed in a multi-bunch mode with empty buckets (a bunch gap). In contrast to a shorter bunch train, it was clearly seen that vertical betatron tune had step-like changes with decrease of a beam current in a longer train. The step-like change in the tune seems to be caused by sudden change in condition of stability of trapped ions. Change in amplitude of the vertical betatron oscillation along a bunch train was also observed with a bunch-by-bunch beam diagnostic system. The structure of the amplitude seems to have relation to modulation of the ion density along the train.

VIII-U-4 Design Study of Vacuum System Improvement

HORI, Yoichiro; YAMAZAKI, Jun-ichiro; KATOH, Masahiro; HAYASHI, Kenji; HOSAKA, Masahito; KINOSHITA, Toshio; MOCHIIHASHI, Akira

In the UVSOR upgrade project, vacuum beam chambers in straight sections must be replaced to new ones designed for new magnets and their arrangement, and three bending chambers need to be renewed for re-equipment of beam-lines. In the remodeling, the pumping speed distribution should be considered in order to maintain a long beam lifetime in the upgraded ring. The pump arrangement by which a required operating pressure can be achieved was searched by a simple simulation of the pressure distribution. The simulation suggests that the pump location is essential in the straight section, and that the lifetime can be expected to extend up to 10–30 % by reinforcing the pumping speed in every bend section. Also a thermal/structural analysis of the chamber has been carried out for the 500 mA storage. Though the present concept of the stainless steel with partially water-cooling will be inherited, the use of copper material is locally desirable for the parts suffered intense SR. New chambers have been designed in detail with applying above results.

VIII-V Researches by the USE of UVSOR

VIII-V-1 Non-Radiative Decay of the Core Excitons in Auger-Free Luminescence Materials, CsCl and BaF₂

KAMADA, Masao; ITOH, Minoru¹
(¹Shinshu Univ.)

[*Phys. Rev. B* **65**, 245104 in press]

The present work has been conducted to understand the decay processes of the Cs-5*p* and Ba-5*p* core excitons in CsCl and BaF₂, respectively, where the Auger decay process of the Cs-5*p* and Ba-5*p* core holes is energetically forbidden. The core-exciton peaks are missing in the excitation spectra for the Auger-free luminescence, which arises from a radiative decay of the valence electrons into these core holes. Resonant enhancement effects of the valence-band photoelectron spectra are observed around 13 eV for CsCl and 17 eV for BaF₂. The effects are attributed to the non-radiative decay through the direct-recombination process of an excited electron and the Cs-5*p* or Ba-5*p* core hole forming the core exciton. It is also found that the core exciton deforms its surrounding lattice with relaxation energy of about 0.3 eV in CsCl and 0.9 eV in BaF₂. The non-radiative direct-recombination probabilities of the core excitons are estimated to be about 32 and 75% for CsCl and BaF₂, respectively, by taking account of the lattice relaxation effects.

VIII-V-2 Photoelectron Spectroscopic Study on Photo-Induced Phase Transition of Spin-Crossover Complex

KAMADA, Masao; TAKAHASHI, Kazutoshi; DOI, Yo-ichiro¹; FUKUI, Kazutoshi¹; TAYAGAKI, Takeshi²; TANAKA, Ko-ichiro²
(¹Fukui Univ.; ²Kyoto Univ.)

[*Phase transition* **41-47**, in press]

Valence band structures in various phases of an organometal spin-crossover complex [Fe(2-pic)₃]Cl₂·EtOH have been measured by means of photoelectron spectroscopy based on the combination of synchrotron radiation and laser light. The valence band structure showed the remarkable change due to the photo-induced phase transition at low temperatures as well as the thermally induced phase transition, but the structure of the photo-induced phase was very different from that of the high-temperature phase. The DV-X α calculation based on the FeN₆ cluster was in good agreement with the photoelectron spectra. The present results indicate that the electronic structures originating from Fe and N ions are closely related to the photo-induced phase transition.

VIII-V-3 Surface-Photovoltage Effect in GaAs-GaAsP Super-Lattice Studied with Combination of Synchrotron Radiation and the Laser

TANAKA, Senku¹; MORÉ, Sam D.; TAKAHASHI, Kazutoshi; KAMADA, Masao; NISHITANI, Tomohiro²; NAKANISHI, Tsutomu²
(¹GUAS; ²Nagoya Univ.)

[*SPIN2000* 1000 (2001)]

Core-level photoelectron spectroscopy with the combination of synchrotron radiation (SR) and a laser was used for exploring the surface-photovoltage (SPV) effect and its temporal profiles in a GaAs/GaAsP super-lattice (SL). It was observed that the SPV value in the SL is suppressed as compared with a bulk GaAs. However, no significant difference was found in the temporal profile between the bulk and the SL. It is suggested that the suppression of the SPV in the SL is dominantly due to the small value of band bending under thermal equilibrium.

VIII-V-4 Pump/Probe Experiments with FEL and SR Pulses at UVSOR

GEJO, Tatsuo; SHIGEMASA, Eiji; NAKAMURA, Eiken; HOSAKA, Masahito; MOCHIHASHI, Akira; KATOH, Masahiro; YAMAZAKI, Jun-ichiro; HAYASHI, Kenji; TAKASHIMA, Yoshifumi; HAMA, Hiroyuki¹
(¹Tohoku Univ.)

Synchrotron radiation free electron lasers (SRFEL or FEL) has been used as a light source because of high power, high coherence and its unique temporal feature. Pump and probe experiments using FEL and synchrotron radiation (SR) pulses have been tried to perform for the last decade. This is due to the fact that the FEL pulse naturally synchronizes with the SR pulse. As the first gas-phase experiment combined FEL with SR, we have carried out the two-photon double-resonant excitation on Xe atoms, utilizing a SR pulse as a pump and an FEL pulse as a probe light.

The experiments were performed on BL7B at UVSOR, where a 3-m normal incidence monochromator is installed. The monochromatized SR from a bending magnet was used as the pump light. The estimated photon flux at BL3A1 is about 1×10^{13} photons/sec/0.1%B.W./100 mA, whereas that at BL7B is in the order of 10^9 . The FEL pulses were extracted through the backward mirror, and transported to the experimental station through a series of multi-layer mirrors. The flight path of FEL, which was adjusted to synchronize the timing between the FEL and the SR pulses, was about 30 m. Fine-tuning of the delay timing was made by using a movable optical delay system (50 cm) at the experimental station. The FEL and SR pulses introduced, coaxially crossed an effusive jet of Xe atoms from a gas nozzle. The singly charged Xe ions produced in the interaction region were detected by means of a conventional channeltron.

The first experiment on the two-photon double-resonant excitation of the Xe* 5*p*⁵*nf* autoionization states using the combination of a mode-locked laser [1]

and SR has already been successfully demonstrated by Meyer's group at LURE. The wavelength of SR was adjusted to be 10.4 eV, in order to prepare the $\text{Xe}^* 5p^5 5d$ intermediate states in a first step. The $\text{Xe}^* 5p^5 4f$ autoionization resonance can be excited within the wavelength region of FEL in a second step. Since the lifetime of the intermediate states is quite short (600 ps), the synchronization between the SR and laser pulses is essential in this experiment. The count rate for this measurement is about 200 counts/sec, which is about 1/1000 in comparison to the case when the non-monochromatized undulator radiation was used at BL3A1. Although the photon intensity of SR at BL7B is high enough to obtain total ion yield spectrum, it is found that considerable improvement on the experimental setup is required for measuring the angular distribution of photoelectrons from the same system on this beam-line.

We are planning to carry out similar experiments in the shorter wavelength region (around 400 nm) of FEL, where higher Rydberg series of the $\text{Xe}^* 5p^5 nf$ states via the $\text{Xe}^* 5p^5 5d$ intermediate state are accessible.

Reference

- 1) M. Gisselbrecht, A. Marquette and M. Meyer, *J. Phys. B* **31**, L977 (1998).

VIII-V-5 Angle-Resolved Photoion Spectra of SO_2

GEJO, Tatsuo; SHIGEMASA, Eiji; NAGASONO, Mitsuru; OJI, Hiroshi; HATSUI, Takaki; KOSUGI, Nobuhiro

The SO_2 molecule has three unoccupied valence orbitals, $3b_1^*$, $9a_1^*$ and $6b_2^*$, which can be associated with the three S $3p$ orbitals, where SO_2 has an electronic structure of $\text{S}^{4+}[(3s)^2(3p)^0] \cdot (\text{O}^{2-})_2$ in the limit of an ionic bonding picture and the $3b_1$, $9a_1$ and $6b_2$ orbitals correspond to out-of-plane $\text{S}3p \pi$ (π_{out}), in-plane $\text{S}3p \pi$ (π_{in}) and in-plane $\text{S}3p \sigma$, respectively.¹⁾ All the $\text{S}1s$ ($1a_1$) excitations to the $3b_1^*$, $9a_1^*$ and $6b_2^*$ orbitals are dipole-allowed and are found to be lying below the $\text{S}1s \rightarrow$ Rydberg excitations with the term values of 10.4, 5.7, and 4.8 eV, respectively.¹⁾ The chemical bond between S and O is not so strong, and even the excitation to the most antibonding σ^* ($6b_2$) orbital is located below the ionization threshold. The single excitations to all the unoccupied valence orbitals are observed below the ionization threshold even in the case of the O $1s$ absorption spectra assigned previously, though there are two O $1s$ orbitals, $1b_2$ and $2a_1$. The $1b_2$ - $2a_1$ splitting caused by the interaction between the two O $1s$ orbitals is expected to be negligible and does not change the situation.

The photoabsorption and angle resolved photoion spectra of SO_2 , were measured in the O K -edge region. The O $1s$ core-to-valence excited states of SO_2 were calculated by multi-reference configuration interaction including single and double excitations (MR-SDCI).

Figure 1a and 1b show the O K -edge photoabsorption and angle resolved photoion spectrum of SO_2 . The lowest photoabsorption feature A observed at 530.56 eV is well separated from the higher features. The feature A

is attributed to the O $1s\sigma(2a_1) \rightarrow \pi^*(3b_1)$ transition, considering its term value of 9.27 eV. It should be noted that the B_1 state is a dipole-allowed out-of-molecular plane (π^*) transition from the A_1 ground state, the A_1 and B_2 states are dipole-allowed in-plane transitions, and the A_2 state is dipole-forbidden; the $\pi^*(3b_1)$ orbital is not accessible from the O $1s\sigma(1b_2)$ electron. Between the lowest $1s \rightarrow \pi^*$ excitation at 530.56 eV and the O K -shell ionization threshold at 539.83 eV, the spectral feature is dominated by some broad bands labeled as B, C, and D at ~ 535 eV (term values of ~ 5 eV) arising from the $1s \rightarrow$ in-plane excitations, which consist of the O $1s \rightarrow 9a_1^*$ (dipole-allowed B_2 from $1b_2$ and A_1 from $2a_1$) and O $1s \rightarrow 6b_2^*$ (dipole-allowed A_1 from $1b_2$ and B_2 from $2a_1$) transitions. The structures E, F, and G are comparatively weak and have term values of 2.24, 1.63, and 0.75 eV, respectively; therefore, they are possibly assigned to the lowest s -type ($4s$ or $5s$) and p -type ($4p$ or $5p$) Rydberg transitions. In the continuum, two broad bands are observed around 540.80 and 542.69 eV, which are attributable to double excitations or S $3d$ -type shape resonances, because there are no other singly excited valence states than the $1s \rightarrow 3b_1^*$, $9a_1^*$ and $6b_2^*$ transitions.

References

- 1) J. Adachi *et al.*, *Chem. Phys. Lett.* **294**, 559 (1998).

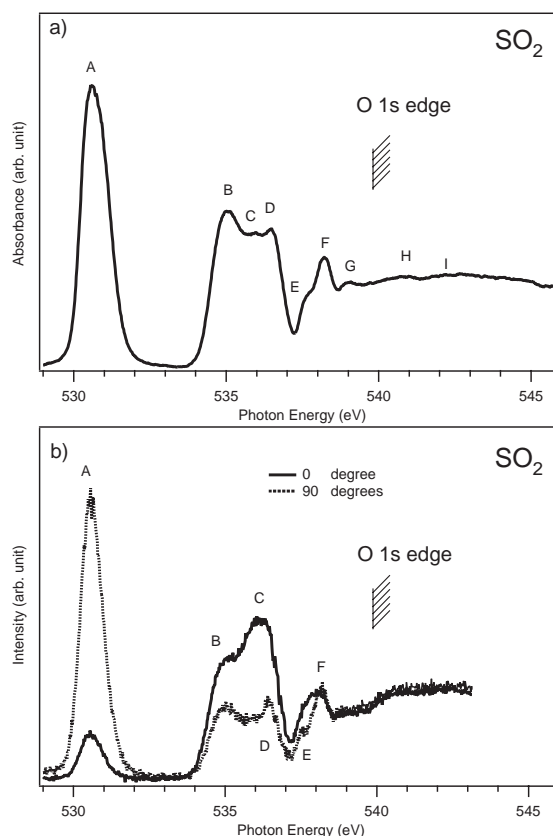


Figure 1. a) Absorption spectrum of SO_2 in the O K -edge region. b) Angle-resolved ion yield spectra of SO_2 . Dotted and solid lines denote I_{90} and I_0 ion yields, respectively.

VIII-V-6 The Measurement of Absorption Spectra of Trifluoromethyl Sulfur Pentafluoride in VUV Region

GEJO, Tatsuo; SHIGEMASA, Eiji; TAKAHASHI, Kenshi¹; MATSUMI, Yutaka¹
(¹Nagoya Univ.)

Global warming or green house effect is one of the major issues for environmental chemistry. Although CO₂, CH₄, and N₂O play a major role on the green house effect in air, some gases with much lower concentrations can contribute to the global warming because of their exceptionally large infrared absorption. For example, SF₆ has 22,200 times larger global warming potential (GWP) over a 100-year time than CO₂ although it is currently present in the atmosphere at only 4 ppt.¹⁾ Recently Sturges *et al.* detected Trifluoromethyl sulfur pentafluoride (SF₅CF₃), which is chemically close to SF₆, at Antarctic deep consolidated snow (firn).¹⁾ This Antarctic firn measurement shows that the concentration of SF₅CF₃ have increased from near zero in the late 1960s to about 0.12 ppt in 1999, whose trend matches to recent global warming tendency. They also measured a radiative forcing of SF₅CF₃, which is 0.57 watt per square meter per parts per billion.¹⁾ This is the largest radiative forcing, on a per molecule basis, of any gas found in the atmosphere up to this date. They also reported stratospheric profiles of SF₅CF₃ and suggested that it is long-lived in the atmosphere (on the order of 1000 years).¹⁾ If this is true, the irreversible accumulation of this gas may affect the green house effect drastically. In order to access this effect and lifetime of SF₅CF₃ in the stratosphere more precisely, its absorption spectra and cross sections in the VUV region are crucial.

The present photoabsorption measurement of SF₅CF₃ in the VUV region was performed at BL7B in the UVSOR facility. Synchrotron radiation at UVSOR was monochromatized by using a 3-m normal incidence monochromator. The intensity of the photon beam transmitted through a gas cell was monitored by using a silicon photodiode (IRD Inc, AXUV-100). The photoabsorption cross sections were calculated by using the Beer-Lambert expression. The data were checked to ensure there is no line saturation effect.

In the region of interest, two strong peaks in the absorption spectra of SF₅CF₃ were observed: One peak around 107 nm (A) and another one around 130 nm (B). The peak similar to A is also observed in SF₆, whereas the equivalent to the peak B was not observed. Therefore one can suggest that the peak B arises from the transition from the lone pair electron of CF₃.

Based on these data, we will estimate the lifetime of SF₅CF₃ in the stratosphere.

Reference

1) W. T. Sturges *et al.*, *Science* **289**, 613 (2000).

VIII-V-7 Symmetry-Resolved Cl 2p Photoabsorption Spectra of Cl₂

SHIGEMASA, Eiji; GEJO, Tatsuo; HATSUI, Takaki; KOSUGI, Nobuhiro

The 2p ionization spectra, or photoelectron spectra, show molecular field splittings (MFS) and spin-orbit splittings (SOS). The 2p excitation spectra, or photo-

absorption spectra, exhibit exchange splittings (EXS) in addition to MFS and SOS. We have already investigated very complicated spectral features due to EXS and SOS in the S 2p excitation region of SO₂, CS₂ and OCS, based on angle-resolved photoion spectroscopy (ARPIS) and the Breit-Pauli *ab initio* calculation. In the present work, Cl 2p ARPIS spectra of Cl₂ in comparison to HCl are reported. The lowest excited states in these molecules are the Cl 2p-π* excitation. There are three 2p orbitals, and the Cl 2p-σ* excitation involves parallel and perpendicular transitions with respect to the bond direction. We will discuss a propensity rule for the two transition directions by measuring the fragment-ion yields.

The experiments were performed on the newly constructed beamline BL4B at the UVSOR, IMS. ARPIS spectra were measured with two identical ion detectors having retarding grids, which were set at 0° and 90° relative to the electric vector of the light, by scanning the photon energy. The photon-energy resolution was set to about 50 meV for the present experiments. The Cl 2p ARPIS spectra of Cl₂ are displayed in Figure 1. The excitation energies and the nature of the structures observed will be discussed with the help of theoretical calculations.

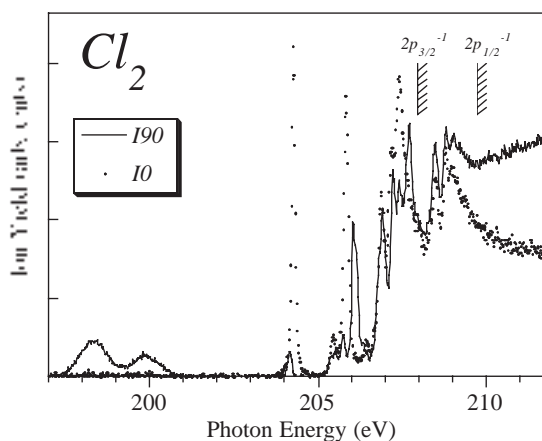


Figure 1. ARPIS spectra in the Cl 2p excitation region of Cl₂.

VIII-V-8 Dynamical Angular Correlation in Molecular Auger Decay

GUILLEMIN, Renaud¹; SHIGEMASA, Eiji; LE GUEN, Karine¹; CEOLINE, Denis¹; MIRON, Cataline¹; LECLERCQ, Nicola¹; MORIN, Paul¹; SIMON, Marc¹
(¹LURE)

[*Phys. Rev. Lett.* **87**, 203001 (2001)]

The first measurements of the angular distribution of Auger electrons from fixed-in-space molecules have been performed in the C K-shell ionization region of CO, for both parallel and perpendicular orientation of the molecular axis with respect to the light polarization vector. The ions emitted parallel or perpendicular to the electric vector of the incident radiation determine the possible Σ or Π symmetries in the ionization channels, respectively. The angular distributions obtained for the CO²⁺ B¹Σ Auger final state show dramatic spectral

variations, which also depend on the initial ionization channels, Σ or Π . The result strongly suggests the breakdown of the two-step model in which the Auger decay is treated independently of the initial photoionization process.

VIII-V-9 Nondipolar Electron Angular Distributions from Fixed-in-Space Molecules

GUILLEMIN, Renaud¹; HEMMERS, Oliver¹; LINDLE, Denis¹; SHIGEMASA, Eiji; LE GUEN, Karine²; CEOLINE, Denis²; MIRON, Cataline²; LECLERCQ, Nicola²; MORIN, Paul²; SIMON, Marc²; LANGHOFF, Peter³
(¹Univ. Nevada; ²LURE; ³Univ. California)

[*Phys. Rev. Lett.* **89**, 033002 (2002)]

The first indication of nondipole effects in the azimuthal dependence of photoelectron angular distributions emitted from fixed-in-space molecules is demonstrated in N_2 . Comparison of the results with angular distributions observed for randomly oriented molecules and theoretical derivations for the nondipole correction first order in photon momentum suggests that higher orders will be needed to describe distributions measured in the molecular frame.

VIII-V-10 Double and Triple Excitations Near the K-Shell Ionization Threshold of N_2 Revealed by Symmetry-Resolved Spectroscopy

SHIGEMASA, Eiji; GEJO, Tatsuo; NAGASONO, Mitsuru; HATSUI, Takaki; KOSUGI, Nobuhiro

[*Phys. Rev. A* **66**, 022508 (2002)]

High-resolution photoion yield spectra of N_2 are measured near the K-shell ionization threshold. Previously-unresolved multiple excitations are distinguished in the Σ - and Π -symmetry resolved spectra, which were obtained from the ion yield spectra recorded at 0° and 90° relative to the polarization direction. The three $^1\Pi_u$ and two $^1\Sigma_u^+$ doubly excited states are clearly identified. Furthermore, a weak Π -symmetry feature just at the σ^* -shape resonance position (~ 419 eV) is definitely resolved and assigned to the lowest $^1\Pi_u$ triple excitation with the help of quantum chemical calculations.

VIII-V-11 Optical and Magneto-Optical Studies on Electronic Structure of CeSb in the Magnetically Ordered States

KIMURA, Shin-ichi; OKUNO, Mitsuru¹; IWATA, Hideki¹; KITAZAWA, Hideaki²; KIDO, Giyu²; ISHIYAMA, Fumihiko³; SAKAI, Osamu⁴
(¹Kobe Univ.; ²Natl. Inst. Mater. Sci.; ³Tohoku Univ.; ⁴Tokyo Metropolitan Univ.)

[*J. Phys. Soc. Jpn.* **71**, (2002) in press]

The electronic structure of CeSb in the magnetically ordered states is examined by measuring the optical

reflectivity, the magnetic linear dichroism and the magnetic circular dichroism spectra at low temperatures under magnetic fields in the infrared region. The optical conductivity spectrum, as well as the reflectivity spectrum changes significantly with the complex magnetic phase diagram, and gives detailed information of electronic structures in the ordered states. The spectra in the ordered states cannot be explained only by the energy band folding due to the appearance of the periodic magnetic structure. By comparing with the calculated optical conductivity spectra, we found that not only the Ce4f-Sb5p mixing but also the Ce5d-Sb5p mixing mainly works in the ordered states.

VIII-V-12 Low Energy Electronic Structure of $Ce_{1-x}La_xSb$ ($x = 0, 0.1$) in the Magnetically Ordered States

KIMURA, Shin-ichi; OKUNO, Mitsuru¹; IWATA, Hideki¹; KITAZAWA, Hideaki²; KIDO, Giyu²
(¹Kobe Univ.; ²Natl. Res. Inst. Met.)

[*Physica B* **312-313**, 228 (2002)]

The anisotropy of the effect of pf mixing on the electronic structure of $Ce_{1-x}La_xSb$ ($x = 0, 0.1$) in the magnetically ordered states is examined by measuring the magnetic linear dichroism of the optical conductivity spectrum ($\sigma_{//}(\omega)$ for $E//B//[001]$, $\sigma_{\perp}(\omega)$ for $E\perp B//[001]$) in the infrared region at low temperatures under magnetic fields. The $\sigma_{\perp}(\omega)$ spectrum changes significantly with magnetic phase, whereas $\sigma_{//}(\omega)$ changes little. This result indicates that the electronic structure perpendicular to the magnetic field is more strongly modulated by pf mixing than that parallel to the field.

VIII-V-13 Temperature Dependence of Low-Energy Optical Conductivity of $Yb_4(As_{1-x}P_x)_3$ ($x = 0, 0.05, 0.15$)

KIMURA, Shin-ichi; OKUNO, Mitsuru¹; IWATA, Hideki¹; AOKI, Hidekazu²; OCHIAI, Akira³
(¹Kobe Univ.; ²Max-Planck-Inst., Germany; ³Tohoku Univ.)

[*J. Phys. Soc. Jpn.* **70**, 2829 (2001)]

To investigate the anomalous transport property and the electronic structure near the Fermi level of Yb_4As_3 , we measured the temperature dependence of the reflectivity spectra of $Yb_4(As_{1-x}P_x)_3$ ($x = 0, 0.05, 0.15$) in the photon energy range of 2 meV–1.5 eV. The optical conductivity spectrum due to carrier absorption (Drude curve) significantly changes with temperature. Above 200 K, the Drude curve with a high effective carrier density (N_{eff}) and a short relaxation time (τ) is commonly observed in all $Yb_4(As_{1-x}P_x)_3$. On the other hand, below 70 K, the Drude curve changes to one with a low N_{eff} and a long τ below 10 meV. At the same temperature, a new peak appears at 15 meV in Yb_4As_3 . The Drude curve and the new peak are considered to originate from the bare As 4p hole band and the hybridization state between the 4f and 5d bands on the

Yb³⁺ chain, respectively.

VIII-V-14 Charge Ordering Effect of Electronic Structure of Yb₄(As_{1-x}Sb_x)₃

KIMURA, Shin-ichi; NISHI, Tatsuhiko¹; OKUNO, Mitsuru¹; IWATA, Hideki¹; AOKI, Hidekazu²; OCHIAI, Akira³

(¹Kobe Univ.; ²Max-Planck-Inst., Germany; ³Tohoku Univ.)

[*J. Phys. Soc. Jpn.* **71**, 300 (2002)]

The change of the electronic structure near the Fermi level of Yb₄As₃ due to the charge ordering is examined by measuring the temperature dependence of reflectivity spectra of Yb₄(As_{1-x}Sb_x)₃ ($x = 0, 0.12, 0.24$) in the photon energy range of 2 meV–1.5 eV. In the optical conductivity spectra, a peak commonly appears at 0.4 eV below the temperature that is a little higher than the charge ordering temperature. Its intensity increases as the temperature decreases. The peak intensity indicates the ratio of the charge-ordered state for the whole because it originates from the optical transition to the Yb 5d band in the charge-ordered state.

VIII-V-15 Temperature-Induced Valence Transition of EuNi₂(Si_{0.25}Ge_{0.75})₂ Studied by Eu 4d-4f Resonant Photoemission and Optical Conductivity

KIMURA, Shin-ichi; OKUNO, Mitsuru¹; IWATA, Hideki¹; SAITOH, Tomohiko²; OKUDA, Taichi³; HARASAWA, Ayumi³; KINOSHITA, Toyohiko³; MITSUDA, Akihiro³; WADA, Hirofumi⁴; SHIGA, Masayuki⁴

(¹Kobe Univ.; ²Photon Factory; ³Univ. Tokyo; ⁴Kyoto Univ.)

[*J. Phys. Soc. Jpn.* **71**, 255 (2002)]

Eu 4d-4f resonant photoemission and optical reflectivity measurements of a temperature-induced valence transition material, EuNi₂(Si_{0.25}Ge_{0.75})₂, have been performed at several temperatures. The valence transition was observed and the mean valence was evaluated to be 2.37 ± 0.02 and 2.75 ± 0.25 below and above the valence transition temperature, respectively. The mixing between the Ni 3d conduction band and the Eu³⁺ 4f hole becomes weak as the temperature increases, showing the valence transition from Eu³⁺ to Eu²⁺.

VIII-V-16 Optical Gap in the Diluted Kondo Semiconductors Yb_{1-x}Lu_xB₁₂: Lattice and Single-Site Effects

OKAMURA, Hidekazu¹; MATSUNAMI, Masaharu¹; KIMURA, Shin-ichi; NANBA, Takao¹; IGA, Fumiroshi²; TAKABATAKE, Toshiro²

(¹Kobe Univ.; ²Hiroshima Univ.)

[*Physica B* **312-313**, 157 (2002)]

We have studied the evolution of energy gap in the

optical conductivity [$\sigma(\omega)$] of Yb_{1-x}Lu_xB₁₂ as functions of temperature (T) and non-magnetic Lu substitution (x). YbB₁₂ has a well-developed energy gap in $\sigma(\omega)$ below 20 K, with the onset of $\sigma(\omega)$ at ~ 20 meV and a shoulder at ~ 40 meV. With increasing T or x , the energy gap is rapidly filled in, which indicates the importance of coherence among the Yb 4f orbitals at different sites. The shoulder, on the other hand, remains nearly unshifted in wide ranges of T (to 70K @) and x (0–1/2), which shows that the characteristic energy for the gap is given by some single-site energy scale of Yb³⁺. Namely, both lattice and single-site effects play important roles in the gap formation of YbB₁₂.

VIII-V-17 Magneto-Optical Study of the Colossal Magnetoresistance Pyrochlore Tl₂Mn₂O₇

OKAMURA, Hidekazu¹; KORETSUNE, Toshihisa¹; MATSUNAMI, Masaharu¹; KIMURA, Shin-ichi; NANBA, Takao¹; IMAI, H.²; SHIMAKAWA, Y.²; KUBO, Y.²

(¹Kobe Univ.; ²NEC Corp.)

[*Physica B* **312-313**, 714 (2002)]

Pyrochlore Tl₂Mn₂O₇ has been found to exhibit a colossal magneto-resistance (CMR) that is comparable to that for the perovskite manganites such as La_{1-x}Sr_xMnO₃: In order to probe the microscopic electronic structures of Tl₂Mn₂O₇; we have measured its optical conductivity $\sigma(\omega)$ in wide ranges of photon energy, temperature (T), and external magnetic field (B). We have observed very strong variations of $\sigma(\omega)$ with T and B near the Curie temperature, where the CMR manifests itself. Analyses on the variations in $\sigma(\omega)$ show that both T - and B -induced evolutions of the electronic structures in Tl₂Mn₂O₇ are very similar to each other, and that they are universally related to the development of macroscopic magnetization. We have also observed a pronounced Kerr rotation at the plasma edge of the reflectivity.

VIII-V-18 Influence of Electronic Structure of CeSbNi_{0.15} on its Optical Conductivity

HONG, S. O.¹; MIN, B. H.¹; LEE, H. J.¹; KIMURA, Shin-ichi; JUNG, M. H.²; TAKABATAKE, Toshiro²; KWON, Y. S.¹

(¹SungKyunKwan Univ., Korea; ²Hiroshima Univ.)

[*Physica B* **312-313**, 251 (2002)]

The reflectivity of CeSbNi_{0.15} is measured at several temperatures in the low energy regions. The optical conductivity is obtained from the measured reflectivity. The carrier concentration and the relaxation time are evaluated by the Drude model. It is found that the pf mixing collapse takes place in CeSbNi_{0.15} and that the gap formation occurs at 7 K.

Computer Center

VIII-W Computer Simulation of Quantum Systems in Condensed Phase

VIII-W-1 Vibrational Energy Transfer from Solute to Solvent: An Analysis Based upon Path Integral Influence Functional Theory and Mixed Quantum-Classical Molecular Dynamics Method

MIKAMI, Taiji; OKAZAKI, Susumu

Path integral influence functional theory and mixed quantum-classical molecular dynamics method have been applied to the analysis of molecular mechanism of solute vibrational energy relaxation in solution. A numerical example is CN^- ion in water.

First, quantum effect of the solvent has been examined by taking a zero limit of Planck constant relevant to the solvent degrees of freedom. The effect is unexpectedly great. Classical approximation for the solvent significantly overestimates the relaxation time. The degree of the overestimation depends much upon the process, *e.g.* single-phonon, two-phonon, and three-phonon processes. However, it is interesting to find that it affects little energy dissipation path. Second, in order

to obtain a microscopic picture of the relaxation in terms of molecular motion, couplings between normal mode and the solute were divided into contributions from each water molecule. Couplings spread over the normal modes are not localized within particular modes. However, in molecular language, molecules in the first hydration shell are mostly responsible for the energy flow from the solute. Third, the couplings actually found in the solution have also been analyzed as a function of time. The solvent does not show delta-function-like coupling. This indicates that the system does not relax by collision which is usually found in the gas state. The coupling in the solution oscillates very rapidly. Then, matching of both transition frequency and phase between the interaction and the wave function of the system were found to be important. In a short time scale, we cannot find any systematic behavior of the coupling. It looks like random. However, integrating the coupling over pico second, the system shows relaxation to the ground state to a certain extent. The relaxation rate changes in hundred femto second or pico second reflecting the structural change of the hydration shell.

VIII-X Molecular Dynamics Study of Classical Complex Systems

VIII-X-1 A Molecular Dynamics Study of Water Penetration into Biomembrane

KAWAKAMI, Tomonori¹; AIZAWA, Keizo¹; HAYMET, Anthony D. J.²; OKAZAKI, Susumu (¹Tokyo Inst. Tech., ²Univ. Houston)

Free energy profile of water penetration into lipid bilayer has been evaluated based upon molecular dynamics calculations combined with thermodynamic integration method. The calculated profile for 25 arbitrarily chosen penetration paths shows that the free energy barrier height has a wide distribution, demonstrating a sort of selectivity of the path by water molecule. Structure of the path or structure of the surrounding lipid molecules was examined in order to extract a factor which determines the barrier height.

VIII-X-2 Molecular Dynamics Study of Mechanical Extension of Polyalanine by AFM Cantilever

IWAHASHI, Kensuke; MIKAMI, Taiji; MASUGATA, Kensuke¹; IKAI, Atsushi¹; OKAZAKI, Susumu

(¹Tokyo Inst. Tech.)

A series of molecular dynamics calculations have been performed mimicking the mechanical extension of α -helical polyalanine molecule in water on the AFM. Force profile has been evaluated as a function of extension. In an initial stage of the extension, $\sim 5\%$, the force was found to follow the Hooke's law up to about 140 pN. At the extension of about 10%, however, the restoring force diminishes, indicating the rupture of α -helix. Then, α -helix region and β -strand region separate from each other in one molecule. Further extension causes stepwise breakages of hydrogen bonds to give the wholly β -stranded polyalanine.

VIII-Y Theoretical Studies on Electronic Structure and Dynamics of Electronically Excited States

VIII-Y-1 Chemical Reactions in the O(¹D) + HCl System I. *Ab Initio* Global Potential Energy Surfaces for the 1¹A', 2¹A', and 1¹A'' States

NANBU, Shinkoh; KAMISAKA, Hideyuki¹; BIAN, Wensheng; AOYAGI, Mutsumi; TANAKA, Kiyoshi²; NAKAMURA, Hiroki
(¹GUAS; ²Hokkaido Univ.)

[*J. Theor. Comp. Chem.* in press]

New global *ab initio* potential energy surfaces (PES) are presented for the low-lying 1¹A', 2¹A', and 1¹A'' electronic states which are correlated to O(¹D) + HCl. These potential energy surfaces are computed by using the multi-reference configuration interaction method with the Davidson correction (MRCI + Q). The reference functions are constructed by the complete active space self-consistent field (CASSCF) calculations using the quadruple zeta + polarization basis set augmented with diffuse functions. The computations are carried out at about 5000 molecular conformations on each three-dimensional potential energy surface. The high accuracy of the computations is confirmed by a comparison with the available most accurate data for the ground state 1¹A'; thus the present work is the first report of the accurate potential energy surfaces for the two excited states. Three low-lying transition states on the excited surfaces, two (TS2 and TS4) on 1¹A'' and one (TS3) on 2¹A', are found. Since TS2 and TS3 are as low as 0.07 eV and 0.28 eV, respectively, and correlated to the OH(²Π) + Cl(²P) product, these excited surfaces are expected to play quite important roles in the reaction dynamics. Possible effects of non-adiabatic couplings among the three PESs are also briefly discussed, although the non-adiabatic couplings have not yet been estimated. The quantum reaction dynamics on these three PESs are discussed in the second and third accompanying paper.

In the present work, we have determined new global three *ab initio* potential energy surfaces accurately; and furthermore quantum wave packet dynamics calculations have been carried out to obtain the total reaction probabilities. The reaction probability for HCl(*v* = 0, *j* = 0) shows that the OH + Cl product channel *via* the 1¹A'' state should be opened at the lower collision energy than $E_{\text{coll}} = 0.529$ eV, while the channel *via* 2¹A' should be closed. Although there was the discrepancy between previous theoretical works and experimental results, it was explained by our works including the electronic excited states.

VIII-Y-2 Millimeter-Wave Spectroscopy of the Internal-Rotation Band of the He–HCN Complex and the Intermolecular Potential Energy Surface

HARADA, Kensuke¹; TANAKA, Keiichi¹; TANAKA, Takehiko¹; NANBU, Shinkoh; AOYAGI,

Mutsumi
(¹Kyusyu Univ.)

[*J. Chem. Phys.* in press]

Millimeter-wave absorption spectroscopy combined with a pulsed-jet expansion technique was applied to the measurement of the internal-rotation band of the He–HCN in the frequency region of 95–125 GHz. In total 13 rovibrational lines, split into nitrogen nuclear hyperfine structure, were observed for the fundamental internal-rotation band, *j* = 1–0. The observed transition frequencies were analyzed including their hyperfine splitting to yield an intermolecular potential energy surface, as improved from the one given by a coupled-cluster single double (triple) *ab initio* calculation. The surface obtained has a global minimum in the linear configuration (He··H–C–N) with a well depth of 30.2 cm⁻¹, and the saddle point located in the anti-linear configuration (H–C–N··He) is higher by 8.174 cm⁻¹ in energy than the global minimum. The distance R_m between the He atom and the center of mass of HCN along the minimum energy path shows a strong angular dependence; $R_m = 4.169$ Å and 4.040 Å in the linear and anti-linear forms, respectively, while it is 3.528 Å in a T-shaped configuration. In the first excited internal-rotation state (*j* = 1), levels with *l* less than 4 are bound but not for the one with *l* = 5, according to the energy level diagram calculated from the present potential energy surface, where *l* denotes the quantum number for the end-over-end rotation of the complex. The energy level diagram is consistent with the millimeter-wave observation, in which the $\Delta l = 0$ transitions with *l* = 0 ~ 4 were observed but not for those with *l* equal to or greater than 5. The band origin of the internal-rotation band, 98.70 GHz, as defined to be the same as the frequency of the *R*(0) transition, is larger by 11% than the *J* = 1–0 rotational transition frequency of the free HCN molecule.

VIII-Y-3 Determination of the Global Potential Energy Surfaces and Transition Wave Packet Dynamics for Polyatomic Systems

NANBU, Shinkoh; ISHIDA, Toshimasa¹; GRAY, Stephen K.²; GONZALEZ, Miguel³
(¹Shizuoka Univ.; ²Argonne Natl. Lab.; ³Univ. Barcelona)

Computational algorithm for the determination of the global potential energy surfaces of polyatomic systems are developed with using the interpolant moving least squares scheme, which was proposed by Ishida and Schatz [*Chem. Phys. Lett.* **314**, 369 (1999)]. In this scheme, any derivatives in quantum-chemical calculations are not required to construct the surface and in contrast with previously developed schemes based on Shepard interpolation alone. In our new algorithm, the molecular conformations are generated with the Monte

Carlo sampling, and then the *ab initio* calculations for all of the conformations are performed by parallel computing. Therefore, we have good advantage for computational time for the serial calculations. Application is made to the tetra-atomic systems, the $2\text{OH} \leftrightarrow \text{H}_2\text{O} + \text{O}$ reaction.

Regarding to the wave packet dynamics, we are also developing the program code based on the MPI-library to make a time-evolution of the wave packet for the tetra-atomic systems.

VIII-Y-4 *Ab Initio* Study of Conformers of *p*-tert-Butylcalix [4] Crown-6-Ether Complexed with Alkyl Ammonium Cations

CHOE, Jong-In¹; CHANG, Suk-Kyu¹; NANBU, Shinkoh
(¹Chung-Ang Univ.)

[*Bull. Korean Chem. Soc.* **23**, 891 (2001)]

The structures and energies of *p*-tert-butylcalix[4]-crown-6-ether (1) in various conformers and their alkyl ammonium complexes have been calculated by *ab initio* HF/6-31G quantum mechanics method. We have tried to obtain the relative affinity of partial-cone and 1,3-alternate conformers of 1 for alkyl ammonium guests by comparison with its cone-shaped analogue. We have also calculated the relative complexation efficiency of these host-guest complexes focusing on the binding sites of crown-6-ether moiety or benzene-rings pocket of the host molecule 1. These calculations revealed that the crown moiety has better complexation efficiency than upper rim part of calix[4]arene that is in similar trend to the cone-shaped complexes.

VIII-Y-5 *Ab Initio* Study of the Complexation Behavior of Calix[5]arene Derivative toward Alkyl Ammonium Cations

CHOE, Jong-In¹; CHANG, Suk-Kyu¹; MINAMINO, Satoshi; NANBU, Shinkoh
(¹Chung-Ang Univ.)

[*Bull. Korean Chem. Soc.* submitted]

The structures and complexation energies of penta-O-alkylated 1b and penta-O-tert-butyl ester 1e of *p*-tert-butylcalix[5]arene and its simplified structures (2b and 2e) toward a series of alkyl ammonium guests have been calculated by semi-empirical AM1 quantum mechanics method. For AM1 calculation, complexation efficiencies of the simplified host 2e are very similar to the values of host 1e. The complexes of simplified host 2e with alkyl ammonium ions have been also optimized by *ab initio* HF/6-31G quantum mechanics method. The calculated complexation efficiencies for 2e by *ab initio* method have been found to be bigger in magnitude than the values obtained by AM1 calculations for linear alkyl ammonium guests. Calculation results show that all of the calix [5] aryl derivatives investigated in this study have much better complexation ability toward ammonium cation without alkyl group over other alkyl ammonium guests. *Ab initio* calculations also well

duplicate the molecular discriminating behaviors of calyx [5] arene derivative 2e between butyl ammonium ions: *n*-BuNH₃⁺ > *iso*-BuNH₃⁺ > *sec*-BuNH₃⁺ > *tert*-BuNH₃⁺.

VIII-Y-6 Formation of HCl⁺(A²Σ⁺) and HBr⁺(A²Σ⁺) Resulting from He(2³S) Penning Ionization of HCl and HBr

TOKUE, Ikuo¹; TANAKA, Hiroyuki¹; YAMASAKI, Katsuyoshi¹; NANBU, Shinkoh
(¹Niigata Univ.)

[*J. Phys. Chem. A* **106**, 6068 (2002)]

He(2³S) Penning ionization of HCl and HBr leading to HCl⁺(A) and HBr⁺(A) has been studied optically by using a crossed-beam apparatus. The ratios of the vibrational population, P_v/P₁(v' = 2 and 3) of HCl⁺(A) and P₁/P₀ of HBr⁺(A), increase with the collision energy in the region of 120–200 meV. The rotational distributions of HCl⁺(A, v' = 0) and HBr⁺(A, v' = 0) can be represented by a double-Boltzmann distribution; the temperatures are 200 ± 50 and 700 ± 80 K for HCl⁺(A, v' = 0) and 250 ± 50 and 1200 ± 200 K for HBr⁺(A), and are nearly independent of the collision energy. The model potential surface for He*(Li) + HCl as the entrance channel is nearly isotropic and shows a shallow dip of about 20 meV, while the surface for He + HCl⁺(A) as the exit channel is anisotropic and shows a deep minimum of 250 meV in the He–H–Cl collinear direction. These results suggest that at least two processes contribute to formation of these ions; one is the direct Penning ionization and the other is the formation via a temporary complex [HeHCl(A)]⁺ by orbiting.

VIII-Y-7 Theoretical Study of Vibrational States for AINC/AICN

MINAMINO, Satoshi; NANBU, Shinkoh; AOYAGI, Mutsumi

The character of the low-lying electronic states of AINC strongly depends on the bond distance of Al-NC, because the covalent states are lying closely to the ionic states. Especially, due to the electronic ground state having the ionic character, the bending vibrational motion has a quite strong anharmonicity, and the motion is characterized as a large amplitude motion (LAM). Therefore, in general, the observed spectrum has the complicated vibronic structures and it is difficult to understand the molecular conformation having the LAM. In this study, we determined the global potential energy surfaces of the electronic ground state for the isomerization of AINC/AICN, and we elucidated the molecular structure of the complicated vibronic states by solving the exact Schrödinger equation for the nuclear motion.

VIII-Y-8 Boundary Expansion in Time-Dependent Nonadiabatic Problems

TAKAMI, Toshiya

Time-dependent nonadiabatic transitions were studied as an initial value problem in a finite parameter range. We introduced “boundary expansion” by expanding Schrödinger’s equation around end points of the parameter. We have shown that extra transitions emerge at the points, and are explained by the terms of the expansion. We have also shown that Berry’s superadiabatic base is naturally defined through the expansion. By the use of the superadiabatic base, we performed numerical analysis of multi-level non-adiabatic transitions in systems with a random matrix Hamiltonian.

VIII-Y-9 Optimal Control of Random Matrix Systems with a Parameter

TAKAMI, Toshiya; FUJISAKI, Hiroshi

We studied control of chaotic quantum systems by applying Optimal Control Theory (OCT) to random matrix Hamiltonian systems with a parameter. For simple two-state problems, we have shown that the optimized field obtained by OCT can be classified into several types: (i) oscillating one with a frequency which agrees with the energy split between the initial and the final state; (ii) one which mainly uses transition between diabatic states at an avoided crossing; (iii) one which can be seen as nonadiabatic transition, etc. Although the oscillating solution is always obtained even in many level systems if the final time is large enough, it is difficult to distinguish other types of solution in short time.

We have shown that the distribution of the optimized solutions for short time is affected by dynamical properties of the system. In particular, we examined influence of the strength of chaos or complexity of the system. We have also studied systems with banded random elements.